

Comprehensive analysis of the Apertif Fast Radio Burst sample: similarities with young, energetic neutron stars

Inés Pastor-Marazuela^{1,2,3,4}, Joeri van Leeuwen¹, Anna Bilous¹, Liam Connor^{5,2}, Yogesh Maan^{6,1}, Leon Oostrum^{1,2,7}, Emily Petroff^{2,8}, Dany Vohl^{2,1}, Kelley M. Hess^{9,1}, Emanuela Orrù¹, Alessio Sclocco⁷, and Yuyang Wang²

¹ ASTRON, the Netherlands Institute for Radio Astronomy, Oude Hoogeveensedijk 4,7991 PD Dwingeloo, The Netherlands

² Anton Pannekoek Institute, University of Amsterdam, Postbus 94249, 1090 GE Amsterdam, The Netherlands

³ Jodrell Bank Centre for Astrophysics, Department of Physics and Astronomy, The University of Manchester, Manchester, M13 9PL, UK e-mail: ines.pastor.marazuela@gmail.com

⁴ Rubicon Fellow

⁵ Cahill Center for Astronomy, California Institute of Technology, Pasadena, CA, USA

⁶ National Centre for Radio Astrophysics, Tata Institute of Fundamental Research, Pune 411007, Maharashtra, India

⁷ Netherlands eScience Center, Science Park 402, 1098 XH, Amsterdam, The Netherlands

⁸ Perimeter Institute for Theoretical Physics, Waterloo ON N2L 2Y5, Canada

⁹ Department of Space, Earth and Environment, Chalmers University of Technology, Onsala Space Observatory, 439 92, Onsala, Sweden

ABSTRACT

Understanding the origin of the energetic fast radio bursts (FRBs) has become the main science driver of recent dedicated FRB surveys powered by real-time instrumentation. Between July 2019 and February 2022, we carried out ALERT, an FRB survey at 1370 MHz using the Apertif Radio Transient System (ARTS) installed at the Westerbork Synthesis Radio Telescope (WSRT). Here we report the detection of 18 new FRBs, and we study the properties of the entire 24 burst sample that were detected during the survey. For five bursts, we identify host galaxy candidates within their error regions with $>50\%$ probability association. We observe an average linear polarisation fraction of $\sim 43\%$ and an average circular polarisation fraction consistent with 0% . A third of the FRBs display multiple components. These burst structures and the polarisation fractions are strikingly similar to those observed in young, energetic pulsars and magnetars. The Apertif FRBs next reveal a population of highly scattered bursts. Given the observing frequency and time resolution, the scattering of most FRBs is likely to have been produced in the immediate circumburst environment. Furthermore, two FRBs show evidence for high rotation measure values, reaching $|RM| > 10^3$ rad m^{-2} in the source reference frames. This corroborates that some source environments are dominated by magneto-ionic effects. Together, the scattering and rotation measures ALERT finds prove that a large fraction of FRBs are embedded in complex media such as star forming regions or supernova remnants. Through the discovery of FRB 20200719A, the third most dispersed FRB so far, we further show that one-off FRBs emit at frequencies in excess of 6 GHz, the highest known to date. We compare this to the radio-bright, high-frequency emission seen in magnetars. Finally, we determine an FRB all-sky rate of 459^{+208}_{-155} sky $^{-1}$ day $^{-1}$ above a fluence limit of 4.1 Jy ms, and a fluence cumulative distribution with a power law index $\gamma = -1.23 \pm 0.06 \pm 0.2$, which is roughly consistent with the Euclidean Universe predictions. Through the high resolution in time, frequency, polarisation and localisation that ALERT featured, we were able to determine the morphological complexity, polarisation, local scattering and magnetic environment, and high-frequency luminosity of FRBs. We find all these strongly resemble those seen in young, energetic, highly magnetised neutron stars.

Key words. fast radio bursts – high energy astrophysics – neutron stars

1. Introduction

The field of Fast Radio Bursts (FRBs) – extragalactic radio flashes of millisecond duration with extreme luminosities (Lorimer et al. 2007; Petroff et al. 2019; Cordes & Chatterjee 2019) – has been rapidly evolving in recent years. The number of published FRBs is now in the hundreds (Petroff et al. 2022), more than forty have been localised to their host galaxies¹, and about fifty are known to repeat (CHIME/FRB Collaboration et al. 2023a). Although these discoveries have not yet fully unveiled the origin of FRBs, the detection of a bright radio burst from the Galactic magnetar SGR 1935+2154 demonstrated that at least some FRBs may be produced by magnetars (Bochenek et al. 2020; CHIME/FRB Collaboration et al. 2020). These findings have been possible thanks to the increased number of

observations and surveys dedicated to FRB searching in recent years.

The current published sample of both repeating and seemingly one-off FRBs is dominated by sources discovered in the CHIME/FRB project, which searches in the 400 – 800 MHz band (CHIME/FRB Collaboration et al. 2021). Given the large sample size, population studies have been possible with the CHIME/FRB data to look at properties such as the bulk burst morphology of a large FRB sample. In studies of this sample, Pleunis et al. (2021a) find four burst archetypes: single component FRBs, classified as either narrow or broadband; multi-component bursts with each component spanning a similar frequency extent; or multi-component bursts with ‘sadtrombone-like’ downward drifting structure. A population study of burst properties in the first CHIME/FRB Catalog by Chawla et al. (2022) also reports the overabundance of scattering de-

¹ FRB Hosts Catalog: <https://www.frb-hosts.org/>

ected in this sample. Additionally, injections performed for the catalog analysis confirm CHIME/FRB detections are biased against highly scattered events, hinting at the presence of a wider FRB population with large scattering timescales to which CHIME/FRB is less sensitive (CHIME/FRB Collaboration et al. 2021).

Several observed properties of FRBs, including dispersion measure (DM), scattering, scintillation, and polarisation, are highly frequency dependent. While the CHIME/FRB sample is by far the largest, studies at higher (and lower) radio frequencies are essential to probe the full extent of the FRB population across all parameters, including DM and scattering. One-off FRBs discovered at frequencies of ~ 1 GHz by the Murriyang Telescope at the Parkes Observatory and the Australian Square Kilometre Array Pathfinder (ASKAP) also show evidence of scatter broadening and multiple components (Day et al. 2020; Champion et al. 2016), some of which might be beyond the width detection threshold at CHIME/FRB frequencies.

The best-studied FRBs by far have been the small but productive sample of repeating FRB sources. Both the low (110 MHz; Pastor-Marazuela et al. 2021; Pleunis et al. 2021b) and high (8 GHz; Gajjar et al. 2018) frequency detections of FRBs have been made through targeted observations of known prolific repeaters. Comparing activity of the repeating FRB 20180916B at 150 MHz and 1.4 GHz simultaneously has shown frequency-dependent activity of this particular source (Pastor-Marazuela et al. 2021). For one-off FRBs, direct comparisons of behaviour at high and low frequencies is not yet possible. As such, assembling large samples of one-off FRBs at different radio frequencies may prove the most fruitful in uncovering frequency-dependent properties. Comparing the observed distributions of DM, scattering, flux, fluence, and scintillation of FRB samples from different instruments will provide insight into the underlying FRB population distribution – either directly, or after correcting for the survey selection effects, as in e.g. Gardenier & van Leeuwen (2021) – as well as the properties of the burst environment and host galaxy.

In this paper we present the sample of 24 one-off FRBs discovered with the Apertif system on the Westerbork Synthesis Radio Telescope (WSRT), during the Apertif-LOFAR Exploration of the Radio Transient sky survey (ALERT; van Leeuwen et al. 2023). Its high spectro-temporal resolution search has yielded a self-contained sample of FRBs for which we report DM, burst morphology, frequency structure, scattering, scintillation, and polarisation. In Section 2 we present the observing strategy for Apertif, while Section 3 presents the data release. In Section 4 we present the data analysis method of the detected bursts. In Section 5 we present the detected FRB sample, the burst properties and the results of population analysis across DM, propagation effects, morphology, and polarisation; we discuss further in Section 6 and conclude in Section 7.

2. Observations

Apertif, the APERTure Tile in Focus, is a front-end instrument installed at the Westerbork Synthesis Radio Telescope (WSRT), in twelve of fourteen 25 m dishes of the interferometer (van Cappellen et al. 2022), located in the Netherlands. Apertif consists of phased array feeds (PAFs), with each dish forming 40 compound beams (CBs) on the sky and thus increasing the original Field of View (FoV) of the WSRT to 8.2 deg^2 (Adams & van Leeuwen 2019). Apertif has carried out an imaging and a time domain survey between July 2019 and February 2022. The Apertif Radio Transient System (ARTS) was designed to carry out the time do-

main survey, as described in van Leeuwen et al. (2023), with supporting detail in van Leeuwen et al. (2022). The CBs from each dish are coherently beamformed into 12 tied-array beams (TABs, see Maan & van Leeuwen 2017), and these are next recombined in frequency to form 71 synthesised beams (SBs) per compound beam (van Leeuwen et al. 2023). The SBs of all CBs generate a total of 2840 Stokes I, Q, U, and V data-streams at a central frequency of 1370 MHz and a bandwidth of 300 MHz, with a time and frequency resolution of $81.92 \mu\text{s}$ and 195 kHz respectively. The Stokes I data-streams are then searched for single-pulses with the software AMBER² (Sclocco et al. 2014, 2016, 2019). The data post-processing is implemented with the Data Analysis of Real-time Candidates from the Apertif Radio Transient System (DARC ARTS³, Oostrum 2020), and includes real-time candidate classification through a neural network that is public (Connor & van Leeuwen 2018, 2024). The single pulse searches and data post-processing are run on a 40-node graphics processing unit (GPU) cluster at the WSRT. The observations were scheduled with apersched (Hess et al. 2022).

ARTS has proven its FRB searching capabilities at high time and frequency resolution through the follow-up and detection of known repeating FRBs (Oostrum et al. 2020; Pastor-Marazuela et al. 2021), as well as through the discovery of new one-off FRBs (Connor et al. 2020; Pastor-Marazuela et al. 2023; van Leeuwen et al. 2023). Here, we present the discovery of a new population of, as of yet, one-off FRBs that have been detected in the ARTS time domain survey.

2.1. Pointings and sky exposure

The priority source list and thus pointing definition evolved during the ALERT survey, in order to adapt to the rapidly evolving FRB discoveries (Bailes 2022). While only two repeating sources were known at the beginning of the survey in July 2019 (Spitler et al. 2016; CHIME/FRB Collaboration 2019), several new repeaters were reported soon after (CHIME/FRB Collaboration et al. 2019; Fonseca et al. 2020). Simultaneously, the number of Apertif detections was increasing. From 2020 onward, the observing shifted away from fields with no known FRBs in order to prioritise the follow up of repeaters and Apertif-discovered FRBs. Given the isotropic sky distribution of FRBs (Bhandari et al. 2018), one-off FRBs should be detected blindly at the same rate in pointings with and without known FRBs.

Figure 1 shows the exposure time per sky region in equatorial coordinates and the location of the newly discovered FRBs, while Fig. 2 shows the fraction of time spent on survey pointings, repeating FRBs, one-off FRBs, new FRBs discovered with Apertif, pulsars and calibration observations. During the 2019 observations, $\sim 70\%$ of the time was spent on the Apertif survey pointings, while the remaining $\sim 30\%$ was divided between follow up of known and newly discovered one-off FRBs and calibration observations. The evolution in pointing strategy in 2020 and 2021 to prioritise the follow up of known repeaters and newly discovered Apertif FRBs is reflected in Fig. 2, where the changes implemented around Jan 1 of each calendar year are visible. Roughly 60% of the time was dedicated to repeater follow up, 20% to the follow up of Apertif FRBs and the remaining 20% in survey pointings and calibration observations.

² AMBER: <https://github.com/TRASAL/AMBER>

³ DARC: <https://github.com/TRASAL/darc>

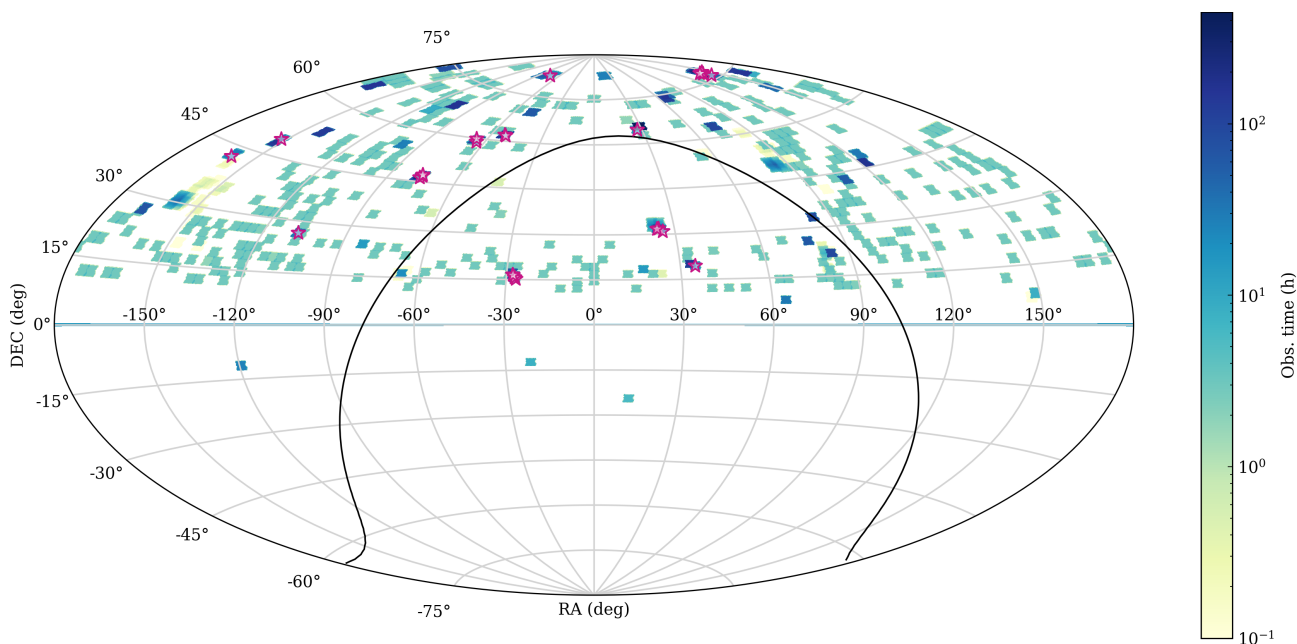


Fig. 1. Exposure time per sky area in equatorial coordinates. Dark blue regions correspond to larger exposure times, and white regions have not been observed. The position of the detected FRBs is marked by magenta stars. The Galactic plane is indicated by the black line.

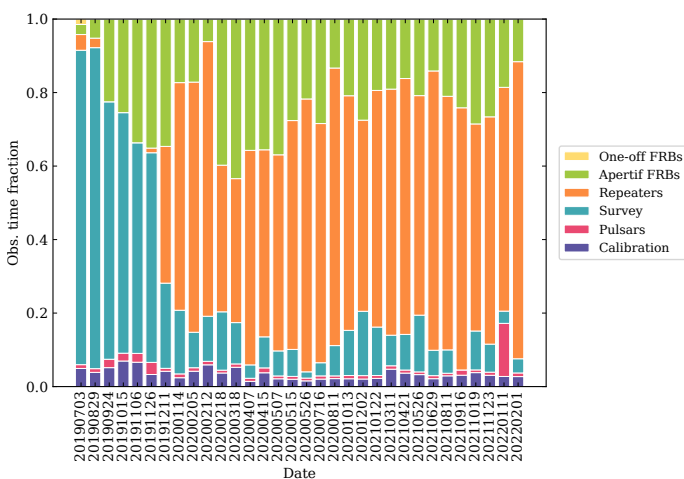


Fig. 2. Fraction of time spent on different target field classes per observing run. Each vertical bar corresponds to a different observing run, with the start date indicated below in YYYYMMDD format. Purple corresponds to the fraction of the time for calibration observations, pink for pulsar observations, blue for fields with no known FRBs defined in the original ALERT survey, orange for known repeating FRBs, green for previously detected Apertif FRBs, and yellow for one-off FRBs discovered by other instruments.

3. Data release

The observations described above were archived in the down-sampled, Stokes-I, PSRFITS format described in van Leeuwen et al. (2023), which are now public. The 2019 data was released before, as Apertif Time-Domain Data Release 1, together with van Leeuwen et al. (2023). Accompanying the current paper we make public also the 2020–2022 data. Together, the 2019–2022 data comprise Apertif Time-Domain Data Release 2, containing 1666 multi-hr pointings that form the whole Apertif Time-Domain legacy data set, since Apertif observations ended in 2022. This complete set is accessible at ASTRON, through the

Data Explorer⁴ or the Virtual Observatory (VO) Interface⁵. The release includes the subset of pointings with FRB detections⁶, that can be directly downloaded; and the set of all pointings⁷, which require staging from tape by the ASTRON helpdesk.

4. Data analysis

In this section, we detail the post-processing data analysis performed on the bursts that resulted from the AMBER and DARC searches and candidate selection (as described in van Leeuwen et al. 2023). Here we describe the methods to determine the burst properties, including dispersion measure, scattering, scintillation, flux calibration, morphology, frequency structure, polarisation, and localisation. The results of these analyses are presented in Section 5. Although for some discoveries the analysis and the results are intertwined to some extent, separating the analysis into its own Section makes it easier to reference later when discussing the results.

4.1. Dispersion measure and redshift estimation

Each FRB candidate detected by the AMBER pipeline has an associated DM that maximises the signal-to-noise ratio (S/N) at the given downsampling factor. Some of the detected FRBs present multiple components, and we thus used an algorithm based on Hessels et al. (2019)⁸, that was already put to test in Pastor-Marazuela et al. (2021) and Bilous et al. (2024), to find the DM maximising the structure of the burst. For faint and/or scattered bursts with no signs of multi-component structure, we used

⁴ <https://science.astron.nl/sdc/astron-data-explorer/data-releases/>

⁵ <https://vo.astron.nl/>; “Apertif Time Domain FRB search”

⁶ <https://hdl.handle.net/21.12136/383f3c18-9c2c-495e-9d4c-d3b4192a5b7d>

⁷ <https://hdl.handle.net/21.12136/03a6775b-e768-4212-bd06-027267d21c0a>

⁸ DM_phase: https://github.com/danielemichilli/DM_phase

pdmp⁹ instead, since it maximises S/N and in these cases this method is more robust at determining the correct DM. The measured DMs of all FRBs presented in this paper are given in Table A.1 of Appendix C.

In order to determine the redshift upper limit for each FRB, we first estimate the extragalactic DM (DM_{EG}) from the observed DM_{obs} . We predict the Milky Way (MW) contribution to the DM (DM_{MW}) from the NE2001 (Cordes & Lazio 2003) and YMW16 (Yao et al. 2017) Galactic electron density models, and take the average of the two. Since the Galactic halo can also significantly contribute to the DM, we adopt the model from Yamasaki & Totani (2020) to compute the MW halo DM (DM_{halo}) in the direction of each FRB. The extragalactic DM will thus be $DM_{EG} = DM_{obs} - DM_{MW} - DM_{halo}$. Next we apply the $DM-z$ relation from Macquart et al. (2020) assuming the cosmological parameters from Planck Collaboration et al. (2020) to obtain the mean redshift and 95% errors. For this, we use the python package FRB¹⁰. We assume a host galaxy contribution to the DM of 100 pc cm^{-3} . The measured DMs and estimated redshifts of our FRB sample are detailed in Section 5.4.1.

4.2. Flux calibration

To perform the flux calibration of all FRBs, we scheduled drift scan observations of the bright calibrator sources 3C147, 3C286, and/or 3C48 at the beginning and the end of each observing run. As the flux densities of these sources are known (Perley & Butler 2017), they can be used as calibrators to obtain the system-equivalent flux density (SEFD). For each FRB, we used the drift scan taken during the same observing run that was the least affected by radio frequency interference (RFI). To convert the pulse profile into flux units, we applied the radiometer equation using the obtained SEFD. We define the peak flux as the maximum flux value at the instrument time resolution (0.08192 ms), and it is thus a lower limit. Finally we integrated over a time window covering the whole burst duration to obtain the FRB fluences in units of Jy ms. Based on the measured stability of the system, we assume 20% errors on the fluence. The resulting fluxes and fluences are given in Table A.1 and detailed in Section 5.3.

4.3. Localisation and host candidate identification

To determine the localisation of the detected FRBs, we implement the localisation method described in Oostrum (2020) and van Leeuwen et al. (2023). The method consists of creating a model of the telescope response in sky coordinates and comparing it to the observed response pattern as follows: first, a model of the Compound Beams (CBs) is created based on drift-scan data. From this we construct the TABs and SBs, consequently obtaining a model of the SB sensitivity in Right Ascension (RA) and Declination (Dec). To localise a burst, we next compare its S/N per SB detection pattern against the predicted SB model. We define the best position of each burst as the resulting 99% confidence regions, which have narrow elliptical shapes since the WSRT is an East-West array. The size of the confidence region shrinks with both higher detection S/N and with a larger number of CBs in which the burst was detected. The orientation of the ellipse depends on the hour angle of the detection, due to the Earth rotation.

⁹ pdmp: <http://psrchive.sourceforge.net/manuals/pdmp/>

¹⁰ FRB: <https://github.com/FRBs/FRB/tree/main>

The localisation regions of all detected FRBs were covered by the Pan-STARRS1¹¹ survey (Chambers et al. 2019), thus giving us access to deep images and a source catalogue with a median photometric depth of 23.2 in the g -band. The project Pan-STARRS1 Source Types and Redshifts with Machine Learning¹² (PS1-STRM, Beck et al. 2021) provides source classifications and photometric redshifts for all the sources contained in the PanSTARRS1 3π DR1, computed through a neural network. Hence, for each FRB, we searched for all the PS1-STRM sources classified as “galaxies”, “quasi-stellar objects” (QSOs), or “unsure” contained within or near the localisation region, and within the expected redshift limits. When the number of known galaxies within an FRB error region was ≤ 5 , we performed a Probabilistic Association of Transients to their Hosts (PATH) analysis (Aggarwal et al. 2021), to determine the probability of the FRB being associated to each host galaxy candidate.

In most cases, the total FRB error region is of order 5 arcmin^2 , which is too large to unambiguously identify a unique FRB host galaxy candidate (see, e.g., Eftekhari & Berger 2017). Additionally, although some FRB error regions might contain more than one known host galaxy candidate, there are probably more that are too faint to be detected. FRBs have been localised to galaxies of different types spanning a broad range of masses (Bhandari et al. 2022; Gordon et al. 2023), from the dwarf galaxy hosts of FRB 20121102A (Chatterjee et al. 2017) and FRB 20190520B (Niu et al. 2022), to massive galaxies reaching close to $10^{11} M_{\odot}$ in the case of FRB 20200120E, which has been localised to a globular cluster of M81 (Bhardwaj et al. 2021; Kirsten et al. 2022). Following Petroff et al. (2018) and van Leeuwen et al. (2023), we estimate the expected number of galaxies within the comoving volume determined by the error region and the redshift upper limit of each burst. We adopt a dwarf galaxy number density of $n = (0.02 - 0.06) \text{ Mpc}^{-3}$ for galaxy masses $4 \times 10^7 M_{\odot} < M_{\text{stellar}} < 10^{10} M_{\odot}$ (Baldry et al. 2012; Haynes et al. 2011), and a massive galaxy number density of $n = (1.5 - 2.0) \times 10^{-3} \text{ Mpc}^{-3}$ for galaxy masses $M_{\text{stellar}} > 10^{11} M_{\odot}$ (Faber et al. 2007). The expected number of galaxies within the comoving volume V_{co} is simply $N_{\text{gal}} = nV_{\text{co}}$. The results of this analysis are given in Section 5.2.

4.4. Burst morphologies

We characterise the morphology of all FRBs by fitting their dedispersed pulse profiles to a single or multi-component model through minimisation of residuals. A human expert determines the number of components, guided in edge cases by the Bayesian information criterion (BIC) values for the fits. Each burst is fitted to a single or multi-component Gaussian model given by Eq. 1, with and without a convolution with an exponential decay given by Eq. 2 to represent scattering, thus assuming the scattering timescale to be the same for all components. After fitting the scattered and unscattered models, the model with the lowest BIC is selected, with BIC_g for the Gaussian, unscattered model, and BIC_{sc} for the scattered model. The resulting expression for the fitted pulse profile $I(t)$ is given by Eq. 3.

$$G_i(t) = A_i \exp\left(-\frac{(t - t_i)^2}{2\sigma_i^2}\right) \quad (1)$$

¹¹ Pan-STARRS1: <https://outerspace.stsci.edu/display/PANSTARRS>

¹² PS1-STRM: <https://archive.stsci.edu/hlsp/ps1-strm>

$$F(t) = \begin{cases} e^{-t/\tau_{sc}}, & \text{if } t \geq 0 \\ 0, & \text{otherwise} \end{cases} \quad (2)$$

$$I(t) = \begin{cases} \sum_{i=0}^n G_i(t), & \text{if } \text{BIC}_{sc} > \text{BIC}_g \\ F(t') \otimes \sum_{i=0}^n G_i(t'), & \text{otherwise} \end{cases} \quad (3)$$

Scattering is not the only explanation for the exponential broadening of the burst; intra-channel dispersive smearing is an instrumental effect that can also produce such broadening. While scattering is roughly proportional to ν^{-4} , intra-channel smearing is proportional to ν^{-3} , and it becomes significant when the burst width is not resolved at the time-frequency resolution of the instrument. For each burst, we compute the expected intra-channel smearing Δt_{DM} with the following equation (Petroff et al. 2019, Section 4.1.2):

$$\Delta t_{DM} = 8.3 \times 10^6 \text{ DM } \Delta \nu_{ch} \nu^{-3} \text{ ms}, \quad (4)$$

where $\Delta \nu_{ch}$ is the frequency resolution, and ν is the observing frequency, both in MHz. For Apertif, we have $\Delta \nu_{ch} = 0.195$ MHz and $\nu = 1370$ MHz. For FRBs where $\text{BIC}_{sc} < \text{BIC}_g$, we compare the resulting scattering timescale to the expected intra-channel smearing. If we find that $\tau_{sc} < \Delta t_{DM}$, we will consider that the burst scattering is not resolved.

For bursts where we determine the exponential broadening to be produced by scattering, we compute the frequency-dependent exponential broadening of the form $\tau_{sc} \propto \nu^{-\alpha}$, in order to get the dependence on frequency and determine the scattering index α when possible. To do this, we use `scatfit`¹³ (Jankowski 2022). Since bursts with low S/N or narrowband bursts might not allow for such analysis, we only use frequency subbands where the S/N > 3.5.

We define the width of each burst component as the full width at tenth maximum (FWTM) of the fitted Gaussian for consistency with the First CHIME/FRB Catalog (CHIME/FRB Collaboration et al. 2021), plus a factor $\tau_{sc} \ln 10$ to take into account the scatter broadening. The total width of the burst is defined as follows in the general case of a multi-component burst:

$$\mathcal{W} \text{ (ms)} = t_f - t_0 + (\text{FWTM}_0 + \text{FWTM}_f)/2 + \tau_{sc} \ln 10, \quad (5)$$

where t_0 and t_f are respectively the arrival time of the first and last subcomponents of the burst, and FWTM_0 and FWTM_f the full width at tenth maximum of the first and last components, respectively. For a single component burst and the independent burst subcomponents, the total width is defined as:

$$\mathcal{W} \text{ (ms)} = \text{FWTM} + \tau_{sc} \ln 10. \quad (6)$$

If the scattering timescale of the FRB is unresolved, the term depending on τ_{sc} in Eq. 5 and 6 equals zero. Section 5.6 details the results of this analysis.

4.5. Frequency structure

The frequency structure of the detected FRBs provides information about the intrinsic burst spectrum and bandwidth, as well as phase modulations that could be intrinsic or produced by the propagation of the radio waves through the turbulent interstellar medium (ISM), known as scintillation. We obtain the FRB spectra $S(\nu)$ by averaging their frequency structure over the total

burst duration \mathcal{W} defined in Section 4.4. In the case of bursts with a frequency extent narrower than the observing bandwidth, we fit the averaged spectrum to a Gaussian and a power law, and select the function with the lowest BIC. In the case of a Gaussian fit, we define the burst peak frequency and the burst bandwidth respectively as the centre and the FWTM of the fitted Gaussian. For the power law spectral fits, we report the resulting spectral index, Γ .

To determine the scintillation bandwidth, we compute the auto-correlation function (ACF) of all burst spectra, removing the zero-lag frequency value, and fit the central peak to a Lorentzian. We define the scintillation bandwidth $\Delta \nu_{sc}$ as the half width at half maximum (HWHM) of the fitted Lorentzian. The ACF is defined as follows (see Section 4.2.2 from Lorimer & Kramer 2004, and references therein):

$$\text{ACF}(\Delta \nu) = \frac{\sum_{\nu} (S(\nu))(S(\nu + \Delta \nu))}{\sqrt{\sum_{\nu} (S(\nu))^2 \sum_{\nu} (S(\nu + \Delta \nu))^2}}, \quad (7)$$

where $S(\nu)$ is the burst averaged spectrum at frequency ν and $\Delta \nu$ the frequency lag. In the case of multi-component bursts, we assume the scintillation to be the same for all subcomponents, since the subcomponent separation is small compared to the typical scintillation timescales of a few minutes observed in Galactic pulsars (Narayan 1992; Bhat et al. 1998), and observed differences in frequency structure do not appear to change between subcomponents, as might be the case from an intrinsic structure. The scintillation analysis results are summarised in Section 5.4.3.

For every FRB that is detected away from boresight, the spectrum we analyse is provided by an SB that is composed from the bands of several TABs (cf. Sect. 2). The number of combined TABs ranges from 0 (the central SB) to 8 (an outer SB). These TABs overlap but have some roll-off (see van Leeuwen et al. 2023). Variations in S/N with frequency of order 10% may be introduced throughout the band, between the edge and peak of each subsequent TABs.

4.6. Polarisation

For any ARTS observation, the Stokes I data, or total intensity, are always saved as filterbank files. However, the Stokes Q , U , and V data are only saved if AMBER identifies a candidate with S/N > 10, a duration < 10 ms, and a DM greater than 1.2 times the predicted Milky Way contribution in the direction of the FRB according to the YMW16 electron density model Yao et al. (2017). Such a detection triggers data dumps of the four Stokes parameters (see van Leeuwen et al. 2023).

The Stokes parameters allow us to carry out polarisation analyses, and thus are a powerful tool for understanding the properties intrinsic to the FRBs and the environment where they live. This includes estimating the Faraday rotation measure (RM, rad m^{-2}), the linear ($L = \sqrt{Q^2 + U^2}$) and circular (V) polarisation intensities, and studying the polarisation position angle (PPA, ψ) evolution.

The RM (rad m^{-2}) measures the integrated strength of the magnetic field parallel to the line of sight along the propagation path (e.g. Petroff et al. 2019). In the case of a source located at a redshift $z = z_{\text{src}}$, the RM can be expressed as (Mckinven et al.

¹³ `scatfit`: <https://github.com/fjankowski/scatfit>

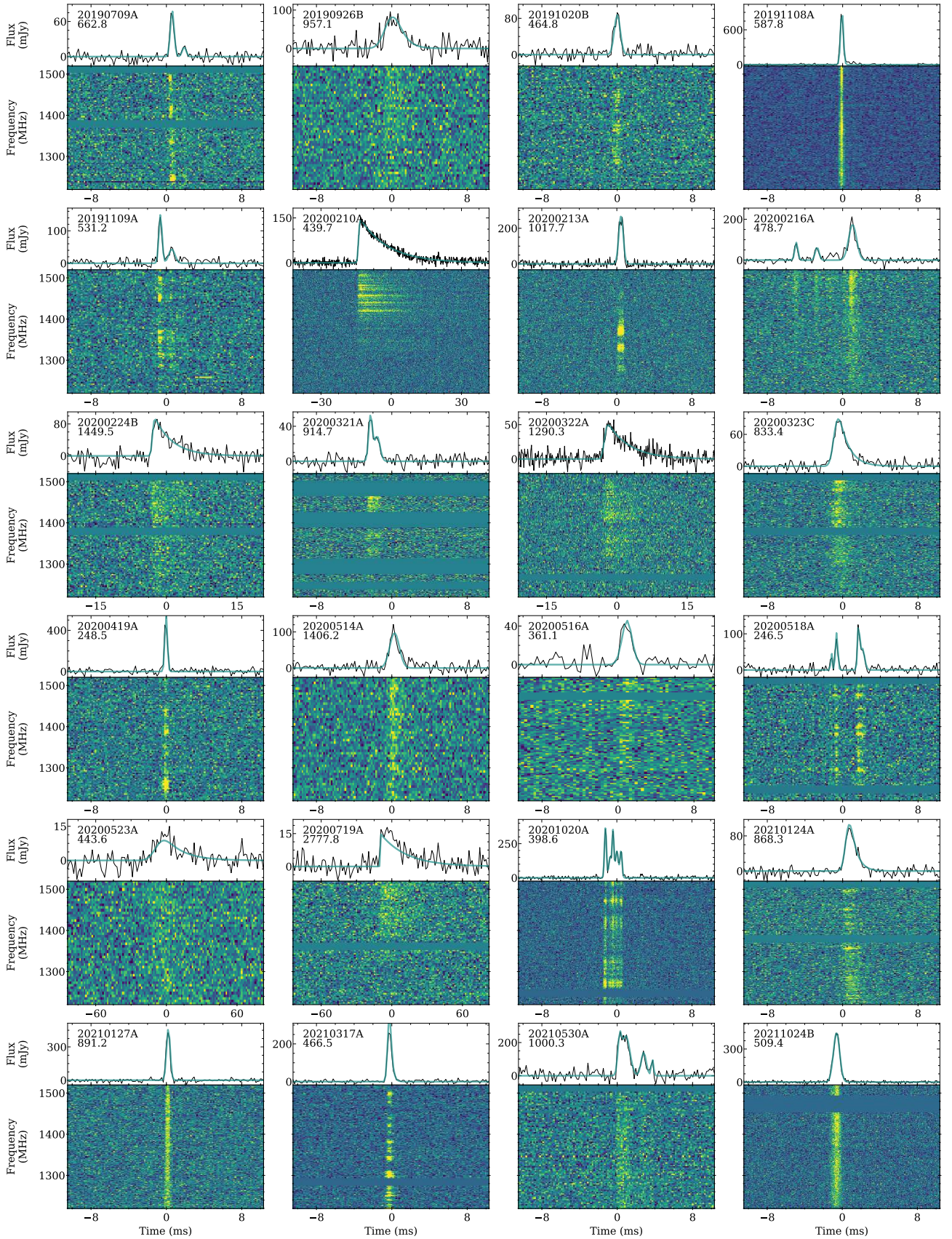


Fig. 3. Dynamic spectra of all FRBs detected with Apertif. Each top panel shows the averaged pulse profile in black, and the fitted pulse profile in teal. The FRB TNS name is indicated on the top left corner, and the DM (pc cm^{-3}) it has been dedispersed to below the name. Each bottom panel shows the dynamic spectrum of the FRB, with the data rebinned in time and frequency to optimise the visibility of the bursts.

2021):

$$\text{RM} = -C_R \int_0^{z_{\text{src}}} \frac{n_e(z) B_{\parallel}(z) dl}{(1+z)^2} dz, \quad (8)$$

with $C_R = 811.9 \text{ rad m}^{-2}/(\mu\text{G pc cm}^{-3})$, n_e the free electron density along the line of sight, B_{\parallel} the magnetic field strength parallel to the propagation path, and $dl(z)$ the distance element along the line of sight at redshift z .

The RM is observed as oscillations in the Q and U intensities, periodic on λ^2 , with λ the observed wavelength in metres. For FRBs where we observe oscillations in the Q and U intensities, we apply the RM synthesis method to estimate the Faraday rotation (see [Burn 1966](#); [Brentjens & Bruyn 2005](#)). This technique applies the equivalent of a Fourier transformation to the complex linear polarisation, $P(\lambda^2) = Q(\lambda^2) + iU(\lambda^2)$, though this expression only has a physical meaning for $\lambda^2 \geq 0$;

$$F(\phi) = \int_{-\infty}^{+\infty} P(\lambda^2) e^{-2i\phi\lambda^2} d\lambda^2, \quad (9)$$

where $|F(\phi)|$ is the total linearly polarised intensity within the observed bandwidth after Faraday de-rotating $P(\lambda^2)$ by the Faraday depth ϕ (rad m^{-2}). The complex linear polarisation can also be written as $P(\lambda^2) = |P|e^{2i\psi}$, with the PPA $\psi(\lambda^2) = \psi_0 + \text{RM}\lambda^2$, and ψ_0 the polarisation position angle at a reference frequency. A Faraday dispersion function (FDF) is built by computing $F(\phi)$ at different ϕ and ψ trial values, and the RM and ψ_0 are given by the (ϕ, ψ) values that maximise the FDF. To determine the best RM value and errors, we fit the FDF peak to a parabolic curve.

Once the (RM, ψ_0) solution has been found, the Stokes Q and U can be Faraday de-rotated, and the resulting $L/I = \sqrt{Q^2 + U^2}/I$ will give us the linear polarisation fraction. The circular polarisation fraction will in turn be given by V/I . The PPA can be expressed as a function of time t and frequency ν as follows:

$$\psi(t, \nu) = \frac{1}{2} \tan^{-1} \frac{U(t, \nu)}{Q(t, \nu)}. \quad (10)$$

After Faraday de-rotating Stokes Q and U , we can study the PPA evolution with time. This PPA is given by the polarisation angle of the emission at the source, and it is thus a property intrinsic to the FRB. It is set by the properties of the magnetic field in the emission regions, since the plane of the linear polarisation coincides with the local plane of curvature of the magnetic field lines. This holds true both for pulsar-like and synchrotron maser emission mechanisms.

Once we obtain the observed source RM (RM_{obs}), we compare this to the expected MW contribution in the direction of each burst (RM_{MW}) using the Faraday rotation map from [Hutschenreuter et al. \(2022\)](#). We then convert the resulting RM to the FRB redshift expected from the Macquart relation (z):

$$\text{RM}_{\text{host}} = (\text{RM}_{\text{obs}} - \text{RM}_{\text{MW}}) \times (1+z)^2 \quad (11)$$

The Stokes data must be calibrated for leakage between the different Stokes parameters before applying any polarisation analysis. The calibration is performed using a linearly polarised calibrator (we used 3C286 or 3C138), and an unpolarised calibrator (3C147). A phase difference between the x and y complex gains will result in leakage between V and U , and this phase can be solved with a source with linear but no circular polarisation. On the other hand, an unpolarised source will determine the gain amplitude difference between the x and y feeds, and

thus the leakage of I into Q . We only started adding the unpolarised source to the calibration observations from April 2020, so all FRBs from earlier dates have no I/Q leakage correction. After any new FRB detection, scheduling constraints permitting, we carried out observations on and off the linearly polarised and unpolarised calibrators. The calibrators were placed at the centre of the CBs where the FRB had been discovered. This centre corresponds to SB 35, though the FRBs were often detected in different SBs. We thus made the assumption that there is a negligible leakage difference between the central and surrounding SBs.

Upon detailed analysis and calibration of the Stokes data, after the survey completion, we concluded that this assumption did not always hold true. In some cases, after calibrating the U/V leakage, a residual V signal oscillating with frequency at the same rate as Q was still observed, which is not consistent with expected physical phenomena (e.g. Faraday conversion is expected to be much smaller than Faraday rotation at our observing frequencies, [Gruzinov & Levin \(2019\)](#)). In those cases, we applied a technique in which we identified a frequency dependent phase minimising the V oscillations, and rotated Stokes U/V by the resulting phase. To test this technique, we applied it to FRB 20191108A ([Connor et al. 2020](#)), which was detected in SB 37 but calibrated with the linearly polarised calibrator 3C286 observed in SB 35. Using this technique to minimise the circular polarisation, we find a linear polarisation fraction $L = 86 \pm 2\%$, higher than the original 50%, and a circular polarisation fraction consistent with 0 ($V = 5 \pm 7\%$), stricter than the originally reported limit of $\lesssim 13\%$. The rotation measure computed through RM synthesis is $+473.1 \pm 2.2 \text{ rad m}^{-2}$, consistent with the $+474 \pm 3 \text{ rad m}^{-2}$ obtained through a least square fit of the position angle as a function of λ^2 in [Connor et al. \(2020\)](#). In this way we validated the technique that we subsequently applied to several FRBs.

5. Results

Between July 2019 and February 2022, a total of 24 new FRBs were discovered within the ALERT survey. This number includes FRB 20190709A, FRB 20190926B, FRB 20191020B, FRB 20191108A, FRB 20191109A, and FRB 20201020A that were reported in previous publications ([van Leeuwen et al. 2023](#); [Connor et al. 2020](#); [Pastor-Marazuela et al. 2023](#)). The dynamic spectra and fitted pulse profiles of all 24 FRBs are presented in Fig. 3. All FRBs were followed up with Apertif observations for 30 h up to 450 h, but none were seen to repeat. The bursts display different morphologies, including broadband and narrow-band single components, and a high fraction of bursts with multiple components peaking at the same frequency. These morphologies are typical of the one-off FRBs in the First CHIME/FRB catalogue ([Pleunis et al. 2021a](#)); the lack of observed repetitions thus reinforces this apparent relation between morphology and repetition. Additionally, the bursts display a broad range of propagation properties that we will discuss below. In this Section, we first describe in detail the properties of some of the FRBs in our sample with remarkable features (Section 5.1), and next the properties of the FRB ensemble from Section 5.2 onwards.

5.1. FRBs of special interest

This section describes individual FRBs in our sample ordered by detection date, with the exception of some FRBs with similar features grouped in a single subsection at the end.

5.1.1. FRB 20200210A

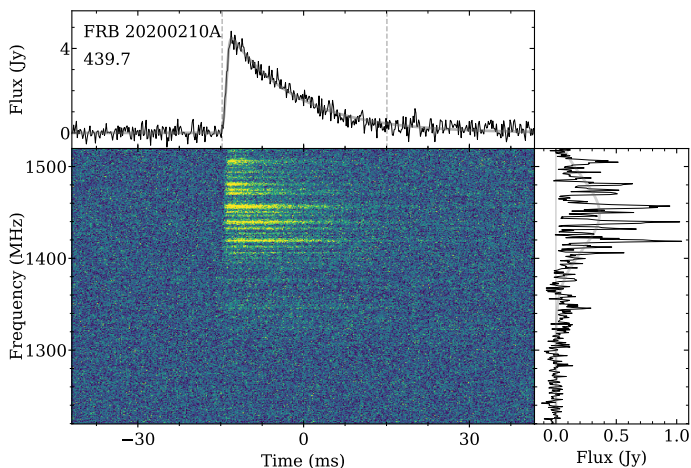


Fig. 4. Dynamic spectrum of FRB 20200210A. The top panel shows the average pulse profile, with a transparent grey line representing the fit to a scattered Gaussian, and the vertical dashed lines the initial and final times of the burst from which the spectrum is extracted. The text indicates the TNS name and the DM (pc cm^{-3}) of the burst. The bottom right panel shows the spectrum extracted between the two dashed lines in the pulse profile, and its fit to a Gaussian in grey. We associate the large intensity fluctuations to scintillation in the Milky Way. The bottom left panel is the dynamic spectrum.

This FRB (Fig. 4) presents a rare set of properties. It displays both temporal broadening from multi-path propagation, with $\tau_{\text{sc}} = 12.6 \pm 0.3$ ms, as well as a scintillation pattern with $\Delta\nu_{\text{sc}} = 1.6 \pm 0.1$ MHz, which indicates the burst has traveled through two distinct scattering screens. Furthermore, it is a narrowband burst, with a bandwidth of ~ 170 MHz. The scattering timescale is uncommonly large for its DM of 439.7 pc cm^{-3} . Such a large scattering timescale at 1370 MHz cannot be explained by the Intergalactic Medium (IGM) or an intervening galaxy halo; we thus associate the first scattering screen with the host galaxy. The scintillation bandwidth falls within the expected ranges from the YMW16 (Yao et al. 2017) and NE2001 (Cordes & Lazio 2003) electron density models; the scattering screen producing scintillation is thus likely to be located in the Milky Way.

Scintillation can only occur when the scattering diameter by the first scattering screen is unresolved by the second, and this permits us to put constraints on the distance between the FRB and the first scattering screen (Masui et al. 2015; Cordes & Chatterjee 2019). Cordes & Chatterjee (2019) determine the source size requirements for scattering and scintillation to be present at the same frequency band:

$$\tau_X \tau_G < \frac{1}{(2\pi\nu)^2} \frac{d_{so}^2}{L_X L_G} \simeq (0.16 \text{ ms})^2 \left(\frac{d_{so}^2}{\nu^2 L_X L_G} \right), \quad (12)$$

where τ_X and τ_G are respectively the extragalactic and Galactic scattering timescales in ms, ν is the observing frequency in GHz, d_{so} the angular diameter distance from source to observer in Gpc, and L_X and L_G the distances of the lenses to the source and the observer respectively, in kpc. We want to determine the distance upper limit between the source and the first scattering screen it encounters, L_X . Scintillation bandwidths can be converted to scattering timescales with the following equation:

$$\tau_{\text{sc}} = C_1 / 2\pi \Delta\nu_{\text{sc}}, \quad (13)$$

where C_1 is a constant with a value close to unity that depends on the medium scattering properties, and we assume $C_1 = 1$ for a thin scattering screen (Eq. 8 from Cordes & Rickett 1998; Lorimer & Kramer 2004, Section 4.2.3).

In the case of FRB 20200210A at a frequency $\nu = 1.37$ GHz, we have the extragalactic scattering timescale $\tau_X = 12.6 \pm 0.3$ ms, and the Galactic scintillation bandwidth $\Delta\nu_{\text{sc}} = 1.6 \pm 0.1$ MHz, which yields $\tau_G = 0.1 \mu\text{s}$. Given the Galactic latitude of the FRB, the scintillation is likely produced in the Milky Way thick disk, at $L_G \sim 1$ kpc (Ocker et al. 2022b). From the extragalactic DM of the FRB alone, we estimate a redshift of $z_{\text{Macquart}} = 0.36$, and thus an angular diameter distance upper limit of $d_{so} = 1.09$ Gpc. By using these values in Eq. 12, we find an upper limit on the distance between the FRB and the scattering screen at its host galaxy of $L_X \lesssim 12$ kpc. However, the presence of scattering allows us to use a joint scattering-dispersion redshift estimator. We do this by applying the method described in Cordes et al. (2022), and assume a lognormal probability density function (PDF) for the scattering parameter $\phi_\tau \equiv \tilde{F}G$. We find the estimated median redshift to be $z = 0.11$, which corresponds to an angular diameter distance of $d_{so} = 0.43$ Gpc. With this new redshift constraint, we find the distance upper limit between the FRB and its scattering screen to be just ~ 2 kpc. This is fully consistent with scattering in the host galaxy, even for a dwarf host, although it is not constraining enough to determine if the scattering originated in the circumburst environment.

The high S/N of this FRB allowed us to subdivide the burst into several frequency subbands to perform a fit of the scattering index (See Appendix D and Fig. 4). We determined a robust measurement of the scattering index, $\alpha = 13.8 \pm 0.9$. This scattering index is anomalous when compared to the pulsar population, and it will be further discussed in Section 6.1.3. In the top panel of Fig. D, we notice that the two lower frequency subbands display wider fitted Gaussian components. This could indicate the presence of a second component at those frequencies, unresolved due to scattering. However, it is unclear how such component would affect the measured scattering index, since it will depend on its relative amplitude and frequency extent (Oswald et al. 2021). Even when removing those two subbands from the fit, we obtain a similar α .

We localised this FRB to an error region of 0.78 arcmin^2 , centred at the coordinates $18:53:59.4 +46:18:57.4$ in RA (hms) and DEC (dms). We find one galaxy, G2, contained within the error region, at a photometric redshift of 0.40. This is close to the upper limit set by the Macquart relation assuming $\text{DM}_{\text{host}} = 100 \text{ pc cm}^{-3}$, $z_{\text{Macquart}} = 0.36_{-0.22}^{+0.10}$, but much higher than expected from the scattering. However, there are two additional galaxies within $7''$ of the error region and the z_{Macquart} upper limit. G3 is located $1''$ from the error region and has $z_{\text{phot}} \sim 0.46$, while G1 is $7''$ away from the error region and has $z_{\text{phot}} \sim 0.11$. The latter has a Kron radius (Kron 1980) of $6.1''$, placing it very close to the FRB localisation region. Since we have performed no astrometric corrections, the galaxy could well be inside the FRB error region. After performing a PATH analysis, assuming an unseen prior $P(U) = 0.01$ given the expected low redshift of the galaxy, we find the most likely host to be G1, with $P(G1|x) = 0.58$. The host galaxy candidates and PATH results are presented in Table B, while the FRB localisation region and the host galaxy candidates are shown in Fig. 5.

5.1.2. FRB 20200213A

This FRB (Fig. 6) is the most narrow-banded of the sample. It has a bandwidth of 145 MHz, less than half of the total ob-

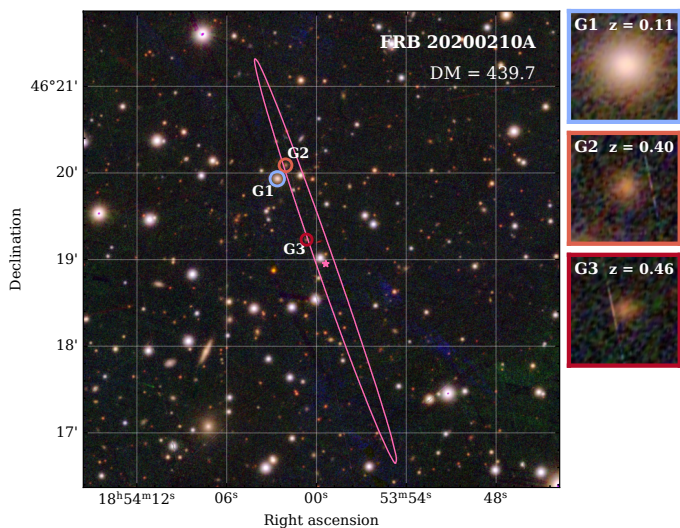


Fig. 5. Localisation region (pink contour) of FRB 20200210A. The three galaxies within $7''$ of the error region are marked with circles, coloured ranging from bluer (lower redshift) to redder (higher redshift), with the galaxy ID (same as in Table B). The subplots (right) are zoomed images of these three galaxies, with $12''$ FoV, and border colour matching the main-panel circles. Each galaxy ID and photometric redshift are indicated at the top.

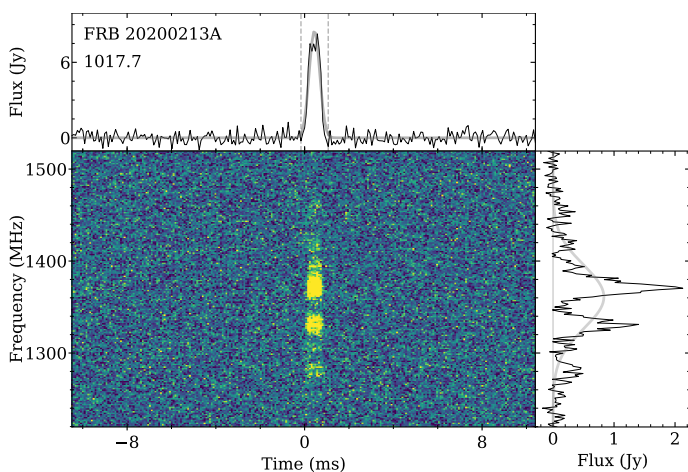


Fig. 6. Dynamic spectrum of FRB 20200213A. The pulse profile and the spectrum are both fitted to a Gaussian.

serving bandwidth. Additionally, it displays a strong frequency modulation, with two main patches of similar intensity and an array of lower intensity patches above and below the central ones. The frequency modulation has a 19 MHz bandwidth, significantly larger than the 4 MHz Δv_{sc} predicted by the NE2001 model (YMW16 predicts 1 MHz). This suggests that either the Galactic ISM is more uniform than predicted by the electron density models, or that the frequency structure is intrinsic to the source. The temporal structure of the burst presents a single component with a flat peak. Given the DM of $1017.7 \text{ pc cm}^{-3}$ and the instrument frequency resolution of 195 kHz, the FRB width is close to the dispersion broadening (Petroff et al. 2019). The flat peak could thus be a result of instrumental smearing instead of the intrinsic structure of the burst, or be the signature of a second or even third component indistinguishable from the first.

The detection of this burst in SB 48 triggered the storage of the Stokes data. Subsequently, we scheduled observations of the linearly polarised calibrator 3C138 in SB 35. The calibrated Stokes data is presented in Appendix Fig. C.1. Since we observe a faint indication of Q/U oscillations, we applied the RM synthesis algorithm to the frequency channels where the burst is bright enough; we selected a frequency extent contained within the FWTM of the spectrum fitted to a Gaussian, between 1291 and 1436 MHz. We find a resulting RM of $300.3 \pm 2.1 \text{ rad m}^{-2}$, and after Faraday de-rotating we obtain linear and circular polarisation fractions of $L = 10 \pm 3\%$ and $V = 8 \pm 6\%$ respectively. These results are shown in Appendix fig. C.2. Given the expected MW contribution $RM_{MW} \sim -17 \text{ rad m}^{-2}$ in the direction of the FRB, the RM in the host galaxy could be as high as $RM_{\text{host}} = 1461^{+380}_{-576} \text{ rad m}^{-2}$ for the expected redshift range $z_{\text{Macquart}} = 1.15^{+0.24}_{-0.58}$. Since the polarised fraction is low and the burst is narrowband, we advise caution when interpreting this RM.

We localised this burst to a small area of 0.94 arcmin^2 . However, since the FRB could be located at a redshift as high as ~ 1.4 , we identify nine galaxies in the error region as host galaxy candidates. Dimmer galaxies, too faint to appear in the Pan-STARRS1 catalogue, could also exist in the area. These results are included in the overview Figure of FRB localisations and host galaxy candidate positions, Fig. 16.

5.1.3. FRB 20200216A

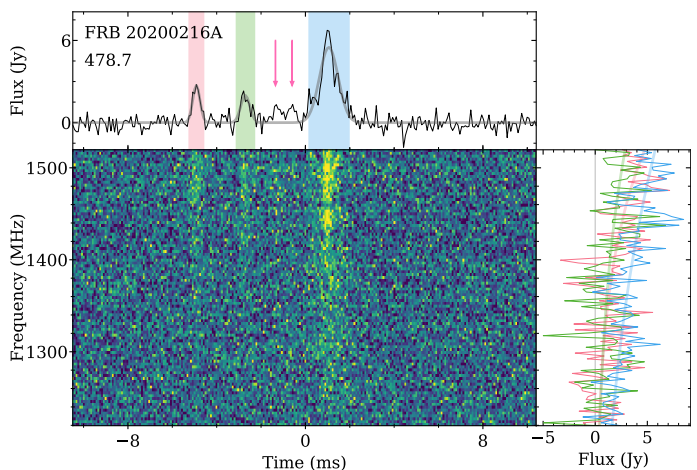


Fig. 7. Dynamic spectrum of FRB 20200216A. On the pulse profile (top panel), each coloured shaded region shows a distinct component and fitted to a Gaussian. Their respective spectra are shown on the bottom right panel with the same colour, and fitted to a power law (transparent solid lines). The two pink arrows on the pulse profile indicate the position of the two potential subcomponents between the precursors and the main component.

This FRB consists of a bright main burst subcomponent with two narrow precursors of about a third of the amplitude of the main burst, as can be seen in Fig. 7. The separation between the two precursors is $\sim 2.2 \text{ ms}$, while the main component arrives $\sim 3.8 \text{ ms}$ after the second precursor. The pulse profile appears to contain two bumps between the second precursor and the main component, but their amplitude is too low to be identified as real subcomponents. We carried out a timing analysis identical to the one described in Pastor-Marazuela et al. (2023), where the presence of a periodicity in FRB 20201020A was investigated, in-

cluding the power spectrum analysis and the study of the time separation between subcomponents, but we find no evidence of periodicity in this burst.

The spectrum of each of the FRB 20200216A subcomponents can be well fitted by a power law. The power law spectral indices of the first, second, and third components are respectively 11.6, 8.7 and 5.6. The precursors seem to peak at higher frequencies than the main subcomponent, reminiscent of the downwards drifting effect typically observed in repeating FRBs (e.g. Hessels et al. 2019). However, the main subcomponent is brighter at the top of the band. The lack of visible emission at the bottom of the band of the two precursors could be simply explained by their lower amplitude, which is below the noise level at lower frequencies. The emission of each component is likely to peak at similar frequencies, but above the highest observing frequency. We further applied Gaussian function fits to the spectra, but the BIC favours a power law model for all components. We thus identify the morphology of this FRB as a multi-component burst with components peaking at the same frequency (Pleunis et al. 2021a).

Given the DM, the expected MW and halo contribution to the DM, and assuming a host galaxy contribution of 100 pc cm^{-3} in the host frame, the expected redshift for this FRB is $z_{\text{Macquart}} = 0.44^{+0.12}_{-0.24}$. We localised it to an error region of 2.34 arcmin^2 around the coordinates $22:08:24.7 + 16:35:34.6$ in RA and DEC, within which we identify one galaxy, with a photometric redshift $z_{\text{phot}} = 0.52 \pm 0.09$, consistent with the expected limits, that we label G3. We find three additional galaxies within $5''$ of the error region, at similar redshifts of $z \sim 0.5$. After running a PATH analysis, we find the brightest and nearest of the galaxies, labeled G1, to be the most likely host, with $P(G_1|x) \sim 0.42$. This galaxy is located $4''$ away from the error region, and has a photometric redshift $z_{\text{phot}} \sim 0.49$. G3 is the second brightest and second most likely host, with $P(G_3|x) \sim 0.37$. Since these posterior probabilities are similar, we cannot confidently identify the host galaxy of FRB 20200216A. The details on the host galaxy candidates and PATH analysis are presented in Table B.

The detection of FRB 20200216A triggered a full-Stokes data dump. Subsequently we scheduled on/off observations of the linearly polarised source 3C286 to calibrate the UV leakage. We observe quick oscillations in the sign of Stokes Q and U in the main component of the burst after calibration, which we associate with Faraday rotation (See Appendix Fig. C.1). We selected the frequency channels contained within the full width at fifth maximum (FWFM) of a Gaussian fit to the spectrum of the main component, which are all those above 1347 MHz, and then we performed the RM synthesis technique on the data. We find the best solution to be $\text{RM} = -2051 \pm 6 \text{ rad m}^{-2}$, as shown in Fig. 8. After Faraday de-rotating, we obtain linear and circular polarisation fractions of $38 \pm 6\%$ and $11 \pm 4\%$ respectively for the main component. The polarisation fraction of the two fainter precursors appears to be slightly lower. Although the linear polarisation fraction is low and the frequency extent of the burst is narrow, the resulting RM and ψ_{PPA} match well the phase between Stokes Q and U. This is the second largest RM ever measured in a one-off FRB to date (Sherman et al. 2024; Mckinven et al. 2021). The expected RM_{MW} contribution in the direction of the burst is $-36 \pm 10 \text{ rad m}^{-2}$, totalling $\sim -2015 \text{ rad m}^{-2}$ from an extragalactic origin. Assuming that the extragalactic RM originates from the host galaxy, this would translate to an RM of $\sim -4200^{+1300}_{-800} \text{ rad m}^{-2}$ in the host reference frame at z_{Macquart} . Three repeating FRBs with high or extreme RM values have been associated to persistent radio sources (PRs, Marcote et al. 2017; Niu et al. 2022; Bruni et al. 2023), and hence finding

a galaxy within the error region associated with such a radio source might be a strong indication that the FRB was produced in that galaxy. The field is not covered by an Apertif imaging survey (see Sect. 5.2). We searched for radio emission within the error region of the FRB in the Rapid ASKAP Continuum Survey (RACS) Mid (Duchesne et al. 2023), but we found no radio source associated to any of the host galaxy candidates.

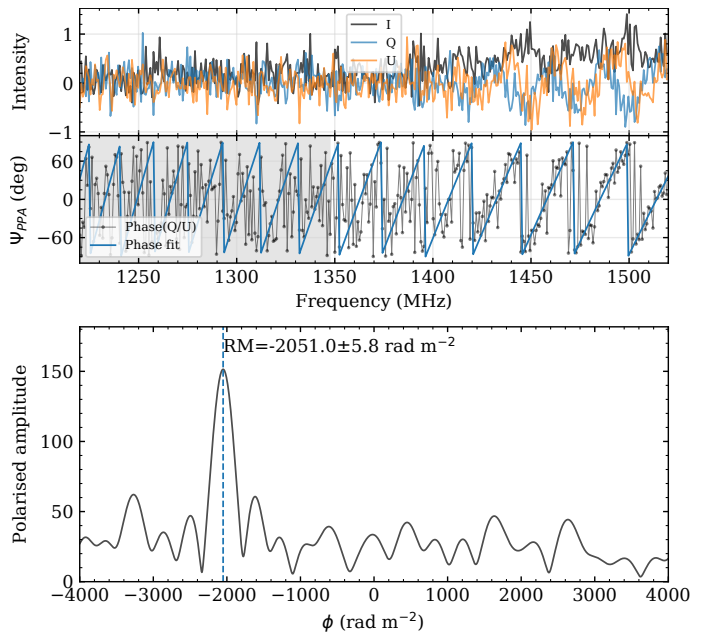


Fig. 8. Measured polarisation properties of FRB 20200216A. Only frequencies above 1347 MHz were used for RM synthesis, since there is not enough signal below that frequency.

5.1.4. FRB 20200419A

This FRB with a low DM of 248.5 pc cm^{-3} consists of a single component with a width of 0.58 ms and no measurable scattering. The burst is broadband, with an intensity that fluctuates with frequency with a decorrelation bandwidth of 7.5 MHz, slightly higher than the expected 2.4 MHz from the NE2001 model. Upon detection of the burst, the full-Stokes data were saved, and observations of both the linearly polarised calibrator 3C286 and the unpolarised calibrator 3C147 were carried out. The burst is highly polarised, with a linear polarisation fraction of $L = 77 \pm 6\%$ and null circular polarisation fraction $V = 4 \pm 6\%$. All the linear polarisation is observed in Stokes Q, and thus no RM can be measured.

We localised this FRB to an ellipse centred around $19:00:34.2 + 81:43:20.5$ in RA and DEC with a 1.29 arcmin^2 error region. The expected redshift from the Macquart relation is $z_{\text{Macquart}} = 0.08^{+0.04}_{-0.06}$, but we find no known galaxies at such low redshift within the FRB error region. The lowest redshift galaxy we identify has a photometric redshift $z = 0.15 \pm 0.03$, consistent with the expected redshift within errors, and we find no other host galaxy candidates within $10''$ of the error region. A PATH analysis determines that the galaxy is $\sim 70\%$ likely to be associated with the FRB. Given the low DM of the FRB and the depth of the Pan-STARRS catalogue, we assumed a very small unseen prior, $P(U) = 0.001$, since even dwarf galaxies would be detected at such low redshift (See Table B for details). The host galaxy candidate would be a good target for optical follow-

up to determine its spectroscopic redshift. A confirmation of the galaxy redshift might indicate a lower DM contribution from the MW or the halo, or a host galaxy contribution $<100 \text{ pc cm}^{-3}$, or a combination of both. The FRB error region and host galaxy candidate are shown in Fig. 11.

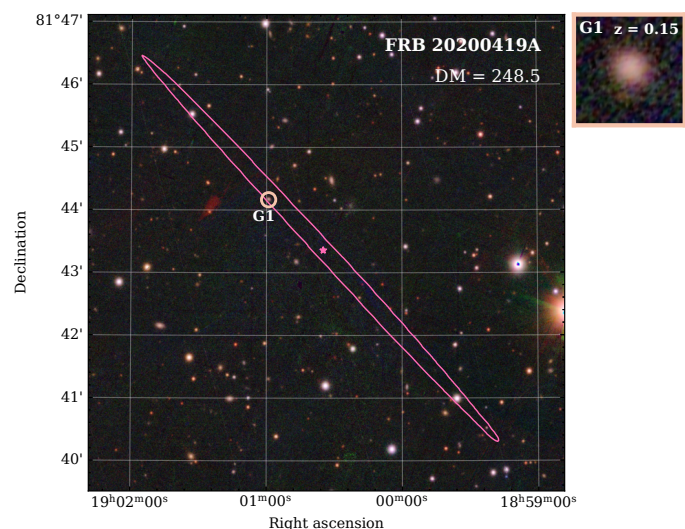


Fig. 9. Localisation region (pink contour) of FRB 20200419A, and host galaxy candidate G1.

5.1.5. FRB 20200514A

FRB 20200514A was detected with a DM of $1406.2 \text{ pc cm}^{-3}$ as a single component burst with a total width of 2.2 ms. Although the burst is broadband, it becomes brighter at the top of the band. Its detection triggered the dump of the Stokes data, and after calibration with the linearly polarised 3C286 and the unpolarised 3C147, we observe rapid oscillations of Q and U with frequency (See Fig. C.1). After applying RM synthesis, we obtain an $\text{RM} = 966.1 \pm 20.5 \text{ rad m}^{-2}$, although the FDF shows significant secondary peaks (See Fig. C.3). Assuming the reported RM, we measure polarisation fractions of $L = 51 \pm 5\%$ and $V = 21 \pm 9\%$. The expected MW contribution to the RM in the direction of the burst is $\sim -215 \text{ rad m}^{-2}$, resulting in an extragalactic RM of $\sim 765 \text{ rad m}^{-2}$. Given the high excess DM of the burst, its expected redshift is $z_{\text{Macquart}} = 1.35^{+0.30}_{-0.66}$. Hence, if we assume the RM to be produced within the FRB host galaxy, it could be as high as $\text{RM}_{\text{host}} = 6500^{+2000}_{-3200} \text{ rad m}^{-2}$. The PPA remains roughly flat, with a marginal decrease of $\sim 5^\circ$ along the burst duration.

5.1.6. FRB 20200518A

This FRB consists of two groups of two narrowly spaced sub-components each. The space between the two groups is $\sim 2.3 \text{ ms}$, while the space between the sub-components of each group is 0.54 ms on the first and 0.34 ms on the second. In the first group, the second component has a larger amplitude, while the first component of the second group is the brightest of all four. The power spectrum of the average pulse profile presents several peaks, but each one corresponds to the separation between different components. The timing analysis does not provide evidence for periodicity.

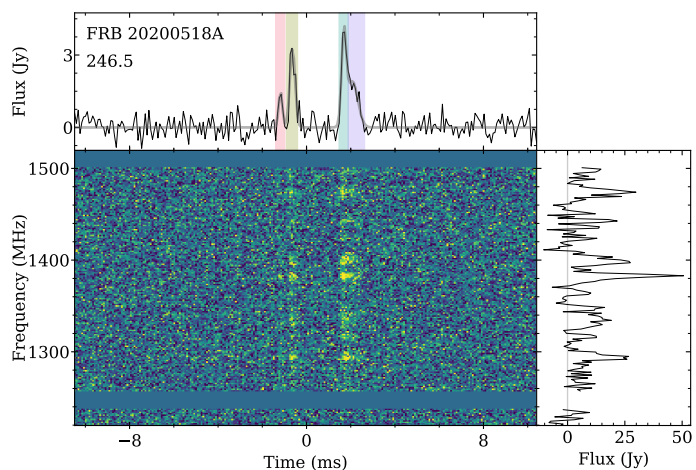


Fig. 10. Dynamic spectrum of FRB 20200518A. On the pulse profile, each of the four components is marked by a coloured shaded region, and fitted to a Gaussian. The spectrum on the bottom right panel is the sum of all components.

All four subcomponents present a similar frequency extent. The peak frequency of the emission cannot be easily determined since the burst presents strong frequency modulations that we associate with scintillation, with a decorrelation bandwidth of $\Delta\nu_{\text{sc}} = 5 \pm 2 \text{ MHz}$. This matches the expected Milky Way contribution of $\sim 4 \text{ MHz}$ from NE2001 (Cordes & Lazio 2003). The burst shows no evidence of scatter broadening at the Apertif resolution.

With a DM of 246.5 pc cm^{-3} , it is the least dispersed burst of our sample. We localised this FRB to a narrow ellipse with a localisation area of 1.67 arcmin^2 centred at the coordinates $09:36:45.3 +77:22:36.8$ in RA and DEC. Given the source redshift and expected MW and halo contributions, we derive $z_{\text{Macquart}} = 0.10^{+0.04}_{-0.08}$. Although we found no galaxies within the error region and redshift limit, we identified two galaxies with photometric redshifts ~ 0.08 within 3.5" and 8" of the nominal error region edge, which given the astrometric uncertainty, could well be inside the actual error ellipse. The FRB localisation region and the two host galaxy candidates are shown in Fig. 11. We ran a PATH analysis on the two candidates assuming a small unseen prior, $P(U) = 0.01$, given the low expected redshift. We found that both galaxies have a similar likelihood of being the host, with $P(G_1|x) \sim 0.42$ and $P(G_2|x) = 0.56$, as detailed in Table B.

The Stokes data were saved after the detection of this burst, but unfortunately no calibration observations were carried out. The raw Stokes data show signal in I, Q, and V. By assuming the circular polarisation to be 0, we apply the method to find the phase that would minimise V. As a result, we obtain a linear polarisation fraction $L = 72 \pm 12\%$, and a residual circular polarisation fraction $V = 29 \pm 17\%$. This would represent a highly linearly polarised burst if our assumptions are correct. The burst does not display any significant Q/U modulations with frequency, and thus no RM can be estimated. The first group of components appears to show a higher linear polarisation fraction than the second one, although the latter also displays a peak in V that could be an inaccuracy of the calibration procedure. The resulting PPA remains constant between the two component groups. The Stokes data calibrated through the circular polarisation minimisation technique are shown in Fig. C.1.

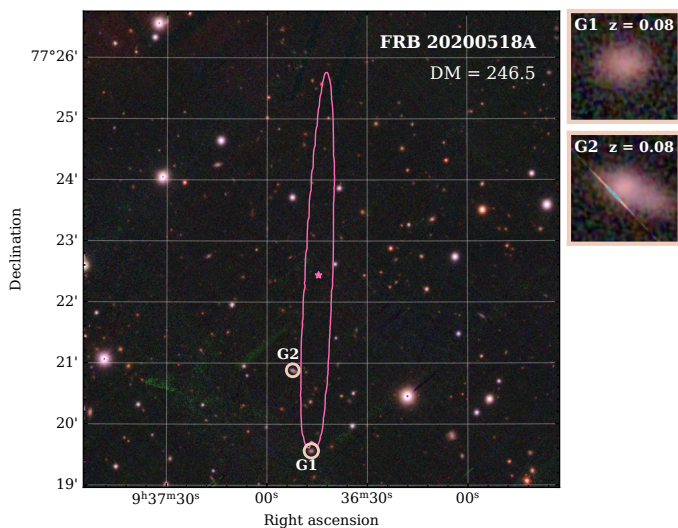


Fig. 11. Localisation region (pink contour) of FRB 20200518A and two host galaxy candidates.

5.1.7. FRB 20200719A

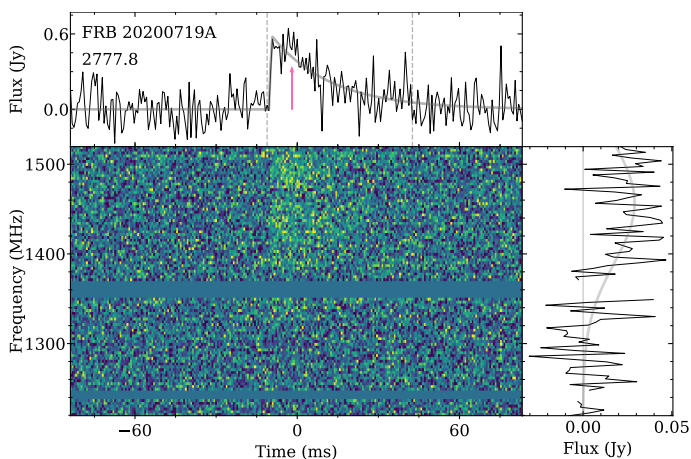


Fig. 12. Dynamic spectrum of FRB 20200719A. The pulse profile is fitted to a scattered Gaussian. The pink arrow indicates the position of an excess emission that might be explained by a second component merged to the first by scattering. The spectrum is fitted to a Gaussian.

FRB 20200719A, with a DM of 2778 pc cm^{-3} , is the most dispersed FRB of our sample, as well as the most scattered, with $\tau_{\text{sc}}=21 \text{ ms}$. It differs by more than 1000 pc cm^{-3} from the Apertif FRB with the second-highest DM. Compared to the FRBs in the TNS¹⁴, it is the FRB with the third-largest DM known to date, after the Parkes 70-cm FRB 19920913A (Crawford et al. 2022) with a DM of 3338 pc cm^{-3} and the CHIME/FRB source FRB 20180906B with a DM of 3038 pc cm^{-3} . The inferred redshift of FRB 20200719A is $z_{\text{Macquart}} \sim 3.26^{+0.62}_{-1.35}$ if we assume a DM_{host} contribution of 100 pc cm^{-3} . The large scattering timescale might however be an indication of a significant contribution to the DM from the host galaxy and the circumburst environment (Cordes et al. 2022; Ocker et al. 2022b), which would place the FRB at a lower redshift. Nonetheless, since the host galaxy contribution to the observed DM evolves

as $\text{DM}_{\text{host}} = \text{DM}_{\text{host,loc}}/(1+z)$ (Deng & Zhang 2014), even a large host local DM contribution would be diluted at high redshift. We can estimate a redshift lower limit assuming the host galaxy has a DM contribution as large as that originally found for the repeating FRB 20190520B (Niu et al. 2022). Even though foreground studies of the FRB 20190520B field have since identified two intervening galaxy cluster halos that reduce the required host DM contribution by as much as 50–70% (Lee et al. 2023), we use the original value here, to be conservative in our limits. The FRB 20190520B host galaxy contributes $\text{DM}_{\text{host}} = 902 \text{ pc cm}^{-3}$ to the observed DM. Since its host is located at $z = 0.241$, the local DM contribution in the host frame is $\text{DM}_{\text{host,loc}} \sim 1119 \text{ pc cm}^{-3}$. If we now assume the host galaxy of FRB 20200719A has a contribution to the DM as large as that originally suggested for FRB 20190520B, its redshift would still be $z_{\text{min}} \sim 2.8^{+0.6}_{-1.2}$. This highly constraining lower limit still places the FRB at very large cosmological distances.

In principle, further increasing $\text{DM}_{\text{host,loc}}$ reduces the required distance, hence further overcoming the $1+z$ dilution in DM_{host} . One might wonder if this double action allows for a reasonable combination of distance and DM_{host} . But even if we place the host at $z=1.0$, the distance of the currently farthest FRB (Ryder et al. 2023), we require a $\text{DM}_{\text{host,loc}}$ of over 2600 pc cm^{-3} , an extreme outlier of known values for $\text{DM}_{\text{host,loc}}$.

The probability of intersecting a foreground galactic halo increases with distance. For instance, the most highly dispersed FRB 20180906B from the CHIME/FRB sample (CHIME/FRB Collaboration et al. 2021) was shown to intersect within 1.4 Mpc of a galaxy cluster (Connor & Ravi 2022). For FRB 20200719A, the possibility of intersecting foreground galaxies is not negligible. We follow Prochaska & Zheng (2019)¹⁵ to determine how likely this FRB is of intersecting an intervening galaxy with a mass greater than the Milky Way within the line of sight (LoS). We use the Aemulus halo mass function (McClintock et al. 2019) to generate galaxy halos with masses between $10^{12} M_{\odot}$ (roughly the MW mass) and $10^{16} M_{\odot}$. Next, we compute the average number of halos expected to occupy the comoving volume at the expected redshift of this FRB, $z_{\text{max}} = 3.26$. If we consider an intersection within the virial radius of the galaxies within the comoving volume, which is the distance at which we expect a foreground galaxy to have a significant contribution to the DM, we find the average number of galaxies to be $N(z) = 2.633$. However, in order to have a significant contribution to scattering, the impact parameter must be lower (Ocker et al. 2021). If we consider 0.15 times the virial radius (roughly 10 times the half mass radius, and between 20 and 40 kpc depending on the mass, Kravtsov 2013), we find $N(z) = 0.059$. Assuming the location of the foreground galaxies within the comoving volume follows a Poisson distribution, the probability that the LoS crosses k halos is given by:

$$P(k|N(z)) = \frac{N^k e^{-N}}{k!}. \quad (14)$$

The probability of intersecting at least one foreground halo is thus given by $P(k \geq 1|N(z)) = 1 - e^{-N}$. We find the probability of at least one intersection within the virial radius of the foreground galaxy to be $\sim 93\%$, and within 0.15 times virial radius it is $\sim 5.8\%$. Foreground galaxies are thus very likely to contribute to the DM of this FRB, while the contribution to scattering is less likely.

¹⁴ Accessed 2023 Nov 01

¹⁵ <https://github.com/FRBs/FRB>

Within the localisation region, we find only two galaxies above a conservative redshift lower limit of 1.6 (at 1.4 ± 0.5 and 0.81 ± 0.96 respectively, see Fig. 16), but with such a high redshift upper limit, roughly 10^3 dwarfs and ~ 50 massive galaxies are expected to be contained within the localisation comoving volume. We thus ran a PATH analysis on the two galaxies assuming a large unseen prior, $P(U) = 0.9$. The brightest galaxy, G2, is found to be the most likely host, with $P(G_2|x) \sim 0.1$, while $P(G_1|x) \sim 2 \times 10^{-4}$, as detailed in Table B. We thus cannot confidently associate FRB 20200719A to any host galaxy.

The spectrum of the FRB can be fitted to a Gaussian peaking at $\nu_{\text{obs}} = 1460$ MHz and with a bandwidth (FWTM) of 260 MHz. Part of the emission thus happens at frequencies above the observing bandwidth. The pulse profile fitted to a single scattered component shows excess of emission after the peak. This might be the signature of a second component that is blurred together with the first due to scattering. By fitting a two-component scattered model, we find a potential component separation of 5.95 ms. However, the BIC of the single component model is marginally lower and hence it is preferred. Assuming a single component scattered burst, we divided the total bandwidth into four subbands and fitted the scattering tail separately in the top two, where there was enough signal to perform the fit. From the difference in scattering timescale between these two subbands, we obtain a scattering index $\alpha = -11.1 \pm 4.5$. In spite of the large error bars, this index is still inconsistent with scattering by a thin screen or a turbulent medium. We will discuss this further in Section 6.1.3.

Given the large distance at which this FRB was emitted, its peak frequency is highly redshifted towards lower frequencies. The observed frequencies evolve as $\nu_{\text{obs}} = \nu_0/(1+z)$, which means the peak frequency in the host galaxy frame would have been between 4.2 and 7.1 GHz for the expected redshift range. As will be further discussed in Section 6.5, and shown in Fig. 29, this is the highest inferred rest frame frequency of a one-off FRB to date. The implications of such a high DM FRB are also reviewed later, in Section 6.1.4.

5.1.8. FRB 20210124A

This burst, with a DM of 869.2 pc cm^{-3} , consists of a scattered single component with $\tau_{\text{sc}} = 0.65$ ms. If we divide the burst into six subbands, we measure a scattering index $\alpha = 4.4 \pm 3.3$, fully consistent with scattering by a turbulent medium or a thin screen. Additionally, the FRB presents intensity modulations with frequency, with a decorrelation bandwidth $\Delta\nu_{\text{sc}} = 1.7$ MHz. These modulations are likely to be a product of scintillation in the MW, since the expected scintillation bandwidth predicted by NE2001 in the direction of the FRB, ~ 1 MHz, agrees with our measurement well within a factor of two. If we consider the screen producing the scattering to be closer to the production site of the burst and the one producing the scintillation to be within the MW, we can set an upper limit on the distance between the FRB and the first screen to be ~ 600 kpc assuming the host galaxy to be at $z = 0.9$. The scattering must thus have been produced within the galactic neighbourhood of the FRB host galaxy.

The Stokes data of this FRB were saved, and we carried out observations of a linearly polarised and an unpolarised calibrator (3C286 and 3C147 respectively). In the Stokes data (See Fig. C.1), we observe signal in Stokes I and Q , but not in U and V . The linear polarisation fraction adds up to $L = 86 \pm 8\%$, the highest in our sample together with FRB 20191108A (Connor et al. 2020, see Section 4.6). The resulting circular polarisation fraction is in turn $V = 15 \pm 12\%$, roughly consistent with 0. The

PPA remains constant within errors throughout the burst duration.

Although the FRB was localised to an error region as small as 0.89 arcmin^2 , we identified 11 galaxies within the error region and redshift upper limit, $z_{\text{max}} = 1.13$. It is thus not possible to identify the most likely host galaxy. The localisation region and host galaxy candidates are displayed in Fig. 16.

5.1.9. FRB 20210127A

This FRB, detected at a DM of 891.7 pc cm^{-3} , consists of a single component, 0.83 ms wide, with no measurable scattering. The burst extends over the whole observing bandwidth, and no scintillation is visible at Apertif frequencies. Its full-Stokes data were saved, and subsequent observations of a linearly polarised and unpolarised calibrators (3C286 and 3C147 respectively) were carried out. The burst was detected in SB 34 while the calibrators were centred in SB 35, and although these SBs are adjacent, the calibrated data still shows a residual V signal with oscillating intensity that is unlikely to arise from a physical phenomenon (See Fig. C.1). Stokes Q and U display similar oscillations, and we thus apply a phase correction to minimise the V signal. After implementing RM synthesis, we obtain an $\text{RM} = 123.5 \pm 0.4 \text{ rad m}^{-2}$, as presented in Fig. C.4. This RM is in excess of what we expect from the MW contribution, $\text{RM}_{\text{MW}} \sim 35 \text{ rad m}^{-2}$ (See Table C.1). If the FRB was produced at $z_{\text{Macquart}} \sim 0.98$, this would translate to $\text{RM}_{\text{host}} \sim 335 \text{ rad m}^{-2}$ in the source reference frame. The PPA shows a marginally significant decrease of about 5 degrees.

We localised this FRB to a small error region of 0.75 arcmin^2 , but we identified eight galaxies with photometric redshifts below the upper limit $z_{\text{max}} = 1.23$, and it is thus not possible to determine the most probable host. See Fig. 16 for the localisation region and candidate hosts.

5.1.10. FRB 20210317A

This burst has a DM of 466.4 pc cm^{-3} and it is formed by a single component. The burst displays frequency modulations with a decorrelation bandwidth of 4.8 MHz without measurable scattering. The NE2001 model predicts the MW scintillation bandwidth in the direction of the FRB to be ~ 1.1 MHz, and since these agree within an order of magnitude, we attribute the burst modulation to scintillation in the MW.

The burst triggered a full-Stokes data dump, but since it was detected during the last observation of the observing run, no calibration observations could be scheduled. The raw Stokes V data show oscillations resembling those produced by Faraday rotation in Q and U , hence we apply the circular polarisation minimisation technique to rotate the phase of the V signal into U . This produces the calibrated data presented in Fig. C.1. After applying RM synthesis, we determine an $\text{RM} = -252.5 \pm 1.3 \text{ rad m}^{-2}$ (See Fig. C.5), and the resulting linear and circular polarisation fractions are $L = 50 \pm 5\%$ and $V = 3 \pm 4\%$. Given the expected contribution $\text{RM}_{\text{MW}} \sim 26 \text{ rad m}^{-2}$, the RM at the expected redshift $z_{\text{Macquart}} = 0.38^{+0.10}_{-0.22}$ would be around $\text{RM}_{\text{host}} \sim -530 \text{ rad m}^{-2}$. The PPA shows a slow increase of ~ 7 degrees throughout the burst duration.

Since we localised the burst to a relatively small error region of 0.54 arcmin^2 centred at the coordinates 19:36:27.4 +59:51:50.7 in RA and DEC, we searched for host galaxy candidates in and around the error region. We identified one galaxy with photometric redshift $z = 0.15 \pm 0.05$ within the error region,

and two additional ones at $z = 0.30 \pm 0.05$ and $z = 0.15 \pm 0.06$ respectively 4.5" and 8.5" away from the error region. Although G1 is the most likely host at 54%, G2 also has a 35% probability of being associated to the FRB. Hence, we cannot confidently identify the host of FRB 20210317A. The localisation region and host galaxy candidates are shown in Fig. 13, while the details of the PATH analysis are shown in Table B.

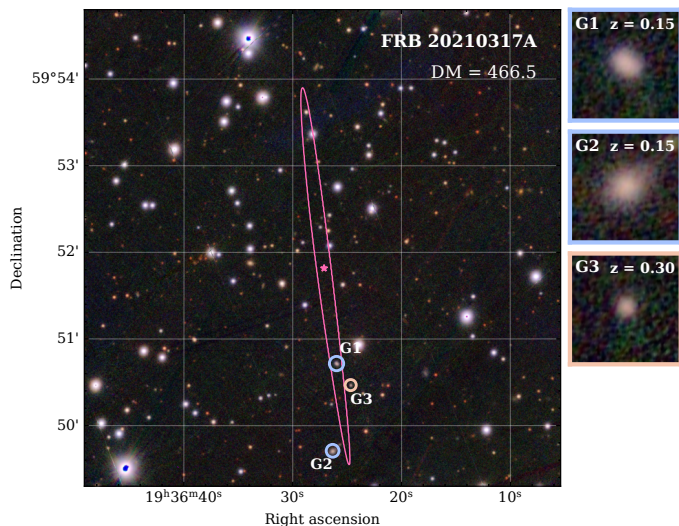


Fig. 13. Localisation region (pink contour) of FRB 20210317A. The three galaxies next to or inside the error region within the redshift limit are indicated by circles and zoomed in on the right.

5.1.11. FRB 20210530A

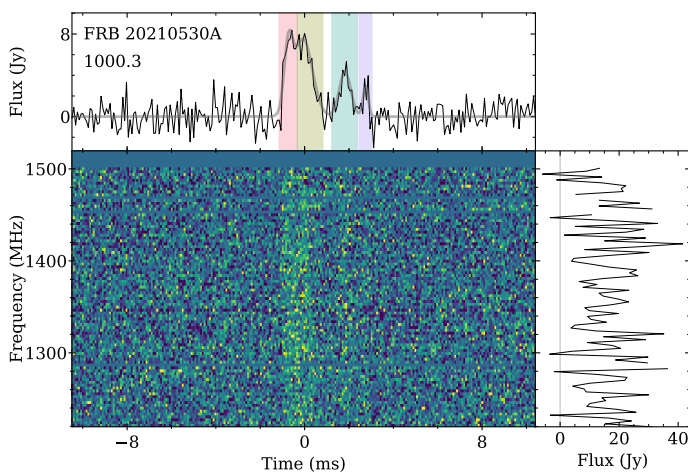


Fig. 14. Dynamic spectrum of FRB 20210530A. The pulse profile is fitted to four Gaussian components, each of them marked by coloured shaded regions. The added spectrum of all four components remains constant throughout the whole bandwidth.

The pulse profile of this FRB consists of a main, broad component with a flat top followed by two postcursors, and it is well fitted by four Gaussian components, as shown in Fig. 14. The first two Gaussians model the profile of the main component, and they have a similar amplitude and a separation of 0.67 ms. The two postcursors have a separation of 1.89 ms and 0.93 ms

with respect to their preceding subcomponents each. A timing analysis does not reveal evidence for periodicity.

The burst triggered a full-Stokes data dump, and calibrators 3C286 and 3C147 were observed. The two main components display an oscillating signal in the calibrated Stokes Q and U, but not in V. After applying RM synthesis, we find an $RM = -125.1 \pm 4.6 \text{ rad m}^{-2}$, as seen in Fig. C.6. The resulting polarisation fractions are $L = 52 \pm 4\%$ and $V = 0 \pm 7\%$. The PPA of the two main components appears first to increase by ~ 20 degrees and then to decrease back to the initial value.

We localised this FRB to an error region of 2.97 arcmin^2 . We find 36 galaxies contained within this region and the Macquart redshift upper limit $z_{\text{max}} = 1.35$, as shown in Fig. 16, too many to identify the most likely host.

5.1.12. FRB 20211024B

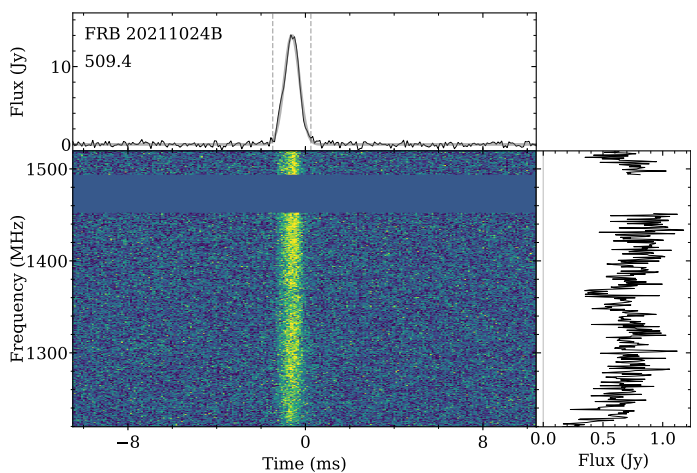


Fig. 15. Dynamic spectrum of FRB 20211024B. The spectrum shows a morphology that cannot be well fitted to a Gaussian nor a power law, but that could be of instrumental origin: the FRB was detected in SB 40 (Table A.2), which is composed of 2 TABs (see Sect. 4.5).

This FRB, displayed in Fig. 15, consists of a single discernible component with a FWTM of 1.45 ms. The burst presents a slight asymmetry, with the intensity increasing more slowly than it decreases at later time. This could be an intrinsic property of the burst, or a hint of an unresolved precursor. The burst was detected with a DM of 509.4 pc cm^{-3} , and after removing the MW and halo contribution, we expect a redshift of $z_{\text{Macquart}} = 0.52^{+0.12}_{-0.30}$.

This FRB has a small localisation region of 0.77 arcmin^2 , and within the redshift upper limit $z_{\text{max}} = 0.64$, we find five host galaxy candidates with photometric redshifts ranging from 0.2 to 0.6. We find the most likely host to be the brightest galaxy, G2, with $P(G_2|x) \sim 61\%$, while for the second brightest galaxy we find $P(G_1|x) \sim 24\%$. These two host candidates have similar photometric redshifts $z_{\text{phot}} \sim 0.24$, on the lower end of what is expected from the Macquart relation for the assumed DM_{host} . The details of the host candidates and PATH analysis are presented in Table B.

5.1.13. Bicomponent bursts

Three bursts manifest two components, where the first is brighter than the second. Two of the FRBs, FRB 20190709A

and FRB 20191109A, were originally presented in van Leeuwen et al. (2023). As discussed there, the subcomponents of FRB 20190709A have a separation of 1.3 ms, and the amplitude of the first is roughly five times larger than the second. Each has a FWTM of ~ 0.9 ms, and no scattering can be resolved. The first component is broadband and shows intensity variations in frequency consistent with the expected scintillation in the MW. The second component is mainly visible at the bottom of the band, coincident in frequency with a bright scintillation ‘patch’ from the first component.

Similarly, the subcomponents of FRB 20191109A have a separation of 1.2 ms, the main component has a width of 0.7 ms and it is ~ 3.5 times larger in amplitude than the second, with a width of 1.4 ms. The pulse profile shows a bump about a millisecond after the first component, but its S/N is too low to confidently associate it with a third component. The two components have a similar frequency extent. The emission extends from the top of the band down to 1280 MHz. There appears to be a gap in emission between 1370 and 1440 MHz, but we associate it to an instrumental effect (lower sensitivity at those frequencies during the observation) rather than to an intrinsic property of the burst.

FRB 20200321A is the last burst with two components. The observation where this burst was detected was highly affected by RFI, and nearly half of the observing bandwidth had to be masked. The subcomponent separation is 0.7 ms, while the widths are 0.9 ms and 1.3 ms for the first and the second subcomponents respectively. The subcomponents are thus nearly merged together. From the limited available bandwidth, the two components appear to be narrowband, with a frequency extent of ~ 230 MHz at a peak frequency 1435 MHz, and both subcomponents extending the same range of frequencies. This FRB triggered the dump of the full-Stokes data, and observations of the linearly polarised calibrator 3C286 were subsequently scheduled. The Stokes Q and U parameters do not display any discernible oscillation where an RM could be estimated, and we measure low polarisation fractions of $L = 17 \pm 5\%$ and $V = 13 \pm 9\%$. The calibrated Stokes parameters are shown in Fig. C.1.

5.1.14. Low polarisation bursts

In this section we include the bursts that triggered the storage of the full-Stokes data which have an average linear polarisation fraction $L < 35\%$ and a circular polarisation fraction $V < 30\%$. Following the FRB polarisation classification from Sherman et al. (2024), these bursts would be considered to be unpolarised. Six out of the 16 bursts with Stokes data fall into this category, including FRB 20200213A presented in Section 5.1.2, and FRB 20200321A described in Section 5.1.13. The calibrated Stokes data of these bursts are displayed in Fig. C.1, and the remaining four bursts are described below.

FRB 20191020B, originally presented in van Leeuwen et al. (2023), was the first FRB of the sample that triggered the storage of the Stokes data. Although no calibrator observations were taken at the time, in the raw data we observe signal in the linear polarisation of $L = 31 \pm 7\%$, and a circular polarisation fraction consistent with 0. There is no sign of Q/U oscillations with frequency that could be attributed to Faraday rotation.

FRB 20200322A, detected at a DM of $1290.3 \text{ pc cm}^{-3}$ presents a scattering tail with $\tau_{\text{sc}} = 4.2$ ms. The burst appears narrowband, with most of the emission observed above 1300 MHz. By dividing the bandwidth into four subbands, we were able to measure the scattering timescale in the three subbands and infer a scattering index $\alpha = -4.5 \pm 2.3$, which is consistent with

both scattering in a turbulent medium or by a thin screen. The spectrum can be fitted to a Gaussian peaking at 1406 MHz, and additionally it shows spectral modulations with a decorrelation bandwidth of 5 ± 2 MHz, consistent with the expected MW contribution. The combination of scattering and scintillation would place an upper limit between the FRB location and the scattering screen of ~ 300 kpc assuming a redshift of $z_{\text{Macquart}} \sim 1.46$. The Stokes data of the FRB were saved upon its detection, and the U/V leakage was calibrated using the linearly polarised source 3C286. The burst appears to be unpolarised, with $L = 3 \pm 6\%$ and $V = 14 \pm 9\%$. The Stokes data are presented in Fig. C.1.

FRB 20200323C was detected at a DM of 833.4 pc cm^{-3} and consists of a single component with a scattering timescale of $\tau_{\text{sc}} = 1.3$ ms. The burst is brighter at the top of the band, and its spectrum can be well fitted by a power law with a spectral index $\Gamma \sim 6.3$. By dividing the dynamic spectrum into 8 subbands, we measured the scattering timescale in the top 6, where the burst is bright enough, resulting in a scattering index of $\alpha = -3.5 \pm 3.0$. Its detection triggered a full-Stokes data dump, and 3C286 observations were obtained to calibrate the U/V leakage. The burst presents a polarisation fraction consistent with 0, although some residual Q/U signal is apparent in Fig. C.1. The signal is however not strong enough to apply the RM synthesis technique.

FRB 20200516A, with a DM of 361.1 pc cm^{-3} , is a single component burst with a temporal width of ~ 2.2 ms and no measurable scattering, whose spectrum can be well fitted by a power law with a spectral index $\Gamma \sim +7.9$. Unfortunately, no calibration observations were performed after the detection of this burst. The raw data shows however a low polarisation fraction of $L = 17 \pm 13\%$ and $V = 14 \pm 7\%$. Calibration would have been unlikely to significantly modify this result.

5.2. Localisation

The Apertif localised FRBs have an average error region of $\sim 5 \text{ arcmin}^2$ and a median of $\sim 2 \text{ arcmin}^2$. Figure 16 displays the 99% confidence levels on the localisation of the new Apertif FRBs with a localisation area $< 6 \text{ arcmin}^2$, as well as the galaxies identified within the error regions. Depending on the mean redshift from the Macquart relation, we estimate the number of dwarf and massive galaxies expected to be contained in the comoving volume V_{co} of the localisation region, as shown in Fig. 17. For FRB 20200210A, we assume the redshift obtained by combining scattering timescale and DM (See Section 5.1.1). For the FRBs published in van Leeuwen et al. (2023), we provide updated error regions after fitting them to an ellipse at the 99% level.

For several of the Apertif FRBs, the expected number of dwarf galaxies within the error region computed as described in Section 4.3 is < 5 , while the number of expected massive galaxies is $\ll 1$, namely FRB 20200210A, FRB 20200419A, FRB 20200518A, FRB 20210317A, FRB and 2021020A. After searching for known galaxies within the expected redshift limits for the relatively well localised FRBs, we find seven FRBs with ≤ 5 host galaxy candidates, listed in Table B. For FRB 20200419A, we find a single host galaxy candidate with a PATH association probability of $\sim 70\%$, while FRB 20200210A, FRB 20200518A, FRB 20210317A, and FRB 20211024B have host galaxy candidates with association probabilities between 50% and 60%.

For searches of associated radio continuum emission at 1.4 GHz, only FRB 20190709A, FRB 20190926B and FRB 20191108A (van Leeuwen et al. 2023) lie within the Apertif imaging footprint (Adams et al. 2022). For the latter FRB,

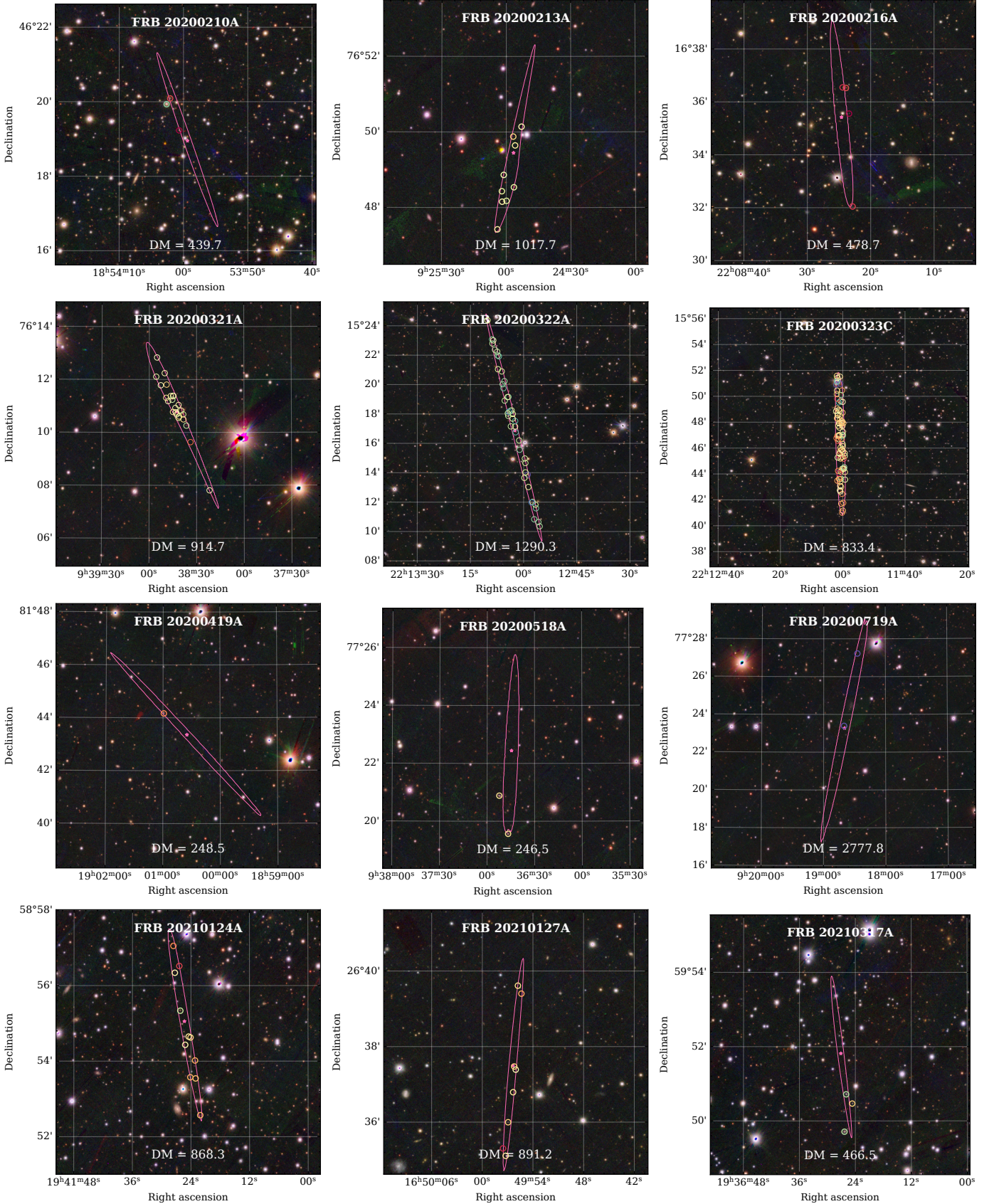


Fig. 16. Localisation regions of the new Apertif FRBs with an error region $<6 \text{ arcmin}^2$. In each subplot, the pink contour represents the 99% confidence region of the localisation, and the pink star the centroid of the error region. The circles show the PS1-STRM galaxies identified within or close to the error region and redshift range of each FRB, with colours from blue to red as redshift increases. The text on top of each plot gives the TNS identifier of each FRB, and the bottom text the DM in units of pc cm^{-3} . The background images are from the PanSTARRS DR1 (Chambers et al. 2019). In each plot, the grids are spaced by 2 arcmin in declination.

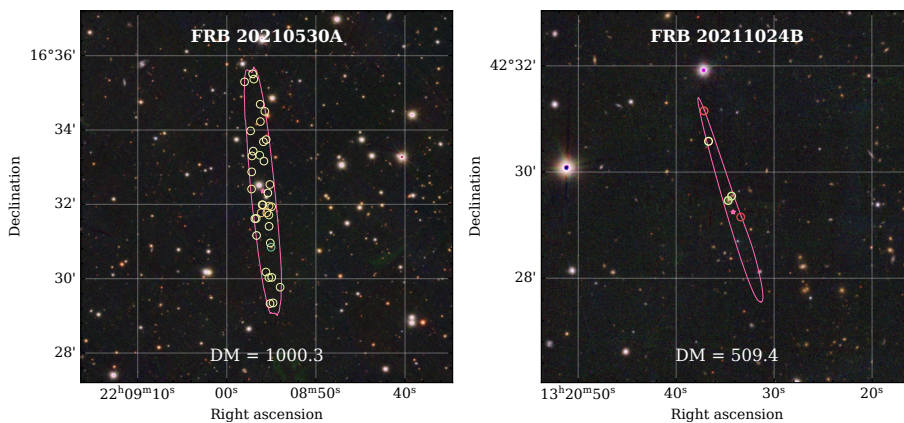


Fig. 16. Continued

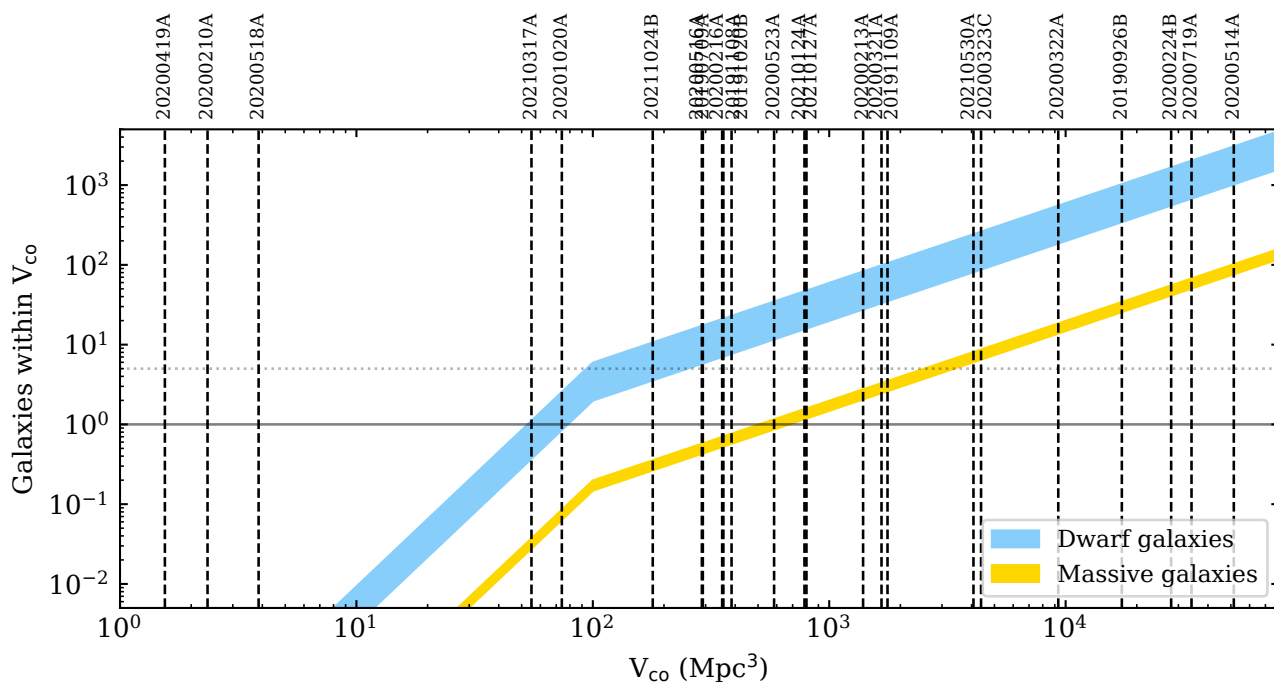


Fig. 17. Expected galaxies within the comoving volume of the FRB localisation. The blue and yellow shaded regions give the expected number of dwarf and massive galaxies respectively within the localisation region and redshift upper limits. Each vertical dashed line gives the upper limit on the comoving volume of an FRB, whose TNS identifiers are given on top. The horizontal solid line shows the one galaxy limit, while the dotted line shows the five galaxy limit.

the lowest-redshift one of the set, Connor et al. (2020) report an imaging non-detection.

All FRBs were found with Galactic latitudes $|l| > 12^\circ$ with the exception of FRB 20200514, with $l = 2.48^\circ$, which was detected in an observation of the repeater FRB 20180916B.

The localisation regions of all Apertif FRBs are reported in Table A.2. The regions were fitted to a 2D Gaussian and we provide the ellipse properties that best match the 99% error region of each FRB, with RA and DEC indicating the ellipse centre, a and b the semi-major and semi-minor axes respectively, and θ the angle of the ellipse measured from West (lower RA) through North, following the SAOImageDS9¹⁶ convention.

5.3. Event rate and fluence distribution

Within the Apertif FRB survey, we have discovered 24 new one-off FRBs in 5259 h of observing time. This corresponds to an average of one FRB every 9.1 days. Following van Leeuwen et al. (2023), we assume an effective Apertif FoV of 8.2 deg^2 , which already accounts for the sensitivity of the CBs. The all-sky rate for N detected FRBs is expressed as follows:

$$R (\text{sky}^{-1} \text{day}^{-1}) = N \times \frac{24 \text{ h day}^{-1} \times 41253 \text{ deg}^2 \text{sky}^{-1}}{5259 \text{ h} \times 8.2 \text{ deg}^2} \quad (15)$$

With $N = 24$ FRBs, this yields an Apertif all-sky FRB rate of $550_{-170}^{+220} \text{ sky}^{-1} \text{day}^{-1}$, with 90% Poisson errors (Gehrels 1986). The rate is consistent with our estimate from van Leeuwen et al. (2023), based on the first 5 Apertif FRB detections, of $700_{-400}^{+800} \text{ sky}^{-1} \text{day}^{-1}$.

¹⁶ ds9: <https://sites.google.com/cfa.harvard.edu/saoimages9>

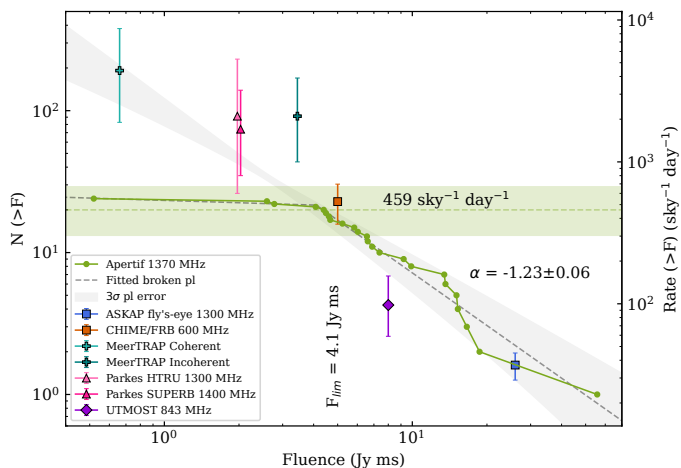


Fig. 18. Cumulative fluence distribution of the Apertif FRBs. The left y axis gives the number of FRBs, and the right y axis its conversion to an all sky rate using Eq. 15. The green dots give the measured FRB fluences, and the grey dashed line their fit to a broken power law. The diagonal grey shaded region gives the 3σ confidence interval of the power law above the fluence limit extrapolated to other fluences. The vertical grey shaded region is below the fluence completeness threshold of 4.1 Jy ms, while the horizontal green shaded region gives the all-sky FRB rate above that fluence, with Poissonian 95% confidence limits. The power law above the completeness threshold has an index of $\gamma = -1.23$. The markers give the all-sky rates estimated by other surveys; blue square for ASKAP fly’s-eye (Shannon et al. 2018), orange square for CHIME/FRB (CHIME/FRB Collaboration et al. 2021), turquoise cross for MeerTRAP Coherent, and teal cross for MeerTRAP Incoherent (Jankowski et al. 2023) light pink triangle for Parkes HTRU (Champion et al. 2016), dark pink triangle for Parkes SUPERB (Bhandari et al. 2018), and purple diamond for UTMOST (Farah et al. 2019).

Burst rates are only meaningful when given together with the fluence completeness threshold of the instrument, which can be highly variable. In van Leeuwen et al. (2023), we determined this threshold from the typical SEFD of the system. Here we take a complementary approach; we build a cumulative fluence distribution of the Apertif FRBs (See Fig. 18), and fit it to a broken power law, assuming the break in the power law corresponds to the fluence completeness threshold;

$$N(> F) = \begin{cases} C(F/F_{lim})^{\gamma_0}, & \text{if } F < F_b \\ C(F/F_{lim})^{\gamma}, & \text{otherwise,} \end{cases} \quad (16)$$

where C is a constant, F_{lim} is the fluence completeness threshold, and γ_0 and γ are respectively the power law indices below and above the completeness threshold. This way, we recompute the all-sky rate for the FRBs above the completeness threshold and determine the power-law index of the fluence distribution. We find a fluence completeness threshold of $F_{lim} = 4.1 \pm 0.2$ Jy ms, with $N = 20$ FRBs above the threshold. Using Eq. 15, this yields an FRB all-sky rate at 1370 MHz of $R_{1370}(F \geq 4.1 \text{ Jy ms}) = 459^{+208}_{-155} \text{ sky}^{-1} \text{ day}^{-1}$, with 90% Poisson errors. Furthermore, we determine a fluence distribution power law index of $\gamma = -1.23 \pm 0.06$, where we quote the 1σ statistical error from the fit. We estimate a systematic error of 0.2 on γ .

We use the resulting power law to compare our subsequent all-sky rate to the estimates made by other surveys at their respective fluence completeness thresholds. In Fig. 18 we plot the all-sky rates from the ASKAP fly’s-eye search ($F > 26$ Jy ms; Shannon et al. 2018), the Parkes HTRU ($F > 2$ Jy ms; Champion et al. 2016) and SUPERB ($F > 2$ Jy ms; Bhandari et al.

2018) surveys, the UTMOST survey ($F > 8$ Jy ms; Farah et al. 2019), MeerTRAP coherent and incoherent ($F > 0.66$ Jy ms and $F > 3.44$ Jy ms, respectively; Jankowski et al. 2023), and the First CHIME/FRB Catalog ($F > 5$ Jy ms; CHIME/FRB Collaboration et al. 2021). The comparison between the Apertif FRB all-sky rate and other surveys will be discussed in Section 6.4.

5.4. Propagation effects

The Apertif FRB sample displays a large variety of propagation effects. In this section we describe the observed dispersion measures, scattering timescales and scintillation bandwidths, and compare them to the FRB samples collected by other instruments and to the expected Milky Way contribution (queried from NE2001 and YMW16 at 1370 MHz using pygedm; Price et al. 2021).

5.4.1. Dispersion measure

The FRB sample presented here has observed DMs ranging from 246 pc cm^{-3} to 2778 pc cm^{-3} , with an average of $\sim 800 \text{ pc cm}^{-3}$ and a median of $\sim 625 \text{ pc cm}^{-3}$. The expected MW and halo contribution in our FRB sample varies between 70 pc cm^{-3} and 300 pc cm^{-3} . We compare the Apertif DMs to other instruments with burst samples larger than 10, listed in the Transient Name Server (TNS) database¹⁷; here we select the FRBs reported by CHIME/FRB (CHIME/FRB Collaboration et al. 2021), ASKAP (Bannister et al. 2017; Shannon et al. 2018; Macquart et al. 2020), Parkes (Lorimer et al. 2007; Keane et al. 2012, 2016; Thornton et al. 2013; Burke-Spolaor & Bannister 2014; Petroff et al. 2015, 2017; Ravi et al. 2015, 2016; Champion et al. 2016), UTMOST (Caleb et al. 2017; Farah et al. 2018, 2019), DSA-110 (Law et al. 2024), and MeerTRAP (Jankowski et al. 2023).

The top panels of Fig. 19 show histograms of the observed and excess DMs of the Apertif FRBs compared to the First CHIME/FRB Catalog, and to all other FRBs contained in the TNS database. The cumulative distributions of the observed (DM_{obs}) and excess ($DM - DM_{MW}$) dispersion measures of Apertif, CHIME/FRB, ASKAP, Parkes and UTMOST are also shown in the lower panels. Table 1 gives the median of the observed and extragalactic DMs for each of the aforementioned surveys. To know whether the Apertif DMs could be drawn from the same distribution as any of the other surveys, we perform a Kolmogorov-Smirnov two sample test and obtain the p-value p_{KS} . If $p_{KS} < 0.01$, we cannot reject the hypothesis that the DMs of the two surveys being compared have been drawn from different distributions.

We find the Apertif DM distribution to be compatible with most surveys, mainly Parkes, UTMOST, MeerTRAP, and CHIME/FRB, given the obtained p-values. The median observed and extragalactic DMs are comparable, with Parkes having the highest median DM and CHIME/FRB DMs being slightly lower than Apertif. ASKAP, however, has the lowest median DM of all surveys, and a $p_{KS} < 0.01$ on both the observed and extragalactic DMs when compared to Apertif, and DSA-110 is ambiguous, with $p_{KS} = 0.061$. The difference in DMs is also discernible in the cumulative distribution of Fig. 19. This indicates Apertif is sensitive to a more dispersed, and thus more distant population of FRBs than ASKAP and DSA-110.

¹⁷ TNS database: www.wis-tns.org

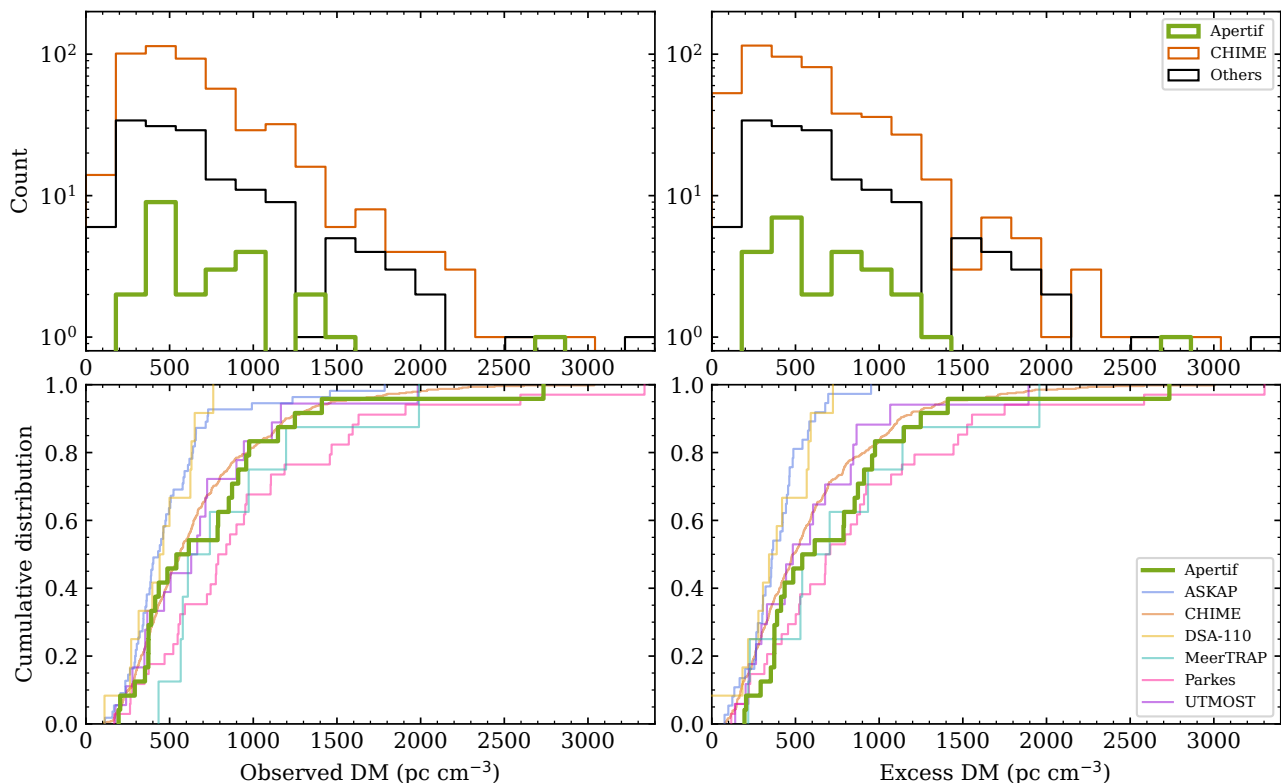


Fig. 19. Distribution of Apertif FRB DMs compared to other FRB samples. The top left and right panels show respectively histograms of the observed and excess DMs with respect to the Milky Way contribution, with Apertif in green, CHIME/FRB in orange, and all other FRBs in the TNS in black. The bottom left and right panels show respectively the cumulative distribution of observed and excess DMs of different single instrument FRB samples, with Apertif in green, ASKAP in blue, CHIME/FRB in orange, DSA-110 in yellow, MeerTRAP in turquoise, Parkes in pink, and UTMOST in purple.

Table 1. Comparison of Apertif DMs to other instrument samples.

Instrument	Observed DMs		Extragalactic DMs	
	Median	p_{KS}	Median	p_{KS}
Apertif	625		578	
ASKAP	431	0.009	361	0.005
CHIME	562	0.269	485	0.194
DSA-110	452	0.061	365	0.061
MeerTRAP	675	0.482	622	0.945
Parkes	815	0.415	694	0.774
UTMOST	647	0.701	484	0.592

Notes. Observed and extragalactic DM medians of Apertif, ASKAP, CHIME/FRB, DSA-110, MeerTRAP, Parkes, and UTMOST FRB samples, and KS two-sample p-value (p_{KS}) of Apertif against all other samples.

5.4.2. Scattering

Out of the 24 detected FRBs, seven have measurable scattering, with values ranging between 0.6 ms and 21 ms at the central frequency of 1370 MHz. A histogram of the measured values is shown in green on the left panel of Fig. 20. The measured scattering timescales are two to four orders of magnitude higher than what we expect from the Milky Way (MW) contribution according to the NE2001 (Cordes & Lazio 2003) and the YMW16 (Yao et al. 2017) models, as shown in Fig. 21. The scattering is thus likely produced in the host galaxy or the local environment of the FRB, or alternatively in an intervening galaxy in the propagation path of the burst.

For a radio wave propagating through a thin scattering screen, the scattering timescale evolves with frequency as $\tau_{sc} \propto \nu^{-4}$ (Lorimer & Kramer 2004). Due to detection biases quantified with an injection pipeline (CHIME/FRB Collaboration et al. 2021), the CHIME/FRB population of FRBs with $\tau_{sc} > 10$ ms at 600 MHz is incomplete, which corresponds to about >0.37 ms at 1370 MHz. The most scattered FRBs detected by CHIME/FRB thus slightly overlap with the low end of the Apertif sensitivity to scattering. This reveals that Apertif can detect a population of highly scattered bursts which are unlikely to be detected by CHIME/FRB due to the scattering reduced S/N at those lower frequencies. On the other hand, Apertif cannot resolve scattering timescales below the instrumental broadening, which are more likely to be resolved by CHIME/FRB.

In order to roughly estimate how the scattered Apertif bursts modify the intrinsic FRB scattering distribution, we build a joint scattering distribution. To do so, we add the Apertif scattering histogram normalised by the number of Apertif bursts to the CHIME/FRB fiducial scattering model (CHIME/FRB Collaboration et al. 2021), and next we fit it by a lognormal model. This method is justified by the small overlap between the different surveys sensitivities to scattering, and it effectively skews the distribution towards higher scattering values. The equation for the lognormal distribution with the x axis in logarithmic scale is given by:

$$p(x) = \frac{m}{\sigma \sqrt{2\pi}} \exp\left(-\frac{\ln(x/m)^2}{2\sigma^2}\right), \quad (17)$$

where the shape σ is a frequency-independent value and m is the frequency-dependent scale in ms. For the joint distribution, we

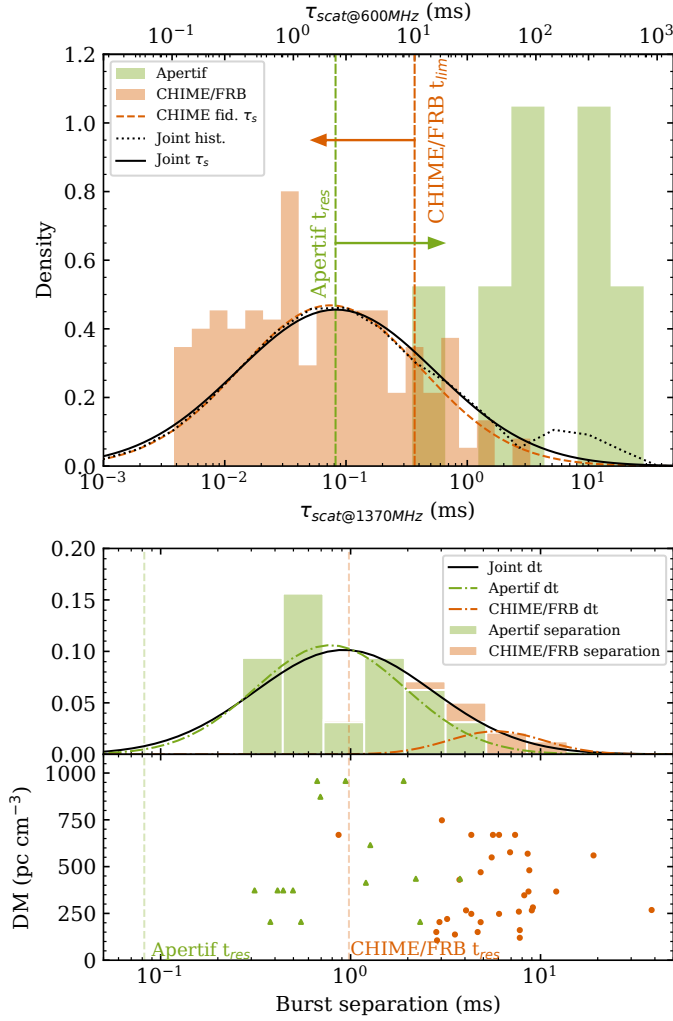


Fig. 20. Scattering and subcomponent separation distributions of Apertif and CHIME/FRB. **Top:** Histogram of observed scattering timescales in CHIME/FRB and Apertif FRBs. The dashed orange line represents the fiducial scattering timescale distribution of CHIME/FRB bursts. The dotted black line shows the joint scattering timescale distribution of Apertif and CHIME/FRB, and the solid black line its fit to a lognormal distribution. The dashed green and orange lines and arrows indicate respectively where Apertif and CHIME/FRB are sensitive to scattering. The lower horizontal axis shows the scattering timescales scaled to the centre of the Apertif band, 1370 MHz, while the upper horizontal axis is scaled to 600 MHz, the centre of the CHIME/FRB band. **Bottom:** Joint stacked histogram of observed subcomponent separations. The green histogram represents the Apertif separation distribution normalised by the total number of components in the FRB sample. The orange histogram is the same for CHIME/FRB. The black line shows a fit of the joint histogram to a lognormal distribution.

find $\sigma = 1.86 \pm 0.07$ and $m = 0.081 \pm 0.006$ ms at 1370 MHz or $m = 2.2 \pm 0.2$ ms at 600 MHz (same σ). This resulting distribution is a rough estimate; correcting for the detailed observational biases and determining the intrinsic FRB scattering distribution is out of the scope of this paper.

5.4.3. Scintillation

Scintillation is measurable in 11 out of the 24 FRBs, with $\Delta\nu_{sc}$ values ranging from 0.8 to 9.3 MHz. In most cases, the observed scintillation bandwidths are larger than the expected Milky Way

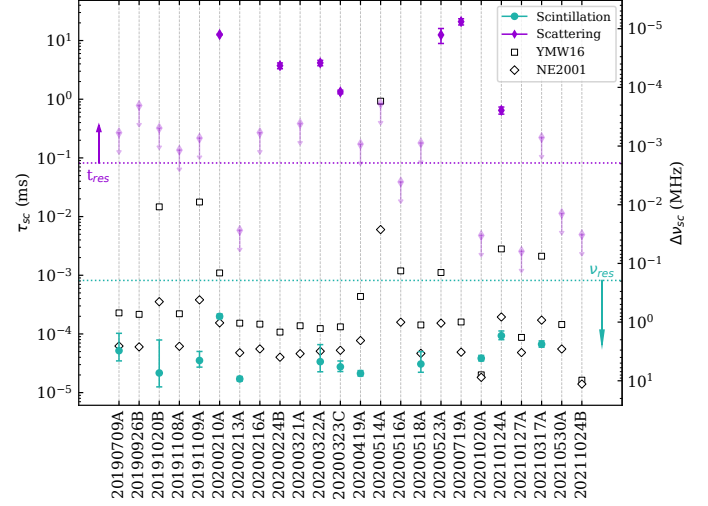


Fig. 21. Scattering timescales and scintillation bandwidth of Apertif FRBs. Each vertical line corresponds to a different FRB, arranged by detection date. The left axis gives the scattering timescale and the right axis the corresponding scintillation bandwidth at 1370 MHz, using the conversion given by Eq. 13. Purple diamonds with error bars give the measurable scattering timescales, and purple diamonds with arrows the scattering timescale upper limits. Cyan circles with error bars give the measured scintillation bandwidth when measurable. The white squares and diamonds give respectively the expected Milky Way contribution to scattering from the YMW16 and NE2001 models at 1370 MHz. The horizontal dotted purple and cyan lines show respectively the Apertif time and frequency resolution.

contribution at 1370 MHz predicted by the YMW16 (Yao et al. 2017) and NE2001 (Cordes & Lazio 2003) models, but they still fall within the 40% error assumed for these models. Figure 21 shows the measured scintillation bandwidths and their comparison to the expected Milky Way contribution. The scintillation bandwidth is converted to scattering timescales using Eq. 13. These results will be further discussed in Section 6.1.5.

5.5. Polarisation

Of the 24 FRBs detected during the Apertif survey, 16 triggered a dump of the full Stokes parameters, and they are all presented in Fig. C.1. Of those, eight present measurable RMs, ranging from ~ 120 rad m^{-2} to ~ 2050 rad m^{-2} in absolute value (see Table C.1). The sample includes the one-off FRB with the second largest $|\text{RM}|$ ever reported (after FRB 20221101A from Sherman et al. 2024); FRB 20200216A, with $\text{RM} = -2051.0 \pm 5.8$ (See Fig. 8). When converting the RM to the expected redshift range, $z_{\text{Macquart}} = 0.44^{+0.12}_{-0.24}$, and after removing the expected mw contribution, this becomes $\text{RM}_{\text{host}} = -4200^{+1300}_{-800}$ rad m^{-2} . FRB 20200514A, with an RM of 979.8 ± 20.5 rad m^{-2} , has the second largest $|\text{RM}|$ in our sample, but it is expected to have the largest RM in the reference frame at $z_{\text{Macquart}} = 1.35^{+0.30}_{-0.66}$; $\text{RM}_{\text{host}} = 6500^{+2000}_{-3200}$ rad m^{-2} .

The bursts have an average linear polarisation fraction $L/I = 43 \pm 28\%$, while the average circular polarisation fraction is $V/I = 9 \pm 8\%$, with the errors giving the standard deviation. Two FRBs have linear polarisation fractions $> 80\%$; these are FRB 20191108A (Connor et al. 2020) and FRB 20210124A. While the first one has a large RM value of ~ 473 rad m^{-2} , the latter has no measurable RM within the observing bandwidth.

The two FRBs with the lowest linear polarisation fractions are also the two most scattered bursts with full Stokes data, namely FRB 20200322A with $\tau_{\text{sc}} = 4.2 \pm 0.4$ ms and $L/I = 3 \pm 6\%$, and FRB 20200323C with $\tau_{\text{sc}} = 1.3 \pm 0.1$ ms and $L/I = 6 \pm 3\%$. This could be explained, for instance, by the propagation through a magnetised inhomogeneous plasma screen (see the discussion in Section 6.3). None of the bursts have a significant circular polarisation fraction, with the highest fractions being $V/I = 21 \pm 9\%$ for FRB 20200514A, and $29 \pm 17\%$ for FRB 20200518A. We note, however, that we have calibrated some of the bursts by assuming their circular polarisation fraction to be zero in cases where we saw oscillations in the sign of the V intensity, which could bias our results.

The PPAs of the bursts with sufficient L signal primarily appear to be flat, and in the case of FRB 20200518A even within the two subcomponent groups. In some of the bursts, one or two of the time samples seem to jump up and down in PPA, although this could be produced by noise; see FRB 20200419A, FRB 20200514A, and FRB 20210530A. FRB 20200216A presents a pronounced decrease in PPA of $\sim 20^\circ$, while the PPA of FRB 20210127A appears to decrease by $\sim 5^\circ$ and that of FRB 20210317A increases by $\sim 6^\circ$. FRB 20200213A shows an erratic PPA behaviour, which might be explained by the low linear polarisation fraction.

5.6. Multi-component bursts

Seven out of the 24 detected bursts display more than one discernible component. Our system thus finds $\sim 30\%$ of the bursts at 1370 MHz are multi-component. Of those, three can be well fitted by two components (FRB 20190709A, FRB 20191109A, and FRB 20200321A, see Section 5.1.13); FRB 20200216A is the only one displaying three distinct components; FRB 20200518A and FRB 20210530A are well fitted by four components, and finally FRB 2021020A has five distinct components (Pastor-Marazuela et al. 2023).

In the morphology study of the First CHIME/FRB Catalog bursts, Pleunis et al. (2021a) find that only about 5% of one-off bursts contain multiple components. However, CHIME/FRB Collaboration et al. (2023b) recently published the baseband data for 140 of the bursts from their first catalog, including both one-offs and repeaters. Although no updates on the morphological fractions have been reported yet, by visually examining the published dynamic spectra we determined that $\sim 37 \pm 3$ of the bursts from the 130 one-off FRBs in the sample show complex, multi-component morphologies. This would imply a $\sim 28\%$ fraction of multi-component FRBs, in agreement with the Apertif multi-component fraction.

We can nevertheless compare the reported multi-component bursts from the First CHIME/FRB Catalogue to the Apertif bursts. While the CHIME/FRB mean subcomponent separation is ~ 7.3 ms, with Apertif we observe a mean separation between burst subcomponents of 1.2 ms. This difference can be explained by the time resolution used in the FRB searches for the First CHIME/FRB Catalog of 0.983 ms (CHIME/FRB Collaboration et al. 2021). In order to better assess the observed subcomponent separation distribution for one-off FRBs, we built histograms of the subcomponent separations and fitted them to a lognormal distribution, as given by Equation 17. When estimating the separation distribution parameters from the Apertif bursts only, we find a scale parameter $m = 0.8 \pm 0.2$ ms and a shape parameter $\sigma = 0.9 \pm 0.2$, while for CHIME/FRB we find $m = 5.8 \pm 0.2$ ms and $\sigma = 0.57 \pm 0.03$. To obtain the joint distribution, we normalise each of the instruments histograms; we divide

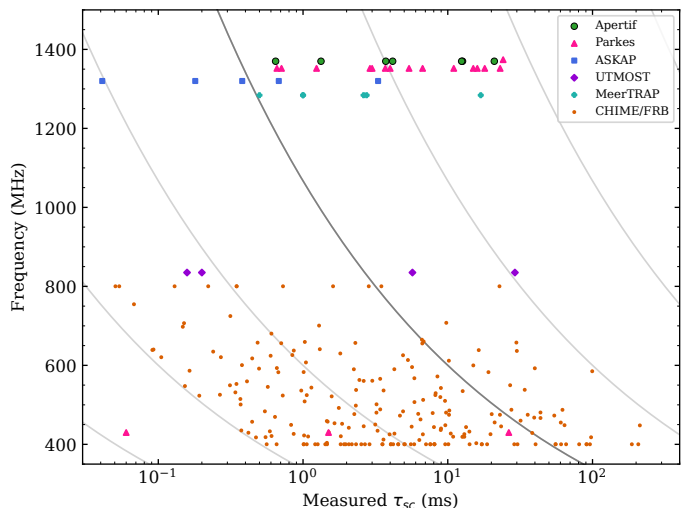


Fig. 22. Observed scattering timescales from different instruments at different frequencies. Green circles represent Apertif (this work), pink triangles Parkes, blue squares ASKAP, purple diamonds UTMOST, turquoise crosses MeerTRAP, and orange circles CHIME/FRB. The values are queried from the TNS database and the First CHIME/FRB Catalog. Grey lines are a reference for the $\tau_{\text{sc}} \propto \nu^{-4}$ relation. The darkest grey line corresponds to the CHIME/FRB scattering sensitivity limit of 10 ms at 600 MHz. Apertif, Parkes, ASKAP, UTMOST and MeerTRAP τ_{sc} are shown at their respective central observing frequencies, while the CHIME/FRB τ_{sc} are shown at the peak frequency of the burst.

the Apertif histogram by the total number of subcomponents in the Apertif sample (39 subcomponents), and we do the same for the CHIME/FRB sample (506 subcomponents). We add the two normalised histograms and fit them to a lognormal distribution, where we find the parameters $m = 0.9 \pm 0.2$ ms and $\sigma = 1.1 \pm 0.3$, as shown in the lower panel of Fig. 20.

5.7. Spectral properties

About two thirds of the Apertif FRBs are broadband, i.e. they have emission from the bottom to the top of the observing bandwidth at roughly the same intensity. The spectra of the remaining bursts can be classified in two different categories. Four have emission at the top of the band, and can be well fitted by a power law with a positive spectral index Γ , ranging from 5.4 to 11.6. The remaining five are narrowband and their spectra can be well fitted by a Gaussian. Although the broadband bursts are likely to have, in reality, a Gaussian or power law spectrum, the fractional bandwidth of Apertif of ~ 0.2 and the presence of structure in frequency from scintillation impede a further characterisation of the wider spectral properties. The burst spectral properties are detailed in Table A.2.

6. Discussion

6.1. Propagation effects

6.1.1. Scattering compared to other surveys

Scattering timescales are a frequency dependent quantity, $\tau_{\text{sc}} \propto \nu^{-\alpha}$ with α the scattering index. The choice of α is important when comparing FRB surveys observing at different frequencies. The theoretical values of the scattering index are $\alpha = 4$ for a simple thin screen model and $\alpha = 4.4$ for a propagation of

the radio waves through a turbulent medium. Estimates of FRB scattering indices are still scarce, and although they are closer to $\alpha = 4$ on average, they are compatible with $\alpha = 4.4$ (e.g. Thornton et al. 2013; Burke-Spolaor & Bannister 2014; Ravi et al. 2015; Masui et al. 2015; Day et al. 2020; Qiu et al. 2020). For Galactic pulsars, Bhat et al. (2004) determine an average scattering index $\alpha \sim 3.86$. In this work, we assume a scattering index $\alpha = 4$, compatible both with Galactic pulsars and FRB observations. This allows us to compare the scattering timescales reported by several surveys observing at different frequencies.

The CHIME/FRB scattering distribution is the most extensive to date, but it is incomplete above $\tau_{\text{sc}} > 10$ ms at 600 MHz (CHIME/FRB Collaboration et al. 2021). This corresponds to about 0.37 ms at 1370 MHz. There is thus a slight overlap between the high end of CHIME and the low end of the Apertif scattering distributions. This means the Apertif FRBs represent a population of highly scattered bursts. Even though we have not performed a burst injection procedure to estimate our biases against detecting FRBs with different properties, the large fraction ($\sim 29\%$) of Apertif FRBs with measurable scattering demonstrate the existence of a large fraction of highly scattered FRBs in the population.

This highly scattered population is further supported by the results of other surveys above 1 GHz. This can be visualised in Fig. 22, where the scattering timescales measured at different frequencies by different surveys are shown. Amongst the ASKAP bursts with measurable scattering (Day et al. 2020; Qiu et al. 2020), more than half have scattering timescales above the CHIME/FRB sensitivity limit, accounting for the frequency difference. Storing data in high time and spectral resolution mode has enabled ASKAP to measure the exponential decay of two FRBs with a lower scattering timescale than any of the Apertif FRBs, down to $\tau_{\text{sc}} = 0.041$ ms for FRB 20190102C. The most scattered ASKAP FRB is FRB 20180130A with $\tau_{\text{sc}} = 5.95$ ms, well below the most scattered Apertif FRB (See Section 5.1.7). Generally, the ASKAP FRBs are less scattered, with an average $\tau_{\text{sc}} \sim 2$ ms compared to the Apertif average of $\tau_{\text{sc}} \sim 6$ ms.

The Parkes FRBs with measurable scattering all fall above the CHIME/FRB sensitivity limit (Lorimer et al. 2007; Ravi et al. 2015; Petroff et al. 2015; Champion et al. 2016; Bhandari et al. 2018; Osłowski et al. 2019; Price et al. 2019). Compared to Apertif, the Parkes FRBs show a marginally larger scattering, with an average $\tau_{\text{sc}} \sim 9$ ms.

Although UTMOST observes at 843 MHz, which is a considerably lower frequency than Apertif, the measured scattering timescales in four FRBs do not significantly differ from Apertif and Parkes (Farah et al. 2019). This could potentially be explained by the high time resolution of $\sim 10 \mu\text{s}$, but it is remarkable to note the similarities between UTMOST, Parkes and Apertif both in the measured dispersion measures and scattering timescales. When accounting for the frequency difference, though, the UTMOST FRBs probe a sample of less scattered bursts than Apertif and Parkes, but similar to ASKAP.

6.1.2. Correlation between dispersion and scattering

Since Galactic pulsars show a correlation between their DMs and scattering timescales, we investigated the presence of such a correlation in the Apertif FRBs. Figure 23 shows the scattering timescales of the FRBs, including upper limits, as a function of excess DM, since we expect the origin of scattering to be extragalactic. The measured DMs and scattering timescales of Galactic pulsars are further plotted for comparison, as well as the τ_{sc} -DM relations established by Cordes & Chatterjee (2019)

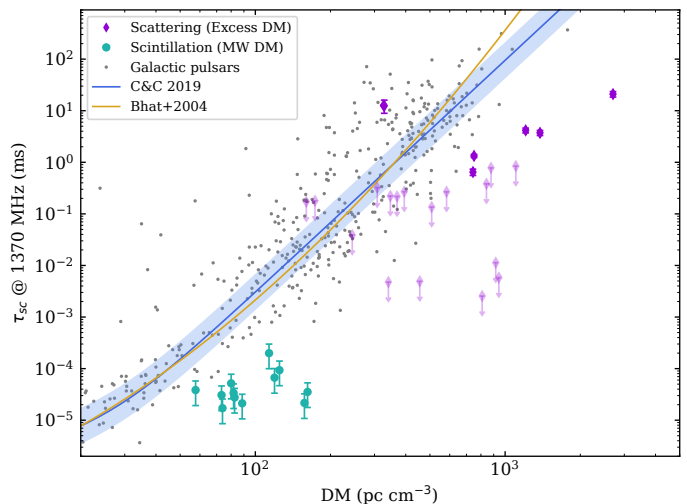


Fig. 23. Scattering as a function of DM of Apertif FRBs compared to Galactic pulsars. The measured Apertif τ_{sc} as a function of extragalactic DM is shown as purple diamonds (higher transparency for upper limits). The cyan circles correspond to the measured scintillation converted to scattering as a function of the expected Galactic DM. The grey dots are the known pulsar τ_{sc} at 1370 MHz as a function of measured DM. The blue line with shaded region is the τ_{sc} -DM relation from Cordes & Chatterjee (2019), and the yellow line the τ_{sc} -DM relation from Bhat et al. (2004).

and Bhat et al. (2004). We also plot the scintillation bandwidth of the FRBs converted to scattering timescales as a function of the expected DM_{MW} , since the measured scintillation bandwidths match the expected Galactic contribution. By eye, the scattering timescales of the FRBs, in the top-right of the Figure, seem to increase with DM, and thus we carried out further correlation analyses.

In order to determine the correlation coefficient between the excess DM and the τ_{sc} values and upper limits of the Apertif FRBs (the purple diamonds in Fig. 23), we compute the Kendall τ correlation coefficient using the `cenken` function of the CRAN NADA package¹⁸, following Feigelson & Babu (2012, Chapter 10.8.3 and references therein). The Kendall τ correlation coefficient is a non-parametric correlation test and it is robust on small sample sizes with censored data (Helsel 2004; Oakes 1982), and it is thus applicable to our case. This function also computes a p-value whose null hypothesis is the absence of correlation. We find a weak correlation coefficient of $\tau = 0.17$, and a p-value = 0.24 above the conventional 0.01, which indicates there is no evidence for a correlation between the excess DM and τ_{sc} of Apertif FRBs.

The lack of evidence for correlation is in agreement with previous FRB observations (Qiu et al. 2020; Petroff et al. 2019; Cordes & Chatterjee 2019). This further supports earlier claims that the IGM does not significantly contribute to scattering (Cordes et al. 2016; Xu & Zhang 2016; Zhu & Feng 2021).

6.1.3. Origin of scattering

Although only FRBs presenting both scattering and scintillation allow us to set upper limits on the distance between the source and the scattering screen, we can determine that the scattering of

¹⁸ CRAN NADA package: <https://cran.r-project.org/web/packages/NADA/index.html>

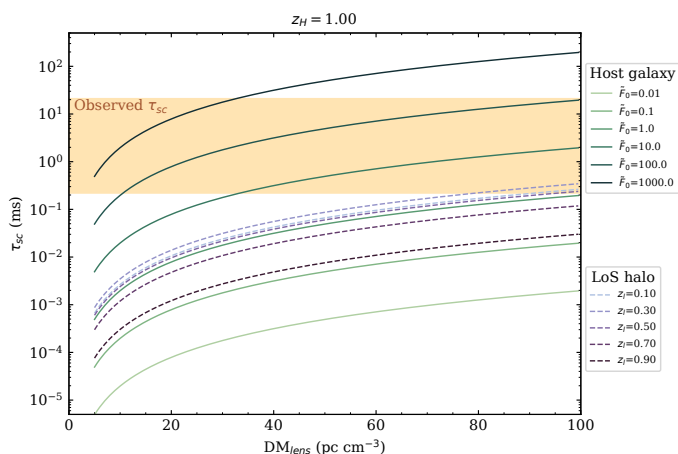


Fig. 24. Expected contribution to scattering at 1370 MHz for different lens DMs from an FRB host galaxy at $z_H = 1$ and an intervening galaxy halo within the line of sight. The solid lines show the expected host galaxy contribution for different electron density variations and a geometric boost factor $G_{sc} = 1$. The dashed lines show the expected contribution from an intervening galaxy halo with a thickness $L = 30$ kpc and $\tilde{F}_0 = 10^{-4} \text{pc}^{-2/3} \text{km}^{-1/3}$ located at different redshifts. The orange shaded region represents the observed Apertif τ_{sc} range.

Apertif FRBs, when present, is much more likely to have been produced at the host galaxy and not in the halo of an intervening galaxy within the LoS. In their Eq. 2, Ocker et al. (2021) determine a relationship between scattering, the electron density fluctuations of the medium, and a geometric factor that depends on the distances between FRB, scattering medium and observer:

$$\tau_{sc}(\text{DM}, \nu, z) \simeq 48.03 \text{ ns} \times \frac{A_\tau \tilde{F}(z_l) \text{DM}_l^2}{(1+z_l)^3 \nu^4} \left[\frac{2d_{sl}d_{lo}}{Ld_{so}} \right], \quad (18)$$

where $A_\tau \lesssim 1$ is a scaling factor to convert the mean delay to the $1/e$ delay obtained from the pulse shape fit, $\tilde{F}(z)$ in $\text{pc}^{-2/3} \text{km}^{-1/3}$ quantifies the electron density variations of the scattering lens, DM_l is the DM contribution from the scattering lens, z_l is the redshift of the scattering lens and ν is the observing frequency in GHz. d_{sl} , d_{lo} , and d_{so} are angular diameter distances in Gpc, with d_{sl} the source to lens distance, d_{lo} lens to observer, d_{so} source to observer. L is the thickness of the layer in Gpc, and the geometric boost factor $G_{sc} \simeq d_{sl}d_{lo}/Ld_{so}$. Note that, since all distances are measured in Gpc, τ_{sc} is measured in ns. When either the source or the observer are embedded in the scattering medium and the source to observer distance d is much larger than the medium's thickness L , $G_{sc} = 1$. The electron density fluctuations vary with redshift following the cosmic star formation rate (CSFR) as follows (Eq. 22 in Ocker et al. 2022a):

$$\tilde{F}(z) \simeq \tilde{F}_0 \times \frac{(1+z)^{2.7}}{1+1[(1+z)/2.9]^{5.6}}. \quad (19)$$

If the scattering lens is located in the host galaxy ($z_l = z_{\text{host}}$), \tilde{F}_0 can vary from 10^{-2} to $10^3 \text{pc}^{-2/3} \text{km}^{-1/3}$ by extrapolation from observations of MW pulsars in the Galactic plane. In this case, the FRB would be embedded in the scattering medium and d_{so} is much larger than the medium's thickness L , thus $G_{sc} = 1$. If, on the other hand, the scattering lens is a galactic halo falling within the FRB LoS, the electron density fluctuations are much lower. Galactic pulsars located in the

Milky Way thick disk (at 10–20 kpc distances) exhibit an $\tilde{F}_0 \sim 10^{-3} \text{pc}^{-2/3} \text{km}^{-1/3}$. An FRB traversing an intervening galactic halo would encounter a much more homogeneous medium, with $\tilde{F}_0 \sim 10^{-4} - 10^{-5} \text{pc}^{-2/3} \text{km}^{-1/3}$. Although the geometric boost factor is much larger for an intervening galaxy halo than for the medium where the source or the observer are embedded, the turbulence of the intervening halo is very small unless the FRB passes with a small impact parameter with respect to the galaxy centre.

In Fig. 24, we compare the expected τ_{sc} produced by the host galaxy medium and by an intervening galactic halo as a function of the lens DM contribution. We compute these values at 1.37 GHz for an FRB located at $z = 1$, the average redshift upper limit of scattered Apertif FRBs. For the host galaxy, we test a range of electron density fluctuations from 10^{-2} to 10^3 . For a scattering lens within the LoS of the FRB with a thickness of $L = 30$ kpc, we assume $\tilde{F}_0 = 10^{-4} \text{pc}^{-2/3} \text{km}^{-1/3}$ and test the τ_{sc} contribution at different distances varying from 10% to 90% of the host galaxy redshift.

We find the observed Apertif scattering timescales to be much more easily produced in the host galaxy than by an intervening galaxy halo located in the burst LoS. This is in agreement with Cordes et al. (2022), and it is further supported by the lack of observable scattering in other FRBs which are known to travel through the halos of foreground galaxies. This is the case for FRB 20191108A, which passes through the halos of M33 and M31 with an impact parameter of 18 kpc from M33 (Connor et al. 2020) and FRB 20190709A passing $\gtrsim 25$ kpc away from the M33 centre (van Leeuwen et al. 2023), as well as the localised FRB 20181112A (Prochaska et al. 2019; Cho et al. 2020), and FRB 20190608B (Simha et al. 2020).

By modelling the dispersion and scattering produced throughout the travel path of an FRB, Chawla et al. (2022) find that circumburst environments with strong scattering properties are required in order to reproduce the FRBs from the first CHIME/FRB catalogue with $\tau_{sc} > 10$ ms at 600 MHz. This corresponds to ~ 0.37 ms at 1370 MHz, which roughly matches the lowest measured Apertif scattering timescale. Although Chawla et al. (2022) suggest intervening galaxies within the burst LoS as an alternative explanation, we have determined above that this scenario is more unlikely given the low fluctuation parameter observed in the MW halo (Ocker et al. 2021). A very low impact parameter with respect to the centre of the intervening galaxy ($\lesssim 10$ kpc for a MW-like galaxy, or roughly $\lesssim 15\%$ of the virial radius as assumed in Section 5.1.7) would be required in order to produce significant scattering.

A correlation between τ_{sc} and DM might have been an indication of a significant contribution to scattering from the IGM or intervening host galaxies. Meanwhile, scattering in the host galaxy would be highly dependent on the type of galaxy and its inclination, hence no correlation would be expected. The lack of a significant τ_{sc} –DM correlation supports an origin of scattering in the FRB host galaxies.

In addition to the measured scattering timescales at 1.37 GHz, the scattering indices α can provide valuable insights into the properties of the media the FRBs have travelled through. In the most simple scenario, scattering produced by a thin screen would result in a scattering index of $\alpha = 4$, while propagation through a uniform Kolmogorov turbulent medium would produce a scattering index of $\alpha = 4.4$. Of the seven Apertif FRBs with measurable scattering timescales and indices, four are compatible with $\alpha = 4$, while only three are compatible with $\alpha = 4.4$. Three of the bursts present larger scattering indices, incompatible with both a thin screen and a Kolmogorov turbulence model,

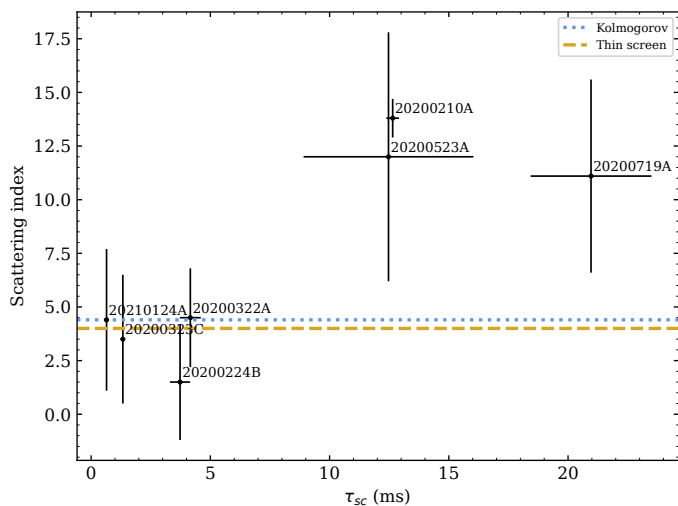


Fig. 25. Scattering index as a function of scattering timescale. The black markers with error bars show the Apertif FRBs where these could be measured, with the TNS name of each indicated next to the marker. The golden dashed horizontal line represents a scattering index of 4, as expected from a thin screen, and the blue dotted line the scattering index of 4.4 expected from Kolmogorov turbulences.

as can be seen in Fig. 25. FRB 20200523A and FRB 20200719A have low S/N and the scattering timescale can only be measured in two subbands, so we decide not to draw conclusions from them. However, FRB 20200210A was bright enough to divide the bandwidth into 16 subbands and measure the scattering in the top six ones, obtaining a robust scattering index of $\alpha = 13.8 \pm 0.9$. The highest scattering index ever measured in pulsars is $\alpha = 9.76$ for B1834–04 (Lewandowski et al. 2013). However, the authors consider this measurement doubtful since scattering was only measured at two different frequencies. Scattering index measurements in FRBs, on the other hand, are still scarce. Sammons et al. (2023) measure a steep scattering index $\alpha = 7.3 \pm 0.9$ within a narrow observing bandwidth for the repeater FRB 20201124A, but an index of $\alpha \sim 4$ is required to make their scattering measurement consistent with previous observations. The simplicity of the models that predict scattering indices of $\alpha = 4$ or $\alpha = 4.4$ is unlikely to apply to more complicated geometries that could arise, for instance, in a clumpy medium, or throughout the inhomogeneities that FRBs are likely to encounter along their travel paths. Walker et al. (2017) showed that molecular clumps around hot stars appear to be responsible for extreme radio scintillation events of background radio sources. In the case of FRB 20200210A, a clumpy medium around the source could explain both the large scattering timescale and the steep scattering index. However, further studies are required to understand the origin of such anomalous scattering indices.

From our observations, we can thus conclude that the Apertif FRBs with measurable scattering are likely to be embedded in an environment with extreme properties. Such extreme environments could for instance be star-forming regions or supernova remnants, as has been previously suggested in e.g. Masui et al. (2015); Connor et al. (2016) and Xu & Zhang (2016).

6.1.4. Dispersion

In their analysis, earlier surveys have compared FRB fluences against their extragalactic DMs, to show that bright, nearby FRBs have energies comparable to the more distant, fainter

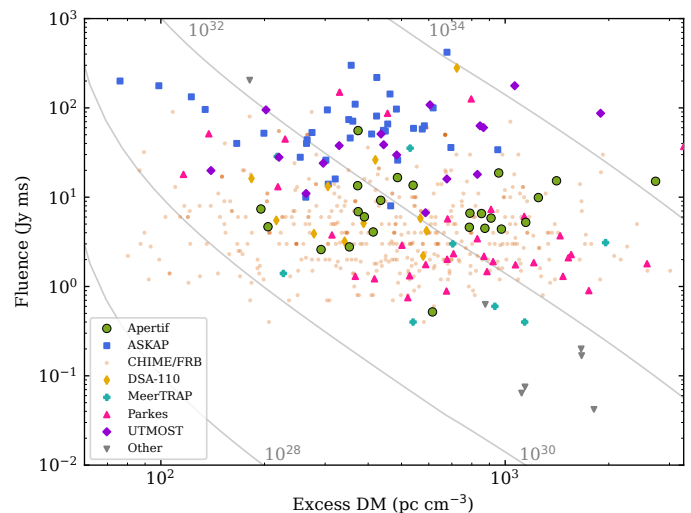


Fig. 26. Fluence–excess DM diagram of Apertif and all other FRBs in the TNS. Apertif is shown as green circles, ASKAP as blue squares, DSA-110 as yellow diamonds, MeerTRAP as turquoise crosses, Parkes as pink upward triangles, UTMOST as purple diamonds, CHIME/FRB as orange dots with a high transparency for better visualisation, and all other FRBs as grey downward triangles. Lines of constant spectral energy density are shown as grey lines for reference, with their labels indicating their value in erg Hz^{-1} .

FRBs (Shannon et al. 2018; Farah et al. 2019; Niu et al. 2021). The Apertif sample is no different, as visible in Fig. 26, where we display this fluence-DM plane. For guidance, the grey lines represent the equivalent isotropic energy density that FRBs would have assuming the IGM DM contribution from Zhang (2018) and the cosmological parameters from Planck Collaboration et al. (2020). We adopt an observed host galaxy contribution to the DM of $50/(1+z)$ pc cm^{-3} for consistency with Shannon et al. (2018) and Petroff et al. (2019). The Apertif FRBs are located between the Parkes and the UTMOST FRB samples within the fluence-excess DM plane, while overlapping the FRBs from the First CHIME/FRB Catalog. This is in agreement with the DM distributions shown in Fig. 19 and the fluence-dependent rates presented in Fig. 18.

The Apertif sample contains the FRB with the third largest DM known to date, FRB 20200719A, at $z_{\text{Macquart}} \sim 3.26^{+0.62}_{-1.35}$ (Sect. 5.1.7). The maximum cosmic star formation rate (CSFR) took place at $z \sim 2$ (Madau & Dickinson 2014); FRB 20200719A could thus have been emitted beyond the CSFR peak. Previous works have compared the CHIME/FRB DM distribution to cosmic evolution models, and have found it does not appear to track the star formation history of the Universe (Qiang et al. 2022; Zhang & Zhang 2022). As most FRB progenitor models are based on or related to stellar populations, and given that the CSFR decreases by over an order of magnitude from its peak to the current era, we find those results surprising. Recently, however, Wang & van Leeuwen (2024) combined for the first time a full multi-dimensional Markov chain Monte Carlo search around the population synthesis code of Gardenier et al. (2019), with the inclusion of the full set of CHIME one-off FRBs. They find strong evidence that the FRB number density follows the CSFR. Detecting additional FRBs like FRB 20200719A at very large DMs and thus redshifts will better constrain the FRB rate evolution with redshift. Comparing the FRB host galaxy properties to that of other astrophysical transients has proved useful in con-

straining the potential FRB progenitors (Heintz et al. 2020; Safarzadeh et al. 2020; Mannings et al. 2021; Bhandari et al. 2022); the redshift distribution could provide with additional information to rule out some of the current FRB progenitor models. However, the detection of some classes of transients is currently observationally challenging. Long Gamma-ray bursts (LGRBs) have been identified with redshifts up to $z \sim 9$ mainly with the Swift satellite (Cucchiara et al. 2011; Lan et al. 2021), while the most distant short Gamma-ray burst (SGRB) was found at a redshift of $z \sim 2.2$ (Selsing et al. 2018). This can be explained by a lower Swift sensitivity to high redshift SGRBs compared to LGRBs (Guetta & Piran 2005). The detection of distant optical transients is also limited; the most distant type Ia supernova has a redshift of only $z \sim 1.9$ (Jones et al. 2013), while core-collapse supernovae (CCSN) have been found up to $z \sim 2.4$ (Cooke et al. 2009) and superluminous supernovae (SLSN) up to $z \sim 3.9$ (Cooke et al. 2012). If a link is established between FRBs and any of these transients, high DM bursts might help establishing the cosmic evolution of their progenitors.

6.1.5. Scintillation

The scintillation bandwidths of the FRBs in our sample, when measurable, fall within the error range of the expected NE2001 contribution, but in most cases they are larger than the predictions. This might indicate the electron density along the LoS fluctuates less than predicted by these models. The YMW16 predicted scintillation is generally also lower than the Apertif measured values. This may be explained by the way the model predicts the scattering/scintillation values; it uses the $\tau_{\text{sc}} - \text{DM}$ relation instead of modelling the electron density fluctuations along the LoS (Yao et al. 2017). The scintillation measurements of Apertif FRBs can thus prove useful in better constraining the Milky Way electron distribution, especially at high Galactic latitudes where there is a dearth of pulsars.

In Fig. 23, we plot the Apertif scintillation bandwidths converted to scattering timescales through Eq. 13, as a function of the expected Galactic contribution to DM (since we expect the scintillation to be produced in the MW). The measured values do not follow the $\tau_{\text{sc}} - \text{DM}$ relation from Bhat et al. (2004) and Cordes & Chatterjee (2019) for Galactic pulsars. Since pulsars generally lie in the Galactic plane, they probe a more inhomogeneous medium than the Galactic halo encountered by most FRBs (Ocker et al. 2021). It is thus understandable that FRBs do not follow the same relation as pulsars.

6.2. Multi-component bursts

In the Apertif FRB sample, we find $\sim 30\%$ of the bursts to display multiple components. Although this is at odds with the 5% multi-component fraction reported for the first CHIME/FRB catalogue (Pleunis et al. 2021a), it appears to be consistent with the fraction observed in the baseband data subset (CHIME/FRB Collaboration et al. 2023b). We determined the CHIME/FRB multi-component fraction by visual inspection of the dynamic spectra, which are mostly downsampled to a $81.9 \mu\text{s}$, very close to the Apertif time resolution.

Since CHIME/FRB observes at a lower frequency than Apertif did, their detected bursts should be more smeared by scattering. Additionally, we have shown that there is a population of highly scattered bursts to which CHIME/FRB is not sensitive. Scattering smearing is likely to blur together closely spaced subcomponents, and thus one would expect the observed frac-

tion of multi-component FRBs to decrease at lower frequencies if the subcomponent fraction remains the same. We must consider however the selection effects that the CHIME/FRB baseband pipeline could have on the observed population, since only bursts with $S/N > 10$ -12 have a baseband trigger, compared to the $S/N > 8$ trigger threshold to store the intensity data. These different thresholds could be producing a bias in the multi-component fraction of the observed population.

Studies comparing multi-component fractions at different frequencies are still scarce, but current and upcoming FRB surveys with access to high spectro-temporal resolution data, such as MeerTRAP (Rajwade et al. 2021), the Deep Synoptic Array 110 (DSA-110; Kocz et al. 2019), or the CRAFT COherent upgrade at ASKAP (CRACO; e.g. Scott et al. 2023), will soon produce large samples of FRBs in the L-band. Comparing the fraction of multi-component FRBs at different frequencies might provide with important clues about the FRB emission mechanism.

If high time resolution studies at lower or higher frequencies detect fewer or more multi-component bursts, respectively, at a level inconsistent with smearing due to scattering or instrumental effects, this would support the existence of frequency-dependent morphology for the population of one-off FRBs. Such frequency-dependent effects are seen for pulse components of radio pulsars due to the different emission heights of different radio frequencies in the pulsar beam, so-called radius-to-frequency mapping (RFM; see, e.g., Cordes 1978). This RFM has been suggested to explain the drift rate evolution with frequency observed in repeating FRBs (Lyutikov 2020; Tong et al. 2022; Bilous et al. 2022). Observing a similar frequency-dependent relationship in one-off FRB pulse components would provide further evidence for a neutron star origin for FRB emission.

The Apertif FRB components have an average width of ~ 0.5 ms, while for CHIME/FRB it is ~ 1 ms. In pulsars, the observed profile (and component) width over this same frequency range of 1.4 to 0.4 GHz evolves too, by an increase of $\sim 20\%$ (Table 1 in Kijak & Gil 1997). If this difference persists when CHIME/FRB collects a larger sample of FRBs with baseband data, this would indicate the evolution of FRB component width versus frequencies is of at least the same scale, if not more, as that seen in pulsars.

In Karastergiou & Johnston (2007), the profile classification of more than 250 pulsars revealed that 60% of young, fast-spinning, and highly energetic pulsars show single component average profiles while 40% show double component profiles, while for older, slower, and less energetic pulsars 45% are single profile, and the rest are either double or multi-component. Although we did not find any current estimates of the radio burst morphology distributions from the magnetar population, observations reveal complex radio bursts to be prevalent (Maan et al. 2022; Caleb et al. 2022; Kramer et al. 2023). The morphological similarities between radio-loud neutron stars and the observed FRBs suggest a link between the emission process of these phenomena.

We note that the Apertif sample consists entirely of one-off FRBs that have not been seen to repeat. While many previous morphological studies have focused on samples of bursts from known repeaters (Hewitt et al. 2022; Platts et al. 2021; Sand et al. 2022), the large fraction of multi-component bursts in a self-consistent sample of one-off FRBs is still novel. Ultimately, larger samples of high time resolution one-off FRBs detected by other facilities will be needed to fully contextualize the Apertif sample, as no further studies can be done with Apertif itself. However, we encourage other surveys to further explore the

morphological properties of one-off FRBs, as has been done by Faber et al. (2023). For large numbers, finding the patterns or groups that underlie the burst shapes could be done with unsupervised methods such as those proposed in Vohl et al. (2023).

6.3. Polarisation

We can classify the polarisation fractions of the 16 Apertif FRBs with full Stokes data into the four subgroups from Sherman et al. (2024). These subgroups were determined empirically based on 25 DSA-110 bursts, and they are the following: linearly polarised if $L/I > 70\%$ and $V/I < 30\%$, circularly polarised if $V/I > 30\%$, partially depolarised if $35\% < L/I < 70\%$ and $V/I < 30\%$, and unpolarised if $L/I < 35\%$ and $V/I < 30\%$. In our sample, we find FRBs belonging to all those categories except for the circular polarisation; 4/16 are linearly polarised, 6/16 are partially depolarised, and 6/16 are depolarised. The fraction of Apertif FRBs with (partial) linear polarisation of 62.5% is fully consistent with the 68% fraction found by DSA-110 (Sherman et al. 2024), as well as the $\sim 70\%$ fraction found in 128 bursts from CHIME/FRB (Pandhi et al. 2024).

The two FRBs with the lowest polarisation fractions, FRB 20200322A and FRB 20200323C, also have the largest scattering timescales of the bursts with full Stokes data. This could be explained if linearly polarised bursts travelled through an inhomogeneous magneto-ionic environment in the vicinity of the source, which would produce depolarisation as well as scattering. This effect has been proposed to explain the depolarisation of repeaters at low frequencies by Feng et al. (2022). They determine an empirical linear correlation between the RM scatter σ_{RM} and the scattering timescale τ_{sc} , where σ_{RM} can be obtained from the depolarisation fraction f_{RM} with the following equivalence:

$$f_{\text{RM}} \equiv 1 - e^{-2.1^4 \sigma_{\text{RM}}^2}. \quad (20)$$

The Apertif bursts with Stokes data and scattering timescale appear to follow the same relation. However, the upper limit on the scattering timescales for some of these bursts would place them below the limits of the expected relation. This could support the suggestion from Pandhi et al. (2024) that one-off FRBs do not always have an intrinsic 100% linear polarisation fraction. The correlation between σ_{RM} and $|\text{RM}|$ observed in Feng et al. (2022) does not appear to apply to the Apertif bursts.

It is noteworthy that the polarisation fraction of the Apertif FRBs overlap with what has been reported for a sample of 35 young and energetic pulsars observed for the thousand-pulsar-array (TPA) program with MeerKAT (Serylak et al. 2021). The linear polarisation fraction of the latter have a median a standard deviation of 49% and 27% respectively, while for ARTS FRBs it is 43% and 27%. The circular polarisation fraction, on the other hand, have a mean and standard deviation of 9% for TPA and 9% and 8% respectively for ARTS FRBs. This is further evidence for the potential link between young, high-energy pulsars and one-off FRBs.

The Apertif FRB sample contains some of the highest RMs ever observed in one-off FRBs, including FRB 20200216A with $\text{RM} = -2051 \text{ rad m}^{-2}$, as can be visualised in Fig. 27¹⁹. Although no one-off FRB has been yet found to have an RM as extreme as that observed for the repeaters FRB 20121102A (Hilmarsson et al. 2021) or FRB 20190520B (Anna-Thomas

¹⁹ The CHIME/FRB RMs from Pandhi et al. (2024) have not been included since the paper is currently under review and their tables are not available digitally yet.

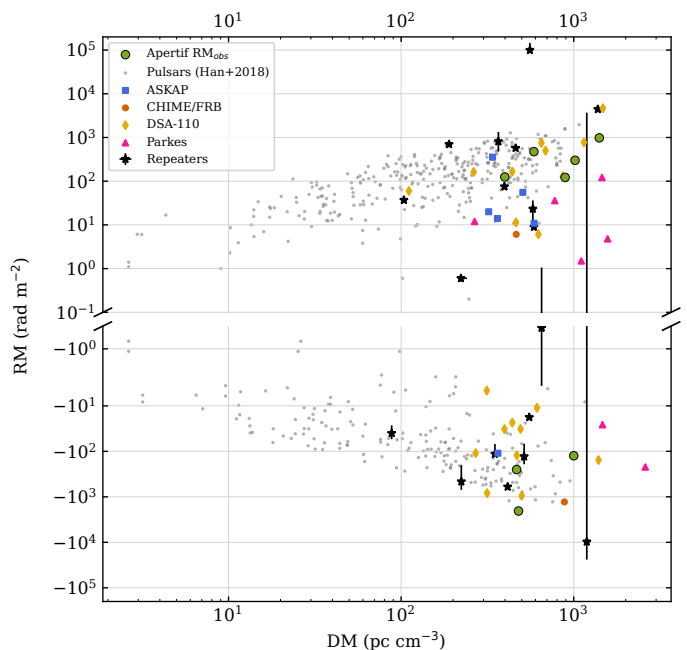


Fig. 27. Observed RM of one-off and repeating FRBs compared to galactic pulsars as a function of DM. The green circles show the observed Apertif RMs, the grey dots the measured pulsar RMs from Han et al. (2018), the blue squares are from ASKAP one-off FRBs, the orange circles from CHIME/FRB, the yellow diamonds from DSA-110, and the pink triangles from Parkes FRBs. The mean measured repeater RMs are shown as black stars with error bars showing the observed RM ranges of each source.

et al. 2023), we compared the RMs of repeaters and one-offs using a Kolmogorov-Smirnov (KS) test. We find a p-value of 0.51 if we compare the observed RMs, while the p-value is 0.61 if we correct the RMs for redshift with Equation 11. This indicates that the current sample of one-off and repeater RMs could have been drawn from the same distribution, implying that both FRB classes could be produced in environments with similar magneto-ionic properties. Pandhi et al. (2024) reach a similar conclusion using the CHIME/FRB polarisation sample, in line with the more general finding in Gardenier et al. (2021), based on a wider range of burst characteristics, that all FRBs originate from a single and mostly uniform population.

If we compare the observed RMs of one-off FRBs from Apertif, Sherman et al. (2024), and references therein to galactic pulsars, we obtain a KS p-value=0.48, suggesting that the distributions are compatible too. However, if instead we compare the redshift-corrected RMs, the p-value is 0.003, indicating that the RMs have been drawn from different distributions. This reveals that one-off FRBs could originate from environments more extreme than those where pulsars are usually located. Although RMs of the order of $|\text{RM}| \sim 100 \text{ rad m}^{-2}$ might be expected from FRBs originating from MW-like host galaxies with H_{II} regions, reaching $10^3 - 10^5 \text{ rad m}^{-2}$ would require the FRB to be emitted from a supernova remnant (SNR) or from a H_{II} region (Hackstein et al. 2019). Hence, a significant fraction of one-offs must be produced from within these environments to explain the observed Apertif RMs. Detecting further one-off FRBs with such extreme RMs might be easier in high frequency observations, since the RM oscillations in Q/U become stronger at lower frequencies, and might not be resolvable at the instrument's frequency resolution.

6.4. All-sky FRB rates and fluence distribution

From the ALERT survey, we compute an all-sky FRB rate at 1370 MHz of $R_{1370}(F \geq 4.1 \text{ Jy ms}) = 459^{+208}_{-155} \text{ sky}^{-1} \text{ day}^{-1}$, with 90% Poisson errors. The power-law fit to the fluence cumulative distribution above this 4.1 Jy ms completeness threshold next allows us to compare our rate to that of other surveys, even though they have different sensitivity limits (See Fig. 18). The resulting power law index for bursts above the threshold is $\gamma = -1.23 \pm 0.06 \pm 0.2$.

The Apertif all-sky rate is comparable to most other FRB surveys when accounting for their fluence sensitivity thresholds; in the L-band, ASKAP in fly’s-eye mode (Shannon et al. 2018), Parkes HTRU (Champion et al. 2016), SUPERB (Bhandari et al. 2018), MeerTRAP Coherent (Jankowski et al. 2023), as well as CHIME/FRB at 600 MHz (CHIME/FRB Collaboration et al. 2021), all report rates that agree with ours. The UTMOST rate at 843 MHz (Farah et al. 2019) agrees within 3σ , but this rate is obtained from a smaller burst sample. We thus see no evidence for an evolution of the FRB rate with frequency.

In a non-evolving, constant density Euclidean Universe, the expected power law index of the fluence distribution observed with a perfect telescope is $\gamma = -1.5$. Although our observed power law index appears to be flatter, we cannot rule out that it is consistent with the Euclidean prediction within systematic errors. We can compare the Apertif $\gamma = 1.23 \pm 0.26$ to what has been reported by other FRB surveys, as shown in Fig. 28. Bhandari et al. (2018) reported $\gamma = -2.2^{+0.6}_{-1.2}$ for the Parkes burst sample, while Shannon et al. (2018) determined $\gamma = -2.1^{+0.6}_{-0.5}$ for the ASKAP sample. James et al. (2019) later reanalysed these two FRB samples and determined the Parkes index to be $\gamma = -1.18 \pm 0.24$ and ASKAP to be $\gamma = -2.2 \pm 0.47$. While the combined power law index of both surveys is $\gamma = -1.55 \pm 0.23$, consistent with the Euclidean Universe, they are inconsistent with each other at 2.6σ . This discrepancy was interpreted as a difference in the cosmological population observed by each of these surveys, with ASKAP seeing nearby sources and Parkes more distant ones, following the average DM of each burst sample (See Fig. 19 and Table 1). Meanwhile, the index determined from the First CHIME/FRB Catalog is $\gamma = -1.40 \pm 0.11^{+0.060}_{-0.085}$, in agreement with the Euclidean prediction and in between the Parkes and ASKAP values (CHIME/FRB Collaboration et al. 2021). This appears to concur with the average DM of the CHIME/FRB sample compared to the other two surveys. These studies seemed to reveal an apparent increasing median-DM/power-law-index trend observed in the other surveys, which the Apertif FRBs also follow; the fluence cumulative distribution appeared to be flatter for a sample of FRBs with larger DMs and thus redshifts. However, recent results from MeerTRAP find power law exponents of $-1.7^{+0.2}_{-0.3}$ and $-1.8^{+0.3}_{-0.3}$ respectively for the incoherent (median DM $\sim 570 \text{ pc cm}^{-3}$) and coherent (median DM $\sim 1080 \text{ pc cm}^{-3}$) surveys (Jankowski et al. 2023), which is at odds with the apparent trend. Furthermore, when subdividing the CHIME/FRB catalog into high and low DM FRBs (above and below 500 pc cm^{-3}), these sub-samples also follow the opposite trend; the high DM sample has $\gamma = -1.75 \pm 0.15$ and the low DM sample $\gamma = -0.95 \pm 0.15$. We note that overall, a number of selection effects modify the single intrinsic γ into the observed one, which may then differ among surveys. At lower fluences, surveys become varyingly incomplete while FRBs at high fluences might be misidentified as RFI by certain processing choices. Pulses may be more easily detectable if they are intrinsically wide and bright, but harder to find if their width is result from dispersion smearing and scattering. These effects, discussed in e.g. Connor

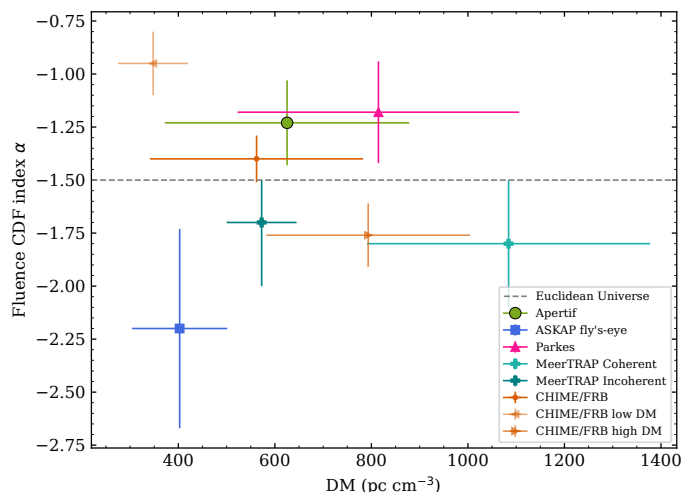


Fig. 28. Fluence cumulative distribution power law indices (γ) as a function of the DMs for each survey. Each data point gives the measured γ as a function of the median DM with median absolute deviation errors. ASKAP Fly’s-Eye survey is shown as a blue square (γ values from James et al. 2019), Parkes is shown as a pink triangle, MeerTRAP Coherent and Incoherent as turquoise and teal crosses respectively, CHIME/FRB as an orange square, the CHIME/FRB $< 500 \text{ pc cm}^{-3}$ sub-sample as a downwards orange triangle, CHIME/FRB $> 500 \text{ pc cm}^{-3}$ as an upwards triangle (CHIME/FRB Collaboration et al. 2021), and Apertif is represented by a green circle. The predicted $\gamma = -1.5$ for an Euclidean Universe is shown by a dashed grey line.

(2019), are simulated in e.g. Wang & van Leeuwen (2024). On average, the FRB sample observations mentioned in this section seem to be in agreement with the Euclidean Universe prediction. Future FRB detections and power law index measurements will provide with important information about how the FRB population evolves with redshift.

6.5. Higher-frequency emission

Although repeating FRBs have been observed to shine at frequencies as high as 8 GHz (Gajjar et al. 2018), no one-off FRBs have been reported above the L-band (Petroff et al. 2022). Since the observed FRB radio frequency ν_{obs} gets redshifted with distance, we can estimate the intrinsic, rest-frame frequencies at which these FRBs were emitted, $\nu_{0,\text{max}}$, from their expected redshifts: $\nu_{0,\text{max}} = \nu_{\text{obs}}(1+z_{\text{Macquart}})$. For localised FRBs, we use the host galaxy redshift instead. We plot the rest frame frequencies as a function of the estimated FRB isotropic energy (Eq. 9 from Zhang 2018) for all FRBs in the TNS database in Fig. 29, and we find 16 FRBs for which the estimated intrinsic emission frequency is $> 3 \text{ GHz}$; four from Apertif, eight from Parkes, three from FAST (Zhu et al. 2020; Niu et al. 2021), and one from MeerTRAP (Rajwade et al. 2022). For the FRB 20200719A presented in this work (Sect. 5.1.7 and Table A.2), and for the Parkes FRB 20160102A (Bhandari et al. 2018), the estimated emission frequency is $> 5 \text{ GHz}$. The detection of high-DM one-off FRBs in the L-band thus indicates that bursts are commonly emitted at higher frequencies.

Interestingly, a significant number of individual radio-loud magnetars are also observable at high frequencies (see e.g., Levin et al. 2012), more than normal radio pulsars. There is also population-based evidence of overlap in high-frequency behaviour between FRBs and magnetars (Gardenier & van

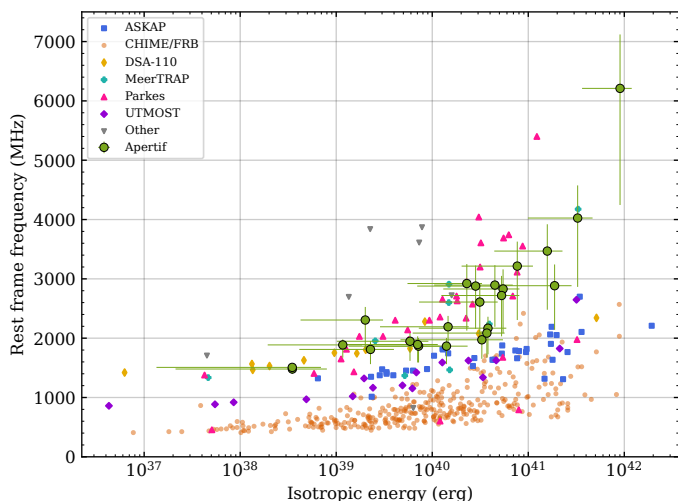


Fig. 29. Rest frame frequency as a function of the isotropic energy of all FRBs in the TNS and Apertif. Apertif FRBs are shown as green circles, ASKAP FRBs as blue squares, DSA-110 as yellow diamonds, MeerTRAP as turquoise crosses, Parkes FRBs as pink upwards triangles, UTMOST as purple diamonds, CHIME/FRB as orange circles, and all other FRBs as grey downwards triangles. Both the rest frame frequency and isotropic energy have large error bars (not shown for better visualisation) with the exception of localised FRBs.

Leeuwen 2021). Our detection of emission at an inferred frequency > 5 GHz strengthens the case that FRBs are emitted by magnetar-like sources.

The strong correlation visible in Fig. 29, between the rest-frame frequency and the FRB isotropic energy, can be well explained by the selection effect caused by the equivalence between the redshift and distance, that together determine in which frequency the FRBs are observed. Less energetic high-frequency FRBs most likely exist too, and fill the top-left part of the Fig. 29 parameter space, but the current low- and mid-frequency surveys cannot easily detect those. Nevertheless, if FRBs had steep, declining spectral indices, a source like FRB 20200719A could not exist. Our finding that an FRB can produce $E_{\text{iso}} = 9.0 \times 10^{41}$ erg above 5 GHz means the spectral index of FRBs cannot be too steeply negative. A quantitative assessment of the allowed values can only come from multi-survey population modeling (as discussed in e.g. Wang & van Leeuwen 2024).

6.6. Motivation for future observations

Now that we know that FRBs emit at higher frequencies, searches for local FRBs in the S-band (2–4 GHz) and above are interesting. Although the generally smaller FoV reduces the raw detection rates, the individual beams shrink equally with increasing frequency, allowing for better localisation. When enough beams can be formed and searched, interferometric S-band searches such as those with the MeerKAT 1.75–3.5 GHz system (Kramer et al. 2018) could be fruitful.

Apertif operations have ceased and the ALERT survey finished. The science case for continued GHz FRB searching remains strong. From a larger sample of real-time detections, with immediate alerting and repointing of lower-frequency observatories, we can determine the emission bandwidth of one-off FRBs, and understand their emission mechanism. Based on the work presented here, a larger sample of 1.4 GHz bursts could be investigated specifically for scattering and multi-component

bursts. Such a system could be implemented as a coarse, total-intensity real-time search that preserves baseband data for detections. While the 1-dimensional nature of the WSRT allowed for full-field beamforming, it did limit the overall localisation precision. Up to now, 2-D interferometers equipped with PAFs (i.e., ASKAP) have not been able to tile out the complete primary beam with TABs, reducing the sensitivity (either through incoherent beamforming, or through the longer integration times in imaging mode). The \sim ms integration upgrade to ASKAP for coherent FRB detection over the entire FoV will increase detection rates while also providing good localisation.

As each WSRT dish has a large collecting area for a "large number–small diameter" array, improvements to the front ends can be a cost-effective way to increase the system sensitivity. Cryogenically cooled PAFs combine the strengths of the current system with reduced SEFD (Navarrini et al. 2018; Pingel et al. 2021). Such a successor to Apertif would increase the detection rate by a factor ~ 4 , and provide better localisation through the higher detection S/N.

7. Conclusions

In this work, we have reported the discovery of 18 new, so-far one-off, FRBs, and analysed the properties of the total of 24 bursts that were detected during the ALERT Apertif FRB survey between July 2019 and February 2022. For each FRB, we determine the localisation region and expected redshift range and perform a flux calibration. We evaluate their morphology, determining the number of components and the spectral properties, and we study the propagation effects by verifying the presence of a resolved scattering tail in time and a scintillation pattern in frequency.

We localise each FRB to a narrow ellipse whose area depends on the detection S/N and the number of CBs where it was detected. The average localisation area is ~ 5 arcmin². For five new FRBs with a high S/N and a low DM, namely FRB 20200210A, FRB 20200419A, FRB 20200518A, FRB 20210317A, and FRB 20211024B, we find a small number of host galaxy candidates in the PanSTARRS DR1 catalogue, ≤ 5 , in which one of the galaxies has a PATH probability of being associated with the FRB $> 50\%$. In the case of FRB 20200419A, we find a single host galaxy candidate with $P(G_1|x) = 70\%$. For the remaining FRBs we expect too many galaxies within their comoving volume to uniquely identify the host galaxy.

The dispersion measure of our FRB sample resembles that of the Parkes (Champion et al. 2016; Bhandari et al. 2018), UTMOST (Farah et al. 2019), and MeerTRAP (Jankowski et al. 2023) FRBs. The median DM is around 100 to 200 pc cm⁻³ higher than the CHIME/FRB (CHIME/FRB Collaboration et al. 2021), ASKAP (Shannon et al. 2018; Macquart et al. 2020), and DSA-100 (Law et al. 2024) samples. For the ASKAP sample, we cannot reject that the DMs have been drawn from a different intrinsic distribution than the Apertif FRBs. The larger Apertif DMs allow Apertif to observe a more distant population of FRBs than ASKAP. Furthermore, one of the Apertif bursts, FRB 20200719A, has the third largest DM of any FRB published to date, with $DM \sim 2778$ pc cm⁻³. Its derived redshift $z \sim 3$ implies that one-off FRBs also emit above 5 GHz, a frequency resembling magnetar bursts, and could be detected in the S-band. In the future, a large sample of highly dispersed FRBs like this one will help us determine the FRB rate as the Universe evolved.

We find the observed scintillation bandwidth of most FRBs to be compatible with the expected Milky Way contribution from

the NE2001 model within errors, although in many cases the measured values tend to be larger. Since most FRBs are detected at high Galactic latitudes, this might be evidence that the MW ISM at high Galactic latitudes is more uniform than models predict, which is evidence that FRBs could be valuable tools for improving our knowledge on the Galactic electron density distribution.

For 16 out of the 24 FRBs, ARTS triggered the capture of full Stokes data. The distribution of polarisation characteristics of these FRBs (linear, circular, depolarised) is identical to that seen in young, energetic pulsars.

A significant fraction of the FRBs display a scattering tail > 0.2 ms at 1370 MHz. Most of these τ_{sc} are hence above the CHIME/FRB scattering sensitivity limit of 10 ms at 600 MHz, accounting for the difference in frequency. They thus reveal a population of highly scattered bursts unlikely to be detected at lower frequencies. Such large scattering timescales could be produced either in the burst environment or an intervening galaxy within the LoS (Chawla et al. 2022). For low redshift FRBs ($z \lesssim 1$), the low chances of intersecting a galaxy with a small impact parameter make a dense circumburst environment the most likely explanation. In the case of FRB 20200210A, the large scattering tail allows us to estimate its redshift to be $z \sim 0.11$ from a joint scattering-DM analysis (Cordes et al. 2022). From the simultaneous presence of scattering and scintillation, we can put an upper limit constraint of 2 kpc between the FRB and a first scattering screen. This confirms the observed scattering was produced within the host galaxy. Fast Radio Burst surveys at high frequencies, such as ALERT, offer the opportunity of studying FRBs produced in dense environments that would not be detectable at lower frequencies due to the increased scattering timescales and thus lower S/N. We hypothesise these dense environments to be the star-forming regions or supernova remnants around FRB-emitting neutron stars. This is corroborated by the very high RMs we find in a number of one-off FRBs.

Roughly $\sim 30\%$ of the bursts are composed of multiple components. Worth mentioning are the structures of FRB 20200216A, FRB 20200518A and FRB 20210530A, which display more than two subcomponents each. None show evidence for (quasi-)periodic behaviour similar to that seen in FRB 20201020A (Pastor-Marazuela et al. 2023). The $\sim 30\%$ fraction appears to be consistent with the multi-component fraction observed in the CHIME/FRB baseband data (CHIME/FRB Collaboration et al. 2023b), which is unexpected since the stronger scattering at lower frequencies should blur together closely spaced subcomponents. Interestingly, the multi-component fraction is similar to that seen in pulsars. Further morphological studies at different bandwidths will reveal whether an evolution of the multi-component fraction or separation exists, which will shed light on the emission mechanism of FRBs.

We conclude that high time and frequency resolution such as provided by Apertif, combined with polarisation and localisation capabilities, are essential for making progress in our understanding of FRBs. Our comprehensive analysis of this set of Apertif discoveries, one of the largest uniform samples at 1.4 GHz to date, shows striking similarities between FRBs and young, energetic neutron stars.

Acknowledgements. We thank Jim Cordes and Stella Ocker for their useful input; Marten van Kerkwijk and Lucy Oswald for interesting discussions; Eric Kooistra, Jonathan Hargreaves, Daniel van der Schuur, Jisk Attema, Wim van Cappellen, André Gunst, Tom Oosterloo, Betsey Adams, Stefan Wijnholds and many, many others for conceiving and building Apertif and ARTS; and Samayra Straal, Oliver Boersma, Pikky Atri, and Kaustubh Rajwade for help with the ob-

servations. This research was supported by the European Research Council under the European Union's Seventh Framework Programme (FP/2007-2013)/ERC Grant Agreement No. 617199 ('ALERT'). Further research support was provided by Vici research project 'ARGO' with project number 639.043.815 and by 'CORTEX' (NWA.1160.18.316), under the research programme NWA-ORC; both financed by the Dutch Research Council (NWO). Instrumentation development was supported by NWO (grant 614.061.613 'ARTS') and the Netherlands Research School for Astronomy ('NOVA4-ARTS', 'NOVA-NW3', and 'NOVA5-NW3-10.3.5.14'). PI of aforementioned grants is JvL. IPM further acknowledges funding from an NWO Rubicon Fellowship, project number 019.221EN.019. EP further acknowledges funding from an NWO Veni Fellowship. DV acknowledges support from the Netherlands eScience Center (NLeSC) under grant ASDI.15.406. This work makes use of data from the Apertif system installed at the Westerbork Synthesis Radio Telescope owned by ASTRON. ASTRON, the Netherlands Institute for Radio Astronomy, is an institute of NWO.

References

- Adams, E. A. K., & van Leeuwen, J. 2019, *Nature Astronomy*, 3, 188
- Adams, E. A. K., Adebahr, B., de Blok, W. J. G., et al. 2022, *Astronomy & Astrophysics*, 667, A38
- Aggarwal, K., Budavári, T., Deller, A. T., et al. 2021, *The Astrophysical Journal*, 911, 95
- Anna-Thomas, R., Connor, L., Dai, S., et al. 2023, *Science*, 380, 599
- Bailes, M. 2022, *Science*, 378, eabj3043
- Baldry, I. K., Driver, S. P., Loveday, J., et al. 2012, *Monthly Notices of the Royal Astronomical Society*, no
- Bannister, K. W., Shannon, R. M., Macquart, J.-P., et al. 2017, *The Astrophysical Journal*, 841, L12
- Beck, R., Szapudi, I., Flewelling, H., et al. 2021, *Monthly Notices of the Royal Astronomical Society*, 500, 1633
- Bhandari, S., Keane, E. F., Barr, E. D., et al. 2018, *Monthly Notices of the Royal Astronomical Society*, 475, 1427
- Bhandari, S., Heintz, K. E., Aggarwal, K., et al. 2022, *The Astronomical Journal*, 163, 69
- Bhardwaj, M., Gaensler, B. M., Kaspi, V. M., et al. 2021, *The Astrophysical Journal Letters*, 910, L18
- Bhat, N. D. R., Cordes, J. M., Camilo, F., Nice, D. J., & Lorimer, D. R. 2004, *The Astrophysical Journal*, 605, 759
- Bhat, N. D. R., Gupta, Y., & Rao, A. P. 1998, *The Astrophysical Journal*, 500, 262
- Bilous, A. V., Griebmeier, J. M., Pennucci, T., et al. 2022, *A&A*, 658, A143
- Bilous, A. V., van Leeuwen, J., Pastor-Marazuela, I., et al. 2024, *A&A*, in prep.
- Bochenek, C. D., Ravi, V., Belov, K. V., et al. 2020, *Nature*, 587, 59
- Brentjens, M. A., & Bruyn, A. G. d. 2005, *Astronomy & Astrophysics*, 441, 1217
- Bruni, G., Piro, L., Yang, Y.-P., et al. 2023
- Burke-Spolaor, S., & Bannister, K. W. 2014, *The Astrophysical Journal*, 792, 19
- Burn, B. J. 1966, *Monthly Notices of the Royal Astronomical Society*, 133, 67
- Caleb, M., Flynn, C., Bailes, M., et al. 2017, *Monthly Notices of the Royal Astronomical Society*, 468, 3746
- Caleb, M., Heywood, I., Rajwade, K., et al. 2022, *Nature Astronomy*, 1
- Chambers, K. C., Magnier, E. A., Metcalfe, N., et al. 2019, *arXiv:1612.05560 [astro-ph.IM]*
- Champion, D. J., Petroff, E., Kramer, M., et al. 2016, *Monthly Notices of the Royal Astronomical Society: Letters*, 460, L30
- Chatterjee, S., Law, C. J., Wharton, R. S., et al. 2017, *Nature*, 541, 58, arXiv: 1701.01098
- Chawla, P., Kaspi, V. M., Ransom, S. M., et al. 2022, *The Astrophysical Journal*, 927, 35
- CHIME/FRB Collaboration. 2019, *Nature*, 566, 235
- CHIME/FRB Collaboration, Andersen, B. C., Bandura, K., et al. 2019, *The Astrophysical Journal Letters*, 885
- CHIME/FRB Collaboration, Andersen, B., Bandura, K., et al. 2020, *Nature*, 587, 54
- CHIME/FRB Collaboration, Amiri, M., Andersen, B. C., et al. 2021, *The Astrophysical Journal Supplement Series*, 257, 59
- CHIME/FRB Collaboration, Andersen, B. C., Bandura, K., et al. 2023a, *The Astrophysical Journal*, 947, 83
- CHIME/FRB Collaboration, Amiri, M., Andersen, B. C., et al. 2023b
- Cho, H., Macquart, J.-P., Shannon, R. M., et al. 2020, *arXiv:2002.12539 [astro-ph]*
- Connor, L. 2019, *MNRAS*, 487, 5753
- Connor, L., & Ravi, V. 2022, *Nature Astronomy*, 6, 1035
- Connor, L., Sievers, J., & Pen, U.-L. 2016, *Monthly Notices of the Royal Astronomical Society: Letters*
- Connor, L., & van Leeuwen, J. 2018, *The Astronomical Journal*, 156, 256
- . 2024, *Zenodo*, 10656614

- Connor, L., van Leeuwen, J., Oostrum, L. C., et al. 2020, *Monthly Notices of the Royal Astronomical Society*, 499, 4716
- Cooke, J., Sullivan, M., Barton, E. J., et al. 2009, *Nature*, 460, 237
- Cooke, J., Sullivan, M., Gal-Yam, A., et al. 2012, *Nature*, 491, 228
- Cordes, J. M. 1978, *The Astrophysical Journal*, 222, 1006
- Cordes, J. M., & Chatterjee, S. 2019, *Annual Review of Astronomy and Astrophysics*, 57, 417
- Cordes, J. M., & Lazio, T. J. W. 2003, [arXiv:astro-ph/0207156](https://arxiv.org/abs/astro-ph/0207156)
- Cordes, J. M., Ocker, S. K., & Chatterjee, S. 2022, *The Astrophysical Journal*, 931, 88
- Cordes, J. M., & Rickett, B. J. 1998, *The Astrophysical Journal*, 507, 846
- Cordes, J. M., Wharton, R. S., Spitler, L. G., Chatterjee, S., & Wasserman, I. 2016, [arXiv:1605.05890](https://arxiv.org/abs/1605.05890) [astro-ph]
- Crawford, F., Hisano, S., Golden, M., et al. 2022, *MNRAS*, 515, 3698
- Cucchiara, A., Levan, A. J., Fox, D. B., et al. 2011, *The Astrophysical Journal*, 736, 7
- Day, C. K., Deller, A. T., Shannon, R. M., et al. 2020, *Monthly Notices of the Royal Astronomical Society*, 497, 3335
- Deng, W., & Zhang, B. 2014, *The Astrophysical Journal*, 783, L35
- Duchesne, S. W., Thomson, A. J. M., Pritchard, J., et al. 2023, *Publications of the Astronomical Society of Australia*, 40, e034
- Eftekhari, T., & Berger, E. 2017, *The Astrophysical Journal*, 849, 162
- Faber, J. T., Michilli, D., Mckinven, R., et al. 2023
- Faber, S. M., Willmer, C. N. A., Wolf, C., et al. 2007, *The Astrophysical Journal*, 665, 265
- Farah, W., Flynn, C., Bailes, M., et al. 2018, *Monthly Notices of the Royal Astronomical Society*, 478, 1209
- . 2019, *Monthly Notices of the Royal Astronomical Society*, 488, 2989
- Feigelson, E. D., & Babu, G. J. 2012, *Modern Statistical Methods for Astronomy: With R Applications* (New York: Cambridge University Press)
- Feng, Y., Li, D., Yang, Y.-P., et al. 2022, *Science*, 375, 1266
- Fonseca, E., Andersen, B. C., Bhardwaj, M., et al. 2020, *The Astrophysical Journal*, 891, L6
- Gajjar, V., Siemion, A. P. V., Price, D. C., et al. 2018, *The Astrophysical Journal*, 863, 2
- Gardenier, D. W., Connor, L., van Leeuwen, J., Oostrum, L. C., & Petroff, E. 2021, *A&A*, 647, A30
- Gardenier, D. W., Leeuwen, J. v., Connor, L., & Petroff, E. 2019, *Astronomy & Astrophysics*, 632, A125
- Gardenier, D. W., & van Leeuwen, J. 2021, *Astronomy & Astrophysics*, 651, A63
- Gehrels, N. 1986, *The Astrophysical Journal*, 303, 336
- Gordon, A. C., Fong, W.-f., Kilpatrick, C. D., et al. 2023, *The Astrophysical Journal*, 954, 80
- Gruzinov, A., & Levin, Y. 2019, *The Astrophysical Journal*, 876, 74
- Guetta, D., & Piran, T. 2005, *Astronomy & Astrophysics*, 435, 421
- Hackstein, S., Brügger, M., Vazza, F., Gaensler, B. M., & Heesen, V. 2019, *Monthly Notices of the Royal Astronomical Society*, 488, 4220
- Han, J. L., Manchester, R. N., Straten, W. v., & Demorest, P. 2018, *The Astrophysical Journal Supplement Series*, 234, 11
- Haynes, M. P., Giovanelli, R., Martin, A. M., et al. 2011, *The Astronomical Journal*, 142, 170
- Heintz, K. E., Prochaska, J. X., Simha, S., et al. 2020, *The Astrophysical Journal*, 903, 152
- Helsel, D. R. 2004, *Nondetects and Data Analysis: Statistics for Censored Environmental Data*, 1st edn. (Hoboken, N.J.: Wiley-Interscience)
- Hess, K. M., Dénes, H., Oostrum, L., & Adams, E. A. K. 2022, [knhess/apersched: apersched v1.0.0](https://arxiv.org/abs/2208.003)
- Hessels, J. W. T., Spitler, L. G., Seymour, A. D., et al. 2019, *The Astrophysical Journal Letters*, 876
- Hewitt, D. M., Snelders, M. P., Hessels, J. W. T., et al. 2022, *Monthly Notices of the Royal Astronomical Society*, 515, 3577
- Hilmarsson, G. H., Michilli, D., Spitler, L. G., et al. 2021, *The Astrophysical Journal*, 908, L10
- Hutschenreuter, S., Anderson, C. S., Betti, S., et al. 2022, *Astronomy & Astrophysics*, 657, A43
- James, C. W., Ekers, R. D., Macquart, J.-P., Bannister, K. W., & Shannon, R. M. 2019, *Monthly Notices of the Royal Astronomical Society*, 483, 1342
- Jankowski, F. 2022, *Astrophysics Source Code Library*, [ascl:2208.003](https://arxiv.org/abs/2208.003)
- Jankowski, F., Bezuidenhout, M. C., Caleb, M., et al. 2023, *Monthly Notices of the Royal Astronomical Society*, 524, 4275
- Jones, D. O., Rodney, S. A., Riess, A. G., et al. 2013, *The Astrophysical Journal*, 768, 166
- Karastergiou, A., & Johnston, S. 2007, *Monthly Notices of the Royal Astronomical Society*, 380, 1678
- Keane, E. F., Stappers, B. W., Kramer, M., & Lyne, A. G. 2012, *Monthly Notices of the Royal Astronomical Society: Letters*, 425, L71
- Keane, E. F., Johnston, S., Bhandari, S., et al. 2016, *Nature*, 530, 453
- Kijak, J., & Gil, J. 1997, *Monthly Notices of the Royal Astronomical Society*, 288, 631
- Kirsten, F., Marcote, B., Nimmo, K., et al. 2022, *Nature*, 602, 585
- Kocz, J., Ravi, V., Catha, M., et al. 2019, *Monthly Notices of the Royal Astronomical Society*, 489, 919
- Kramer, M., Liu, K., Desvignes, G., Karuppusamy, R., & Stappers, B. W. 2023, *Nature Astronomy*, 1
- Kramer, M., Menten, K., Barr, E. D., et al. 2018, in *Proceedings of MeerKAT Science: On the Pathway to the SKA — PoS(MeerKAT2016)*, Vol. 277 (SISSA Medialab), 003
- Kravtsov, A. V. 2013, *The Astrophysical Journal*, 764, L31
- Kron, R. G. 1980, *The Astrophysical Journal Supplement Series*, 43, 305
- Lan, G.-X., Wei, J.-J., Zeng, H.-D., Li, Y., & Wu, X.-F. 2021, *Monthly Notices of the Royal Astronomical Society*, 508, 52
- Law, C. J., Sharma, K., Ravi, V., et al. 2024, *The Astrophysical Journal*, 967, 29
- Lee, K.-G., Khrykin, I. S., Simha, S., et al. 2023, *ApJ*, 954, L7
- Levin, L., Bailes, M., Bates, S. D., et al. 2012, *MNRAS*, 422, 2489
- Lewandowski, W., Dembska, M., Kijak, J., & Kowalińska, M. 2013, *Monthly Notices of the Royal Astronomical Society*, 434, 69
- Lorimer, D., & Kramer, M. 2004, *Handbook of Pulsar Astronomy.pdf*, Cambridge Observing Handbooks for Research Astronomers No. 4
- Lorimer, D. R., Bailes, M., McLaughlin, M. A., Narkevic, D. J., & Crawford, F. 2007, *Science*, 318, 777
- Lyutikov, M. 2020, *The Astrophysical Journal*, 889, 135
- Maan, Y., Surnis, M. P., Joshi, B. C., & Bagchi, M. 2022, *The Astrophysical Journal*, 931, 67
- Maan, Y., & van Leeuwen, J. 2017, in *URSI GASS*
- Macquart, J.-P., Prochaska, J. X., McQuinn, M., et al. 2020, *Nature*, 581, 391
- Madau, P., & Dickinson, M. 2014, *Annual Review of Astronomy and Astrophysics*, 52, 415
- Mannings, A. G., Fong, W.-f., Simha, S., et al. 2021, *The Astrophysical Journal*, 917, 75
- Marcote, B., Paragi, Z., Hessels, J. W. T., et al. 2017, *The Astrophysical Journal*, 834, L8
- Masui, K., Lin, H.-H., Sievers, J., et al. 2015, *Nature*, 528, 523
- McClintock, T., Rozo, E., Becker, M. R., et al. 2019, *The Astrophysical Journal*, 872, 53
- Mckinven, R., Michilli, D., Masui, K., et al. 2021, *The Astrophysical Journal*, 920, 138
- Narayan, R. 1992, *Philosophical Transactions: Physical Sciences and Engineering*, 341, 151
- Navarrini, A., Monari, J., Scalambra, A., et al. 2018, in *2018 2nd URSI Atlantic Radio Science Meeting (AT-RASC)*, 1
- Niu, C.-H., Li, D., Luo, R., et al. 2021, *The Astrophysical Journal Letters*, 909, L8
- Niu, C.-H., Aggarwal, K., Li, D., et al. 2022, *Nature*, 606, 873
- Oakes, D. 1982, *Biometrics*, 38, 451
- Ocker, S. K., Cordes, J. M., & Chatterjee, S. 2021, *The Astrophysical Journal*, 911, 102
- Ocker, S. K., Cordes, J. M., Chatterjee, S., & Gorsuch, M. R. 2022a, *The Astrophysical Journal*, 934, 71
- Ocker, S. K., Cordes, J. M., Chatterjee, S., et al. 2022b, *The Astrophysical Journal*, 931, 87
- Oostrum, L. C. 2020, PhD thesis
- Oostrum, L. C., Maan, Y., van Leeuwen, J., et al. 2020, *Astronomy & Astrophysics*, 635, A61
- Oswald, L. S., Karastergiou, A., Posselt, B., et al. 2021, *Monthly Notices of the Royal Astronomical Society*, 504, 1115
- Osłowski, S., Shannon, R. M., Ravi, V., et al. 2019, *Monthly Notices of the Royal Astronomical Society*, 488, 868
- Pandhi, A., Pleunis, Z., Mckinven, R., et al. 2024
- Pastor-Marazuela, I., Connor, L., van Leeuwen, J., et al. 2021, *Nature*, 596, 505
- Pastor-Marazuela, I., Leeuwen, J. v., Bilous, A., et al. 2023, *Astronomy & Astrophysics*, 678, A149
- Perley, R. A., & Butler, B. J. 2017, *The Astrophysical Journal Supplement Series*, 230, 7
- Petroff, E., Hessels, J. W. T., & Lorimer, D. R. 2019, *The Astronomy and Astrophysics Review*, 27, 4
- . 2022, *The Astronomy and Astrophysics Review*, 30, 2
- Petroff, E., Bailes, M., Barr, E. D., et al. 2015, *Monthly Notices of the Royal Astronomical Society*, 447, 246
- Petroff, E., Burke-Spolaor, S., Keane, E. F., et al. 2017, *Monthly Notices of the Royal Astronomical Society*
- Petroff, E., Oostrum, L. C., Stappers, B. W., et al. 2018, *Monthly Notices of the Royal Astronomical Society*
- Pingel, N. M., Pisano, D. J., Ruzindana, M., et al. 2021, *The Astronomical Journal*, 161, 163
- Planck Collaboration, Aghanim, N., Akrami, Y., et al. 2020, *Astronomy & Astrophysics*, 641, A6
- Platts, E., Caleb, M., Stappers, B. W., et al. 2021, *Monthly Notices of the Royal Astronomical Society*, 505, 3041

- Pleunis, Z., Good, D. C., Kaspi, V. M., et al. 2021a, *The Astrophysical Journal*, **923**, 1
- Pleunis, Z., Michilli, D., Bassa, C. G., et al. 2021b, *The Astrophysical Journal*, **911**, L3
- Price, D. C., Flynn, C., & Deller, A. 2021, *Publications of the Astronomical Society of Australia*, **38**, e038
- Price, D. C., Foster, G., Geyer, M., et al. 2019, *Monthly Notices of the Royal Astronomical Society*, **486**, 3636
- Prochaska, J. X., & Zheng, Y. 2019, *Monthly Notices of the Royal Astronomical Society*, **485**, 648
- Prochaska, J. X., Macquart, J.-P., McQuinn, M., et al. 2019, *Science*, **366**, 231
- Qiang, D.-C., Li, S.-L., & Wei, H. 2022, *Journal of Cosmology and Astroparticle Physics*, **2022**, 040
- Qiu, H., Shannon, R. M., Farah, W., et al. 2020, *Monthly Notices of the Royal Astronomical Society*, **497**, 1382
- Rajwade, K., Stappers, B., Williams, C., et al. 2021, [arXiv:2103.08410](https://arxiv.org/abs/2103.08410) [astro-ph]
- Rajwade, K. M., Bezuidenhout, M. C., Caleb, M., et al. 2022, *Monthly Notices of the Royal Astronomical Society*, **514**, 1961
- Ravi, V., Shannon, R. M., & Jameson, A. 2015, *The Astrophysical Journal*, **799**, L5
- Ravi, V., Shannon, R. M., Bailes, M., et al. 2016, *Science*, **354**, 1249
- Ryder, S. D., Bannister, K. W., Bhandari, S., et al. 2023, *Science*, **382**, 294
- Safarzadeh, M., Prochaska, J. X., Heintz, K. E., & Fong, W.-F. 2020, *The Astrophysical Journal*, **905**, L30
- Sammons, M. W., Deller, A. T., Glowacki, M., et al. 2023, *Monthly Notices of the Royal Astronomical Society*, **525**, 5653
- Sand, K. R., Faber, J. T., Gajjar, V., et al. 2022, *The Astrophysical Journal*, **932**, 98
- Sclocco, A., van Leeuwen, J., Bal, H. E., & van Nieuwpoort, R. V. 2016, *Astronomy and Computing*, **14**, 1
- Sclocco, A., Van Nieuwpoort, R., & Bal, H. E. 2014, in *Exascale Radio Astronomy* (Monterey, California: Bulletin of the American Astronomical Society), 3
- Sclocco, A., Vohl, D., & van Nieuwpoort, R. V. 2019, in *2019 RFI Workshop - Coexisting with Radio Frequency Interference (RFI)*, 1
- Scott, D. R., Cho, H., Day, C. K., et al. 2023, *Astronomy and Computing*, **44**, 100724
- Selsing, J., Krühler, T., Malesani, D., et al. 2018, *Astronomy & Astrophysics*, **616**, A48
- Serylak, M., Johnston, S., Kramer, M., et al. 2021, *Monthly Notices of the Royal Astronomical Society*, **505**, 4483
- Shannon, R. M., Macquart, J.-P., Bannister, K. W., et al. 2018, *Nature*, **562**, 386
- Sherman, M. B., Connor, L., Ravi, V., et al. 2024, *The Astrophysical Journal*, **964**, 131
- Simha, S., Burchett, J. N., Prochaska, J. X., et al. 2020, *The Astrophysical Journal*, **901**, 134
- Spitler, L. G., Scholz, P., Hessels, J. W. T., et al. 2016, *Nature*, **531**, 202
- Thornton, D., Stappers, B., Bailes, M., et al. 2013, *Science*, **341**, 53
- Tong, H., Liu, J., Wang, H. G., & Yan, Z. 2022, *Monthly Notices of the Royal Astronomical Society*, **509**, 5679, publisher: OUP ADS Bibcode: 2022MNRAS.509.5679T
- van Cappellen, W. A., Oosterloo, T. A., Verheijen, M. A. W., et al. 2022, *Astronomy & Astrophysics*, **658**, A146
- van Leeuwen, J., Kooistra, E., Oostrum, L., et al. 2022, [arXiv:2205.12362](https://arxiv.org/abs/2205.12362) [astro-ph.HE]
- . 2023, *Astronomy and Astrophysics*, **672**, A117
- Vohl, D., van Leeuwen, J., & Maan, Y. 2023, [arXiv e-prints](https://arxiv.org/abs/2311.09201), [arXiv:2311.09201](https://arxiv.org/abs/2311.09201)
- Walker, M., Tuntsov, A., Bignall, H., et al. 2017, *The Astrophysical Journal*, **843**, 15
- Wang, Y., & van Leeuwen, J. 2024, [arXiv e-prints](https://arxiv.org/abs/2405.06281), [arXiv:2405.06281](https://arxiv.org/abs/2405.06281)
- Xu, S., & Zhang, B. 2016, *The Astrophysical Journal*, **832**, 199
- Yamasaki, S., & Totani, T. 2020, *The Astrophysical Journal*, **888**, 105
- Yao, J. M., Manchester, R. N., & Wang, N. 2017, *The Astrophysical Journal*, **835**, 29
- Zhang, B. 2018, *The Astrophysical Journal*, **867**, L21
- Zhang, R. C., & Zhang, B. 2022, *The Astrophysical Journal Letters*, **924**, L14
- Zhu, W., & Feng, L.-L. 2021, *The Astrophysical Journal*, **906**, 95
- Zhu, W., Li, D., Luo, R., et al. 2020, *The Astrophysical Journal*, **895**, L6

Appendix A: Fast Radio Burst properties

This appendix contains the Tables A.1 and A.2 where the properties of the 24 FRBs detected during the Apertif survey are summarised.

Table A.1. Apertif Fast Radio Burst properties.

TNS Name	MJD barycentric	DM (pc cm^{-3})	S/N	N	Flux (Jy)	Fluence (Jy ms)	Width (ms)	τ_{sc} (ms)	$\Delta\nu_{\text{sc}}$ (MHz)	ν_{peak}^a (MHz)	BW ^b (MHz)
FRB 20190709A	58 673.218 777 99	662.83(8)	15	2	0.09(2)	0.52(10)	2.15(20)		3.1 ± 1.5	1370	>300
FRB 20190926B	58 752.031 731 03	957.1(8)	13	1	0.11(2)	5.8(12)	5.0(10)	0.78(39)		1370	>300
FRB 20191020B	58 776.781 603 36	464.8(2)	13	1	0.10(2)	2.78(56)	1.36(9)		7.4 ± 5.3	1370	>300
FRB 20191108A	58 795.831 621 98	587.79(6)	60	1	0.94(19)	13.6(27)	0.63(1)			1370	>300
FRB 20191109A	58 796.549 633 59	531.2(2)	13	2	0.15(3)	4.08(82)	2.28(13)		4.5 ± 1.3	1370	>300
FRB 20200210A	58 889.309 294 16	439.7(5)	38	1	0.16(3)	55.7(11)	29.63(55)	12.65(26)	0.8 ± 0.1	1449(1)	169(6)
FRB 20200213A	58 892.022 475 46	1017.7(2)	18	1	0.26(5)	4.39(88)	1.02(3)		9.3 ± 0.8	1361(2)	145(7)
FRB 20200216A	58 895.443 484 62	478.7(2)	27	3	0.21(4)	9.2(18)	7.22(8)			1520	>300
FRB 20200224B	58 903.659 557 87	1450(1)	17	1	0.12(2)	15.3(31)	10.1(11)	3.73(42)		1520	>300
FRB 20200321A	58 929.829 020 69	914.71(4)	13	2	0.05(1)	4.48(90)	1.79(19)			1436(7)	226(27)
FRB 20200322A	58 930.286 708 55	1290.3(10)	19	1	0.07(1)	9.9(20)	12.8(10)	4.16(44)	4.7 ± 2.3	1406(7)	277(33)
FRB 20200323C	58 931.383 711 75	833.4(2)	28	1	0.10(2)	6.6(13)	3.89(25)	1.33(9)	5.8 ± 1.2	1520	>300
FRB 20200419A	58 958.079 145 29	248.5(3)	19	1	0.59(12)	7.4(15)	0.58(2)		7.5 ± 0.8	1370	>300
FRB 20200514A	58 983.360 700 20	1406.2(2)	18	1	0.14(3)	5.2(10)	2.18(12)			1370	>300
FRB 20200516A	58 985.973 360 36	361.1(4)	10	1	0.05(1)	2.59(52)	2.24(19)			1520	>300
FRB 20200518A	58 987.731 459 01	246.5(1)	15	4	0.13(3)	4.67(93)	3.95(17)		5.2 ± 2.0	1370	>300
FRB 20200523A	58 992.145 198 81	444(9)	10	1	0.04(1)	6.9(14)	50.1(96)	12.47(356)		1370	>300
FRB 20200719A	59 049.574 229 15	2778(6)	13	1	0.05(1)	15.1(30)	51.8(58)	20.96(253)		1459(11)	259(49)
FRB 20201020A	59 142.506 451 21	398.59(8)	53	5	0.36(7)	13.5(27)	2.13(2)		4.1 ± 0.4	1370	>300
FRB 20210124A	59 238.426 897 90	868.25(7)	24	1	0.11(2)	4.61(92)	2.87(24)	0.65(9)	1.7 ± 0.3	1370	>300
FRB 20210127A	59 241.360 472 89	891.2(1)	35	1	0.43(9)	6.6(13)	0.83(2)			1370	>300
FRB 20210317A	59 290.295 710 36	466.5(1)	33	1	0.27(5)	6.0(12)	1.14(5)	0.22(3)	2.4 ± 0.3	1370	>300
FRB 20210530A	59 364.167 613 89	1000.27(9)	17	4	0.29(6)	18.7(37)	4.15(14)			1370	>300
FRB 20211024B	59 511.388 218 06	509.4(1)	80	1	0.45(9)	16.6(33)	1.45(1)			1370	>300

Notes.

^a Central frequency ν_{peak} for broadband bursts assumed to be the central frequency, 1370 MHz. For bursts with power law spectrum, 1520 MHz and 1220 MHz if they peak at the top or the bottom of the band respectively. Other values for narrowband bursts fitted to a Gaussian spectrum.

^b BW is the FWTM of the bursts with a Gaussian spectrum or > 300 MHz for broadband bursts.

Table A.2. Apertif Fast Radio Burst properties, continued.

TNS Name	RA ^a	DEC ^a	a ^a (arcsec)	b ^a (arcsec)	θ ^a (°)	Loc. area (arcmin ²)	CB	SB	DM _{MW+halo} ^b (pc cm ⁻³)	z _{Macquart} ^c	Γ ^d	α ^e	ν _{0,max} ^f (GHz)	E _{iso} ^g (erg)
FRB 20190709A	01h39m19.7s	+32d03m31.3s	223	3.3	96.90	0.64	10	36	52 + 32	0.68 ^{+0.16} _{-0.36}	-	-	2.3	2.0 × 10 ³⁹
FRB 20190926B	01h42m06.0s	+30d58m05.0s	1170	13.4	92.61	13.64	7	39	51 + 32	1.07 ^{+0.24} _{-0.54}	-	-	2.8	5.5 × 10 ⁴⁰
FRB 20191020B	20h30m39.0s	+62d17m43.0s	555	12.5	82.88	6.05	5	14	102 + 44	0.32 ^{+0.10} _{-0.18}	-	-	1.8	2.3 × 10 ³⁹
FRB 20191108A	01h33m31.4s	+31d41m33.4s	226	5.9	108.69	1.16	21	37	51 + 32	0.58 ^{+0.14} _{-0.32}	-	-	2.2	3.8 × 10 ⁴⁰
FRB 20191109A	20h38m11.1s	+61d43m10.8s	1084	13.6	144.33	13.25	18	44	105 + 44	0.42 ^{+0.10} _{-0.24}	-	-	1.9	5.9 × 10 ³⁹
FRB 20200210A	18h53m59.4s	+46d18m57.4s	148	6.0	109.20	0.78	9	37	70 + 47	0.36 ^{+0.10} _{-0.22}	-	13.8±0.9	2.0	3.3 × 10 ⁴⁰
FRB 20200213A	09h24m56.9s	+76d49m31.9s	144	7.5	78.65	0.94	9	48	45 + 31	1.15 ^{+0.24} _{-0.58}	-	-	2.9	2.3 × 10 ⁴⁰
FRB 20200216A	22h08m24.7s	+16d35m34.6s	216	12.5	95.68	2.34	5	30	48 + 41	0.44 ^{+0.12} _{-0.24}	±11.6±2.5	-	2.2	1.5 × 10 ⁴⁰
FRB 20200224B	02h20m24.7s	+19d26m22.1s	1037	10.2	88.92	9.26	14	33	44 + 31	1.65 ^{+0.36} _{-0.76}	±5.4±1.3	1.5±2.7	4.0	3.3 × 10 ⁴¹
FRB 20200321A	09h38m42.0s	+76d10m45.4s	190	9.0	113.74	1.49	5	37	45 + 31	1.00 ^{+0.24} _{-0.50}	-	-	2.9	2.8 × 10 ⁴⁰
FRB 20200322A	22h13m02.5s	+15d16m50.1s	424	10.3	103.79	3.83	6	29	46 + 40	1.47 ^{+0.32} _{-0.70}	-	4.5±2.3	3.5	1.6 × 10 ⁴¹
FRB 20200323C	22h12m01.0s	+15d46m21.9s	300	19.0	91.42	4.97	12	18	47 + 40	0.90 ^{+0.22} _{-0.46}	±6.2±1.1	3.5±3.0	2.9	4.5 × 10 ⁴⁰
FRB 20200419A	19h00m34.2s	+81d43m20.5s	212	7.0	132.69	1.29	32	56	55 + 35	0.08 ^{+0.04} _{-0.06}	-	-	1.5	3.5 × 10 ³⁸
FRB 20200514A	01h47m32.5s	+64d18m37.3	2374	12.1	105.49	25.01	2	40	181 + 44	1.35 ^{+0.30} _{-0.66}	-	-	3.2	7.7 × 10 ⁴⁰
FRB 20200516A	18h56m35.9s	+46d49m37.4	1121	10.3	134.05	10.08	18	22	73 + 47	0.24 ^{+0.06} _{-0.14}	±7.9±2.6	-	1.9	1.2 × 10 ³⁹
FRB 20200518A	09h36m45.3s	+77d22m36.8s	164	11.6	87.40	1.67	25	68	45 + 31	0.10 ^{+0.04} _{-0.08}	-	-	1.5	3.5 × 10 ³⁸
FRB 20200523A	18h55m37.1s	+47d07m38.1s	513	14.8	78.28	6.64	24	19	72 + 46	0.36 ^{+0.10} _{-0.20}	-	12.0±5.8	1.9	7.2 × 10 ³⁹
FRB 20200719A	09h18m41.1s	+77d23m06.8s	307	14.4	78.45	3.93	22	20	46 + 31	3.26 ^{+0.62} _{-1.35}	-	11.1±4.5	6.2	9.0 × 10 ⁴¹
FRB 20201020A	13h51m24.7s	+49d02m03.6s	115	8.3	80.88	0.84	29	17	29 + 32	0.36 ^{+0.10} _{-0.22}	-	-	1.9	1.4 × 10 ⁴⁰
FRB 20210124A	19h41m25.3s	+58d55m02.1s	147	7.0	99.54	0.89	11	48	80 + 44	0.90 ^{+0.22} _{-0.46}	-	4.4±3.3	2.6	3.1 × 10 ⁴⁰
FRB 20210127A	16h49m56.4s	+26d37m30.0s	155	5.5	84.89	0.75	21	34	41 + 44	0.98 ^{+0.24} _{-0.50}	-	-	2.7	5.3 × 10 ⁴⁰
FRB 20210317A	19h36m27.4s	+59d51m50.7s	129	4.8	97.13	0.54	23	35	76 + 43	0.38 ^{+0.10} _{-0.22}	-	-	1.9	7.0 × 10 ³⁹
FRB 20210530A	22h08m56.0s	+16d32m25.4s	185	18.4	95.56	2.97	6	36	47 + 40	1.11 ^{+0.26} _{-0.54}	-	-	2.9	1.9 × 10 ⁴¹
FRB 20211024B	13h20m34.5s	+42d29m20.7s	123	7.2	107.23	0.77	18	40	25 + 31	0.52 ^{+0.12} _{-0.30}	-	-	2.1	3.7 × 10 ⁴⁰

Notes.

- ^a Properties of the localisation region fitted to an ellipse. RA and DEC are the central coordinates of the ellipse, a and b the semi-major and semi-minor axes, respectively, of the 99% contour. The angle θ is the ellipse angle measured from West (lowest RA) through the North, using the same convention as ds9.
- ^b Milky Way DM from NE2001 model (Cordes & Lazio 2003) and halo DM from (Yamasaki & Totani 2020).
- ^c z_{max} computed from (Zhang 2018).
- ^d Spectral index Γ of bursts with power law spectrum.
- ^e Scattering index α of bursts with scattering tail, defined by τ_{sc} ∝ ν^{-α}.
- ^f Rest frame frequency upper limit ν_{0,max}.
- ^g Isotropic energy upper limit.

Table B.1. Host galaxy candidates and association probability for FRBs with ≤ 5 galaxies within the error region.

FRB	ID	Galaxy name	z_{phot}	r_r (")	m_r	$P(O)$	$P(O x)$
FRB 20200210A	G1	PSO J283.5110+46.3322	0.11 ± 0.01	6.1	18.0	0.924	0.580
	G2	PSO J283.5087+46.3348	0.40 ± 0.08	3.3	21.0	0.040	0.003
	G3	PSO J283.5028+46.3205	0.46 ± 0.06	2.9	21.5	0.025	0.289
	U					0.01	0.129
FRB 20200216A	G1	PSO J332.0996+16.6087	0.49 ± 0.07	2.6	21.4	0.325	0.424
	G2	PSO J332.0953+16.5341	0.51 ± 0.20	2.5	22.3	0.138	0.004
	G3	PSO J332.1018+16.6091	0.52 ± 0.09	2.4	21.6	0.265	0.370
	G4	PSO J332.0976+16.5926	0.56 ± 0.32	2.4	22.1	0.171	0.139
	U					0.1	0.064
FRB 20200419A	G1	PSO J285.2463+81.7361	0.15 ± 0.03	3.5	19.6	0.999	0.704
	U					0.001	0.296
FRB 20200518A	G1	PSO J144.1948+77.3261	0.08 ± 0.03	4.6	19.9	0.350	0.415
	G2	PSO J144.2179+77.3481	0.08 ± 0.02	4.6	19.4	0.640	0.557
	U					0.01	0.028
FRB 20200719A	G1	PSO J139.6135+77.4537	0.81 ± 0.96	2.4	22.7	0.048	1.8×10^{-4}
	G2	PSO J139.6677+77.3898	1.45 ± 0.51	3.7	22.6	0.052	0.101
	U					0.9	0.899
FRB 20210317A	G1	PSO J294.1082+59.8453	0.15 ± 0.05	3.2	20.0	0.391	0.541
	G2	PSO J294.1097+59.8285	0.15 ± 0.06	4.5	19.9	0.412	0.350
	G3	PSO J294.1028+59.8412	0.30 ± 0.05	2.4	20.7	0.186	0.088
	U					0.01	0.021
FRB 20211024B	G1	PSO J200.1431+42.4925	0.24 ± 0.07	2.9	20.5	0.194	0.235
	G2	PSO J200.1445+42.4911	0.24 ± 0.02	5.2	19.4	0.604	0.609
	G3	PSO J200.1529+42.5097	0.34 ± 0.35	1.0	24.5	0.006	3.3×10^{-4}
	G4	PSO J200.1548+42.5192	0.56 ± 0.27	2.7	21.8	0.052	4.2×10^{-4}
	G5	PSO J200.1392+42.4859	0.58 ± 0.18	1.9	22.0	0.045	0.042
	U					0.1	0.113

Notes. The galaxies are sorted by increasing redshift. Their ID is the same identifier as used in the text. The galaxy name is given by the Pan-STARRS source catalogue. The photometric redshift and errors are given by PS1-STRM. r_r and m_r are respectively the Kron radius and the magnitude in the r band as given by Pan-STARRS. $P(O)$ and $P(O|x)$ are respectively the PATH prior and posterior probability that the galaxy is associated with the FRB. For each FRB, U represents the unseen galaxies.

Appendix B: Host galaxy candidates

In Table B, we present the galaxies identified within the error regions for those FRBs with ≤ 5 host galaxy candidates, as well as the resulting association probabilities from the PATH analysis.

Table C.1. Apertif Fast Radio Burst polarisation properties.

TNS Name	L/I (%)	$ V /I$ (%)	RM_{obs} (rad m ⁻²)	RM_{MW} (rad m ⁻²)	RM_{host} (rad m ⁻²)
FRB 20191020B	31± 7	5± 7		24± 17	
FRB 20191108A	86± 2	0± 1	473.1± 2.2	-63± 13	1400 ⁺³⁰⁰ ₋₅₀₀
FRB 20200213A	10± 3	8± 6	300.3± 2.1	-17± 7	1500 ⁺⁴⁰⁰ ₋₅₀₀
FRB 20200216A	38± 6	11± 4	-2051.0± 5.8	-36± 10	-4200 ⁺¹³⁰⁰ ₋₈₀₀
FRB 20200321A	17± 5	13± 9		-16± 6	
FRB 20200322A	3± 6	14± 9		-28± 9	
FRB 20200323C	6± 3	0± 3		-30± 6	
FRB 20200419A	77± 6	4± 6		9± 8	
FRB 20200514A	51± 5	21± 9	979.8± 20.5	-215± 68	6500 ⁺²⁰⁰⁰ ₋₃₂₀₀
FRB 20200516A	17± 13	14± 7		1± 12	
FRB 20200518A	72± 12	29± 17		-17± 7	
FRB 20201020A	36± 2	8± 5	125.1± 37.5	17± 3	200 ⁺¹⁶⁰ ₋₁₄₀
FRB 20210124A	86± 8	15± 12		32± 18	
FRB 20210127A	53± 2	4± 5	121.9± 0.4	35± 9	330 ⁺¹³⁰ ₋₁₅₀
FRB 20210317A	50± 5	3± 4	-251.7± 1.3	26± 20	-530 ⁺¹⁶⁰ ₋₁₃₀
FRB 20210530A	52± 4	0± 7	-125.1± 4.6	-37± 10	-390 ⁺¹⁹⁰ ₋₁₆₀

Notes. Only FRBs with triggered full-Stokes data dumps are listed here. To ensure uniform layout, insignificant digits are sometimes also included.

Appendix C: Stokes data

In this appendix, we show the Stokes I, Q, U, and V data of the 14 new FRBs with Stokes data dumps, in Fig. C.1. When possible, we have performed an RM measurement, shown in Figures C.2 to C.6.

Appendix D: Scattering of FRB 20200210A

To better characterise the scattering of FRB 20200210A, we used `scatfit` to divide the full bandwidth into 16 subbands, and computed the S/N of the FRB in each one. If the S/N was above a threshold of 4.5, we performed a scattering fit. We used the scattering timescales in each subband to fit them to a power law as a function of frequency, since we expect $\tau_{\text{sc}} \propto \nu^{-\alpha}$. We find a scattering index $\alpha = 13.8 \pm 0.9$ (Note that `scatfit` defines the scattering index with an opposite sign). This result is robust, since we find a consistent α value when changing the number of frequency subbands and the S/N threshold. If this scattering index is used to scale the scattering timescale to 1 GHz, it would result in $\tau_{\text{sc}} \sim 1700 \pm 700$ ms. The result is shown in Fig. D.1.

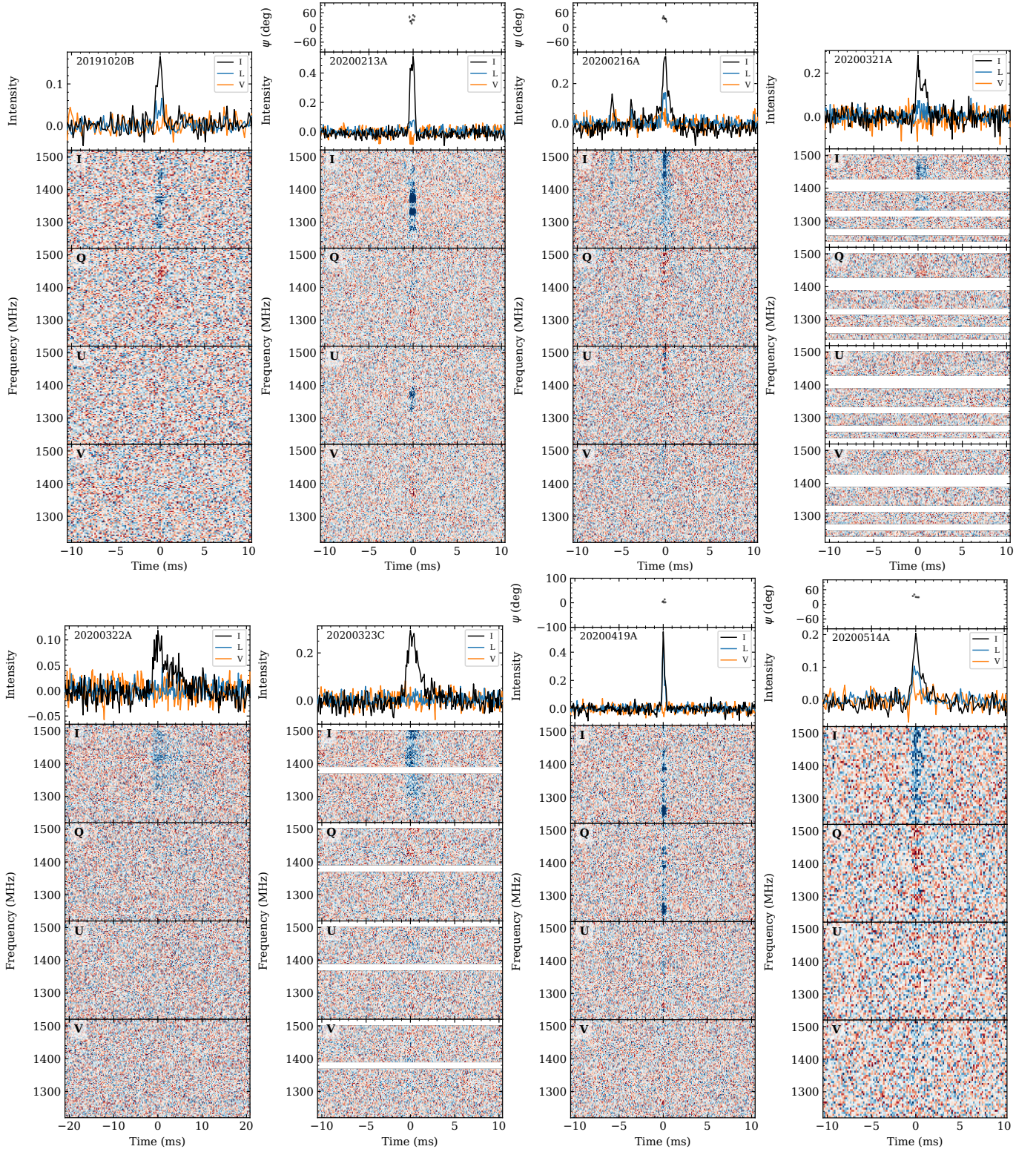


Fig. C.1. Stokes IQUV data of triggered FRBs. Each top panel shows the pulse profile of total intensity (Stokes I - black), linear polarisation ($\sqrt{Q^2 + U^2}$ - blue) after Faraday de-rotation when an RM is known, and circular polarisation (Stokes V - orange). The bottom panels show respectively Stokes I, Q, U, and V, without Faraday de-rotation. Blue indicates a positive value and red a negative value. The FRB name is indicated on the top right corner.

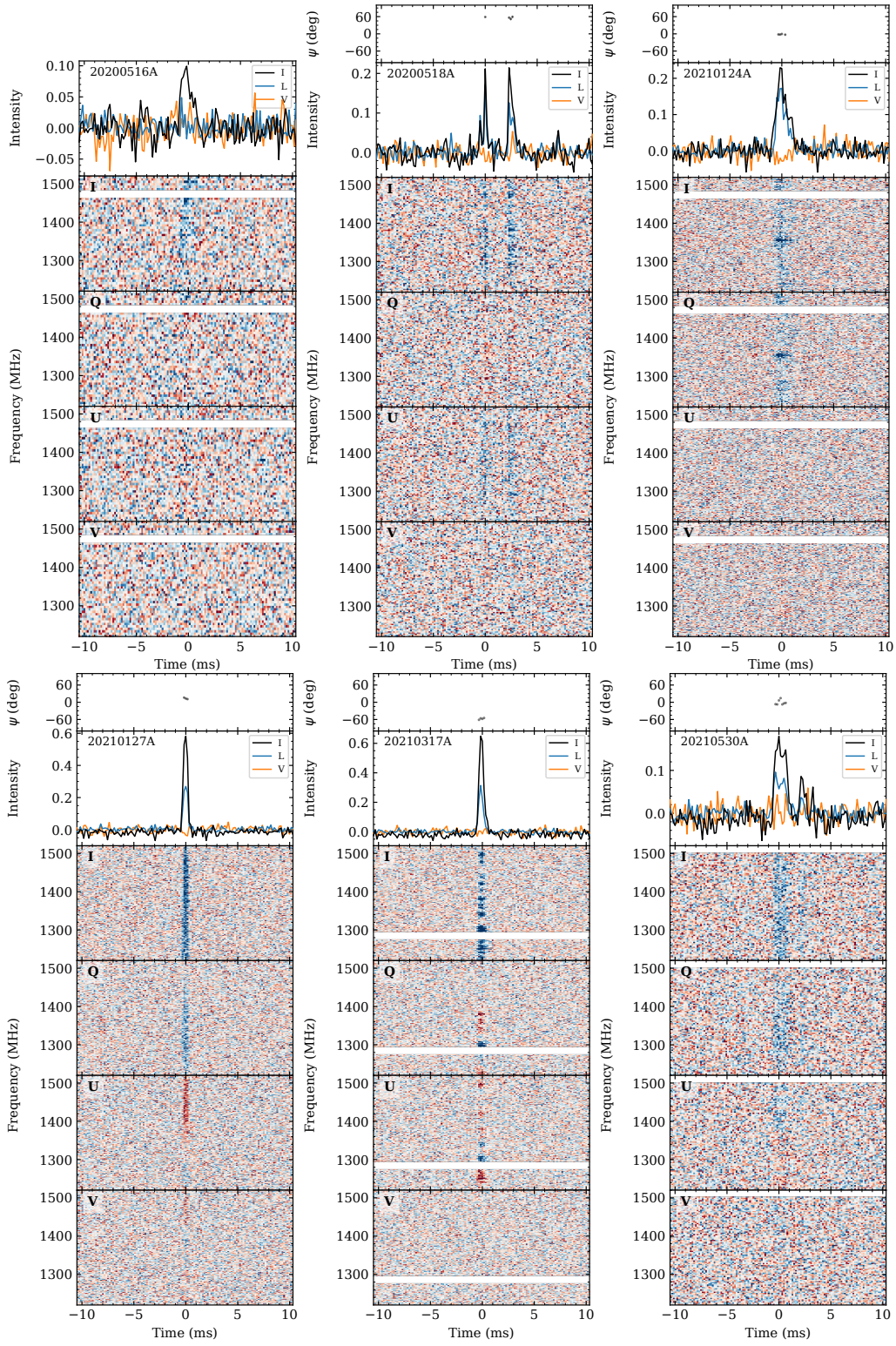


Fig. C.1. (Continued)

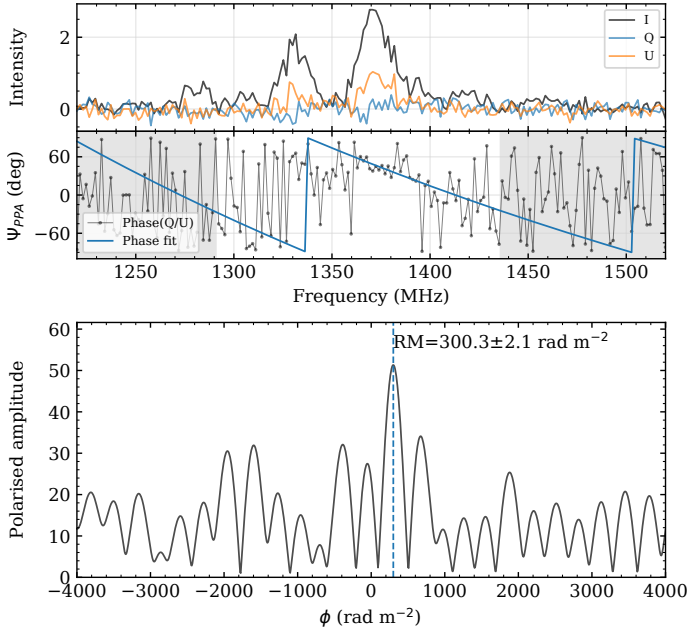


Fig. C.2. Rotation measure analysis of FRB 20200213A. The frequency channels between 1291 and 1436 MHz were used for the RM synthesis, since they are contained within the full width at tenth maximum of the spectrum fitted to a Gaussian.

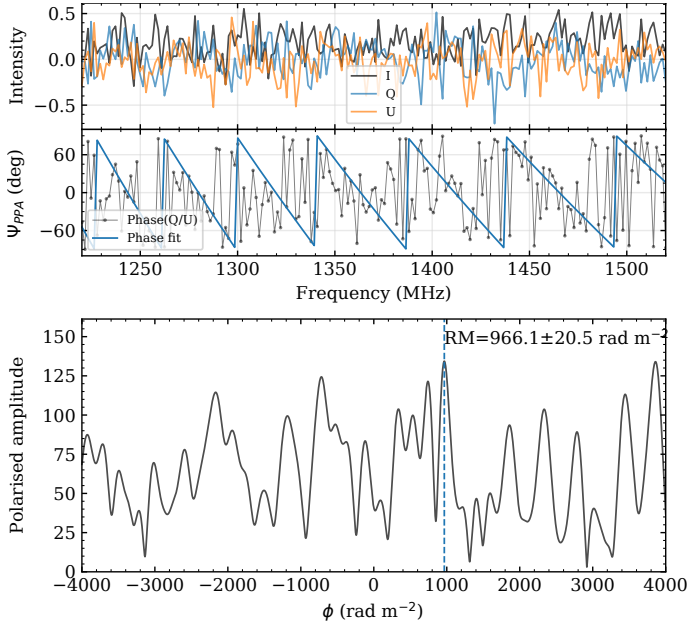


Fig. C.3. Rotation measure analysis of FRB 20200514A. Using whole bandwidth.

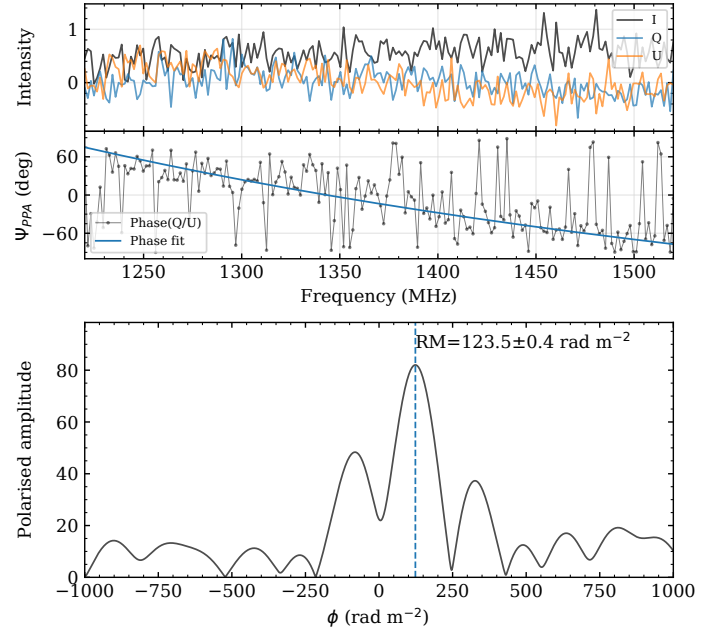


Fig. C.4. Rotation measure analysis of FRB 20210127A. Using whole bandwidth.

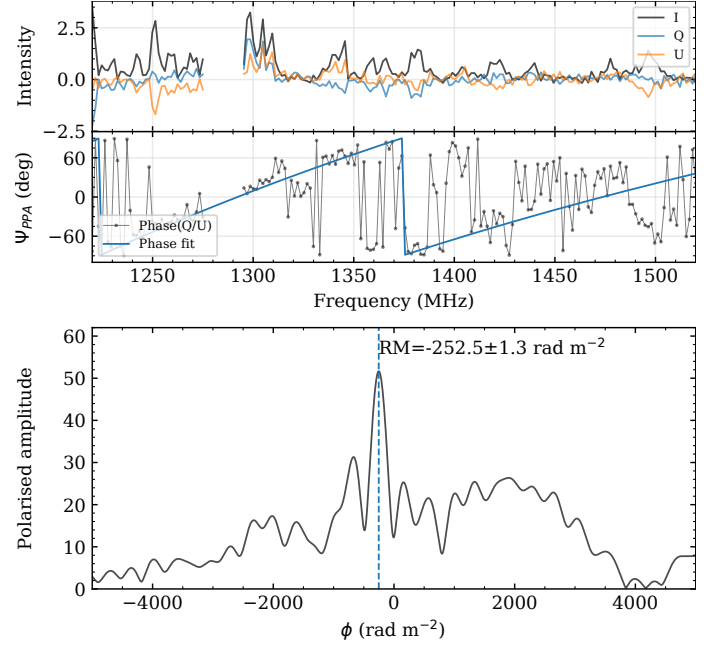


Fig. C.5. Rotation measure analysis of FRB 20210317A. Using whole bandwidth.

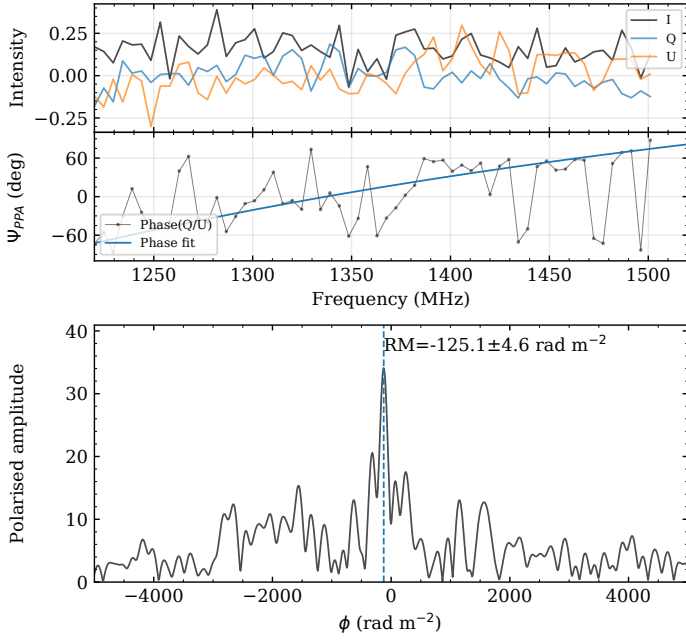


Fig. C.6. Rotation measure analysis of FRB 20210530A. Using whole bandwidth.

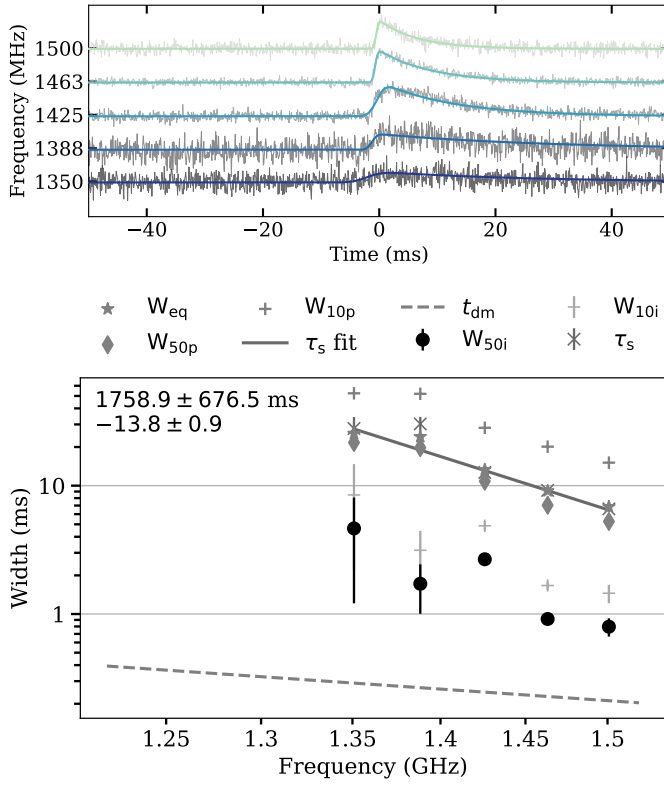


Fig. D.1. Multi-frequency scattering fit result for FRB 20200210A. The top panel shows the pulse profile in 6 subbands with $S/N > 4.5$, each one fitted to a Gaussian convolved with an exponential decay. The bottom panel shows the fit result at each subband. The scattering timescales are shown as crosses, while the fit to a scattering index is shown as a solid line. The text at the top right corner gives the expected scattering timescale at 1 GHz given the spectral index, and the line below the scattering index α .